

Tunable plasmon resonances in anisotropic metal nanostructures

Ph. D. Thesis Utrecht University, September 2006

ISBN-10: 90-393-4316-0

ISBN-13: 978-90-393-4316-6

Digital version: www.amolf.nl, www.colloid.nl

Tunable plasmon resonances in anisotropic metal nanostructures

Instelbare plasmonresonanties in anisotrope nanostructuren van metaal

met een samenvatting in het Nederlands

Proefschrift

ter verkrijging van de graad van doctor aan de Universiteit Utrecht op gezag van de rector magnificus, prof. dr. W. H. Gispen, ingevolge het besluit van het college voor promoties in het openbaar te verdedigen op maandag 25 september 2006 des middags te 4.15 uur

door

Johanna Jacoba Penninkhof

geboren op 23 maart 1978 te Utrecht

Promotoren:

Prof. Dr. A. Polman

Prof. Dr. A. van Blaaderen

Dit proefschrift werd mede mogelijk gemaakt door financiële steun van de Stichting voor Fundamenteel Onderzoek der Materie (FOM), de Nederlandse organisatie voor Wetenschappelijk Onderzoek (NWO) en NanoNed, een technologieprogramma van het Ministerie van Economische Zaken.

Contents

1	Introduction	1
1.1	General introduction	2
1.2	Optical constants	3
1.3	Light scattering and absorption	4
1.3.1	Small metal particles	5
1.3.2	Linear arrays of small metal particles	6
1.3.3	Large metal particles	7
1.3.4	Metal shell particles	8
1.4	Ion beam irradiation	8
1.5	This thesis	9
Part I	Colloidal masks	13
2	Modification of colloidal masks by optical tweezers and ion irradiation	15
2.1	Introduction	16
2.2	Experimental	16
2.3	Results and discussion	17
2.4	Conclusions	21
3	Modification of colloidal masks by wet-chemical growth	23
3.1	Introduction	24
3.2	Experimental	25
3.3	Results and discussion	26
3.4	Conclusions	29
Part II	Metal cores	31
4	MeV ion beam deformation of metal colloids in silica	33
4.1	Introduction	34
4.2	Experimental	34
4.3	Results and discussion	35
4.3.1	Au-core/silica-shell colloids	35
4.3.2	Au and Ag colloids in planar SiO ₂ films	38
4.4	Conclusions	39

5	MeV ion induced anisotropic plasmon resonances of Ag nanocrystals in glass	41
5.1	Introduction	42
5.2	Experimental	42
5.3	Results and discussion	43
5.4	Conclusions	46
6	Highly confined electromagnetic fields in arrays of strongly coupled silver nanoparticles	47
6.1	Introduction	48
6.2	Nanoparticle array fabrication	49
6.3	Optical absorption spectroscopy	50
6.4	Finite integration simulation procedure	51
6.5	Results and discussion	53
6.6	Conclusions	58
	Part III Metal shells	59
7	Ion beam deformation of metal shell colloids	61
7.1	Introduction	62
7.2	Experimental	63
7.3	Results and discussion	64
7.4	Conclusions	69
8	Optical properties of spherical and anisotropic gold shell colloids	71
8.1	Introduction	72
8.2	Fabrication	73
8.2.1	Synthesis of spherical Au-shell colloids	73
8.2.2	Preparation of substrates	74
8.2.3	Ion irradiation	75
8.2.4	Optical extinction	75
8.3	Spherical Au-shell particles	75
8.4	Anisotropic Au-shell particles	79
8.4.1	Angle-dependent extinction	79
8.5	Conclusions	83
9	Optical cavity modes in gold shell particles	85
9.1	Introduction	86
9.2	FDTD calculation scheme	87
9.3	Au-shell sphere	89
9.4	Cavity mode resonance	91
9.5	Oblate ellipsoidal Au-shells	92
9.6	Conclusions and outlook	94

10 Applications	95
10.1 Nanophotonics and information technology	96
10.2 Biomedical applications	96
10.3 Sensing	97
Appendix: Light scattering	99
References	103
Summary	113
Samenvatting	116
List of publications	119
Dankwoord	120
Curriculum vitae	122
Image gallery	123
Color images	126

1

Introduction

1.1 General introduction

Metal nanostructures show optical properties that are strikingly different from the properties of the bulk material. For example, the deep-red and yellow colors in stained glass are caused by small metal particles of gold and silver, respectively. This optical effect is due to a strong interaction between light and the conduction electrons, that are confined to the small volume of the metal particle. Under influence of an oscillating electric field, the negatively charged conduction electrons perform a collective motion with respect to the positive-ion background, creating an effective charge at the surface that results in a restoring force. The electron oscillation is therefore called a (localized) surface plasmon. Plasmon modes can also be found in bulk metals and at the interface between a dielectric and a metal. Under certain conditions, plasmons can be excited by light, which leads to strong light scattering and absorption and an enhancement of the local electromagnetic field.

The optical properties of small metal particles have inspired many researchers in the past 150 years. For example, Michael Faraday (1791-1867) showed that the red color in stained glass is due to small-sized Au particles, and the first theoretical framework to fully explain this peculiar interaction between light and matter was published by Gustav Mie (1869-1957) about a hundred years ago. [1] However, the research on plasmonic materials has increased remarkably in the past decade. This recent revival of interest is caused by the advances and increased expertise in fabrication methods to create metallic structures of well-defined sizes and shapes, [2, 3] and the many possibilities to use these materials in applications in optoelectronics, sensing, biology and medicine.

The key issue is that with plasmon-based structures light can be confined to and manipulated on a scale smaller than the wavelength of light (a few hundred nanometers), i.e., smaller than would be possible by conventional optics. [4] A striking example of this phenomenon is the high transmission efficiency of light through sub-wavelength holes in a thick metal screen. [5, 6]. The enhanced field intensity close to surface corrugations (like the holes in the metal film) is currently being investigated for use in near-field optical lithography and near-field optical storage heads. [6–9]

Exploiting the interfacial nature of the surface plasmons, thin metal films can replace dielectric waveguides in optical devices, as the electromagnetic energy (confined to the metal-dielectric interface) can be guided over distances of tens to hundreds of micrometers for visible and infrared wavelengths. [10–13] Very tight lateral confinement of light can be achieved by use of linear arrays of metal nanoparticles [14–16], along which electromagnetic energy can propagate over a micrometer distance. [17] Furthermore, the high local field enhancements close to the metal particles can be exploited for molecular sensors and spectroscopy and nonlinear optical elements. [18–25]

Plasmonic structures are often made of noble metals such as gold (Au) and silver (Ag), because these metals are stable under ambient conditions and show strong surface plasmon resonances. Moreover, they are compatible to biological systems and the binding of proteins, oligonucleotides and other biologically relevant systems to the metal surface is well established. Small particles of different sizes and shapes have been shown to be suitable markers, contrast agents (e.g., in optical coherence tomography) or therapeutic agents for biomedical applications. [26–30] For these applications, it is advantageous to be able to tune the particle plasmon resonance to the near-infrared region between 650 and 900 nm, where water and hemoglobin have their lowest absorption coefficient. [31–33]

This tunability is provided by engineering the shape and geometry of the particles.

The following sections give a brief introduction to the optical constants of noble metals, to plasmon resonances in spherical and ellipsoidal metal particles, and the optical properties of metal shell particles. Ion irradiation is introduced as a fabrication technique to tune the shape of metallo-dielectric particles.

1.2 Optical constants

The response of a material to the exposure of electromagnetic radiation is usually given by the frequency dependent dielectric constant $\epsilon(\omega)$. This dielectric constant is a complex number ($\epsilon = \epsilon' + i\epsilon''$) and is related to the index of refraction $N = n + ik$ by

$$\epsilon' = n^2 - k^2 \quad \epsilon'' = 2nk \quad (1.1)$$

The dielectric constants of a material can be obtained by reflection and/or transmission measurements on clean surfaces. For a dielectric medium like glass, the refractive index for optical frequencies is nearly constant and equals 1.5 ($\epsilon = 2.25$). Its imaginary part, related to absorption, is negligible. Glass, therefore, is transparent.

The dielectric constants of metals, however, depend strongly on optical frequency. They also tend to be highly absorbing and reflecting at visible and infrared wavelengths. Many metals (but not all) can be well described by a simple model developed by Drude. [34] This model assumes a gas of independent electrons that can move “freely” and scatter with phonons, electrons, lattice defects or impurities with a common average relaxation time τ . The dielectric constant is given by

$$\epsilon(\omega) = \epsilon_{high} - \frac{(\epsilon_{static} - \epsilon_{high})\omega_p^2}{\omega^2 + i\gamma_0\omega} \quad (1.2)$$

with ω_p the so-called plasma frequency and $\gamma_0 = 1/\tau$ the electron relaxation rate. ϵ_{static} is the relative permittivity at zero frequency; ϵ_{high} includes the contribution of the bound electrons to the polarizability. ϵ_{static} is equal to 1 if only the conduction band electrons contribute to the dielectric constant.

The most commonly used data from literature for ϵ are the tables in Palik’s *Handbook of Optical Constants* [35] and the tables by Johnson and Christy [36]. As an example, we have plotted the real and imaginary part of the dielectric constants for silver (triangles) and gold (circles) as a function of photon energy in the bottom and top graph of Fig. 1.1. Fits of the Drude model to the data at low frequencies are shown as well. It is clear that for Ag and Au, the Drude model fails at energies below 3.8 and 2.2 eV, respectively. At these frequencies, in addition to the free electrons, excitation of electrons from deeper bands into the conduction band (interband transitions) contribute to ϵ as well.

For particles with dimensions smaller than the mean free path of the conduction electrons, the dielectric constants become size-dependent: $\epsilon(\omega, R)$. The scattering of the conduction electrons at the surfaces can be taken into account by an additional damping term proportional to the Fermi-velocity v_F (about 1.4 nm/fs in Au and Ag) divided by an effective length R_{eff} . [37] The effective length can be the particle radius in case of a sphere, or the shell thickness in case of metal shell particles. Thus,

$$\gamma = \gamma_0 + Av_F/R_{eff} \quad (1.3)$$

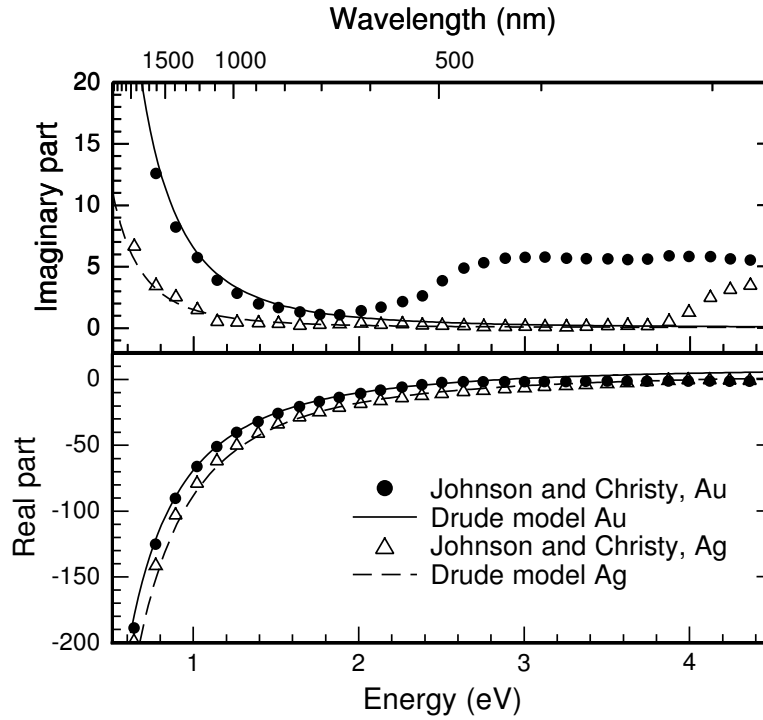


Figure 1.1: Real (bottom) and imaginary (top) part of the dielectric constants for bulk Au (circles) and Ag (triangles) as tabulated by Johnson and Christy. [36] The solid lines show the Drude model for Au with $\omega_p = 1.35 \times 10^{16}$ rad/s, $\gamma = 1.25 \times 10^{14}$ Hz, $\epsilon_{static} = 10.54$ and $\epsilon_{high} = 9.54$. For Ag (dashed lines), $\omega_p = 1.72 \times 10^{16}$ rad/s, $\gamma = 2.3 \times 10^{13}$ Hz, $\epsilon_{static} = 6.18$ and $\epsilon_{high} = 5.45$.

in which A is a dimensionless parameter, that depends on the details of the surface scattering process (e.g., defects, grain boundaries, chemical interface effects); it is usually set to unity. [37] The additional damping term results in an increase of the imaginary part with respect to the bulk value, the effect being larger at lower photon energies. This results in a broader and a less structured extinction spectrum [38].

The use of this correction term yields a better correspondence between calculations and ensemble measurements. However, the use of this size-dependent dielectric constant is under debate. For example, Nehl *et al.* concludes from the narrow line width of the scattering spectra of single Au-shell particles that interfacial electron scattering does not contribute significantly to the observed ensemble line width in ensemble measurements. [39] Another article that reports on dielectric constants measured on single Au particles by differential interference contrast microscopy, however, shows that a large scattering rate should be included to account for the discrepancy between the measured result and the size-corrected optical constants of Au from Johnson and Christy. [40]

1.3 Light scattering and absorption

The temporal and spatial evolution of the interaction of light with matter is described by electrodynamics. Light is represented by an electromagnetic wave that travels through a polarizable medium, and is modified by the polarization it induces in the medium. The

ease with which the medium is polarized is specified by the polarizability.

A quantity that is more related to optical transmission measurements than the polarizability is the extinction cross section, which is a measure of the amount of light that is extinct by the particle, either by absorption (transfer to heat) or by scattering (reradiation). For very small particles, the contribution of scattering to the extinction is small compared to the absorption. Then, the polarizability α and the extinction cross section C_{ext} are directly related by $C_{ext} = C_{abs} = kIm[\alpha]$ with $k = 2\pi/\lambda$ the wavevector.

In the beginning of the 20th century, Gustav Mie solved Maxwell's equations for an electromagnetic light wave interacting with a sphere. [1] When applying the correct boundary conditions for a sphere, the calculations gave a series of multipole oscillations (dipole, quadrupole, etc) for the extinction and scattering cross section of the particle as function of particle radius. With this result, and the assumption that the macroscopic, frequency-dependent dielectric constants of the bulk material could be applied to a small metal sphere, he was able to explain the beautiful colors of stained glass.

1.3.1 Small metal particles

For very small particles, the fields can be considered homogeneous (constant) over the particle, and only the low-order modes contribute to the extinction. Then, the situation can also be considered as a particle placed in a uniform *static* electric field (quasistatic regime). The theory by Mie only describes the response of a sphere, but can be easily generalized to ellipsoids in the quasistatic regime. For an ellipsoidal metal particle, the polarizability α is given by: [34]

$$\alpha = 4\pi\epsilon_0 V \frac{\epsilon - \epsilon_m}{3\epsilon_m + 3L_i(\epsilon - \epsilon_m)} \quad (1.4)$$

with ϵ and ϵ_m representing the dielectric constant of the metal and the surrounding medium, V the volume of the particle and L_i a geometric factor that depends on the semi-axes of the particle. The sum of the geometric factors L_i is 1, and for spheres $L_i = \frac{1}{3}$. For an anisotropic particle, the geometric factor for light polarized along the long axis of the particle is less than $\frac{1}{3}$.

The polarizability is largest when the denominator in Equation (1.4) equals to zero, i.e., for $\epsilon = (1 - 1/L_i)\epsilon_m$. Then, the particle is excited on resonance. The frequency at which the resonance occurs depends strongly on shape (by L_i), the properties of the metal (ϵ) and of the surrounding medium (ϵ_m), as directly follows from Equation (1.4).

The effect of the optical constants of the metal and the surrounding medium on the polarizability is illustrated in Fig. 1.2. The solid line shows the calculated extinction spectrum of a spherical Au particle with a diameter of 50 nm in water. The peak in extinction is found at a wavelength of about 520 nm, i.e., green light is absorbed, giving the particles their red color. The spectrum of a Ag sphere of the same size in the same medium is also shown in Fig. 1.2 (dashed line). The extinction peak is found at a smaller wavelength (at 420 nm), a direct consequence of the different dielectric constants for Ag than for Au (see Fig. 1.1). Changing the embedding medium to glass instead of water (i.e., ϵ_m from 1.45 to 1.33) causes a peak shift for Ag by about 25 nm (see dash-dotted line). The glass effectively screens the surface charges resulting in a smaller restoring force and thus to a lower resonance frequency.

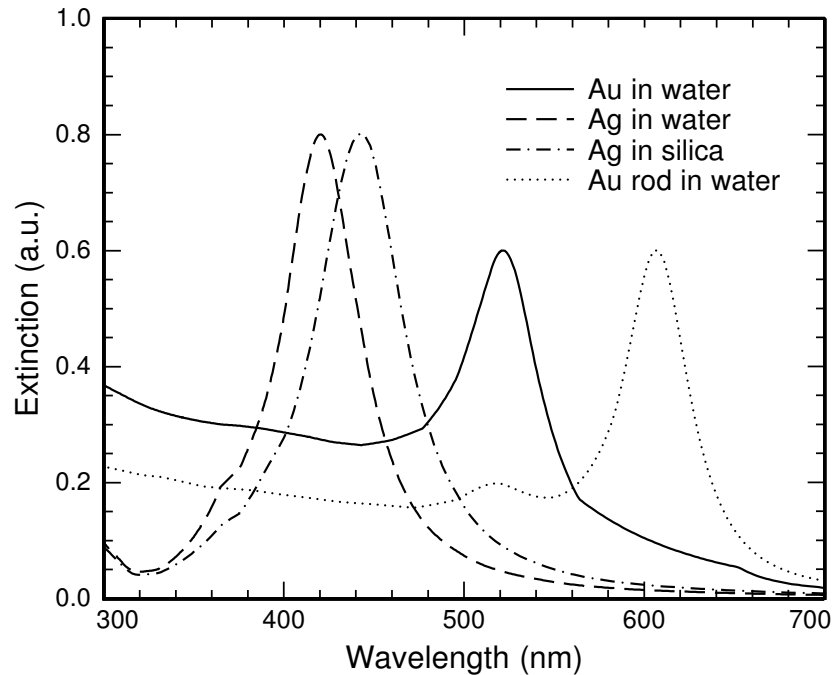


Figure 1.2: Calculated extinction spectra of Au spheres (solid line), Au rods (dotted line) and Ag spheres in water (dashed line) or silica (dash-dotted line). The refractive index of silica is taken as 1.45, the radius of the particles is 25 nm. The rods have aspect ratio of 2 with a length of 80 nm.

The plasmon resonance frequency can be further tuned by changing the shape of the particle. As an example, the extinction spectrum of a gold rod in water with size aspect ratio of 2 (length 80 nm) is shown in Fig. 1.2. The spectrum, calculated by the T-matrix method, [41] is averaged over all orientations of the particle. Two distinct peaks are observed: a small peak at about the plasmon resonance of the Au sphere and a large peak at a wavelength of 605 nm. The large peak is related to the resonance that corresponds to the excitation of a plasmon mode along the long axis of the particle. For this longitudinal excitation, the field-induced charges are separated over a larger distance with respect to a sphere with the same volume. The restoring force is thus smaller and hence the resonance frequency is red-shifted. A similar argument with increasing restoring force can be used to explain that the resonance frequency corresponding to excitation along the short axes of the rod (transverse excitation) is slightly blue-shifted (in this case by about 5 nm).

1.3.2 Linear arrays of small metal particles

Tunability of the plasmon resonance is also obtained in ensembles of coupled nanoparticles. For example, the extinction spectrum of a linear array of small closely-spaced metal particles can show two plasmon excitation bands resulting from electromagnetic coupling between neighboring particles. [42, 43] When incident light is polarized transverse to the array axis, repulsion between like surface charges on neighboring particles increases the energy required to drive a resonant oscillation and therefore results in a spectral blue-shift. Conversely, attraction between nearby unlike surface charges under longitudinally

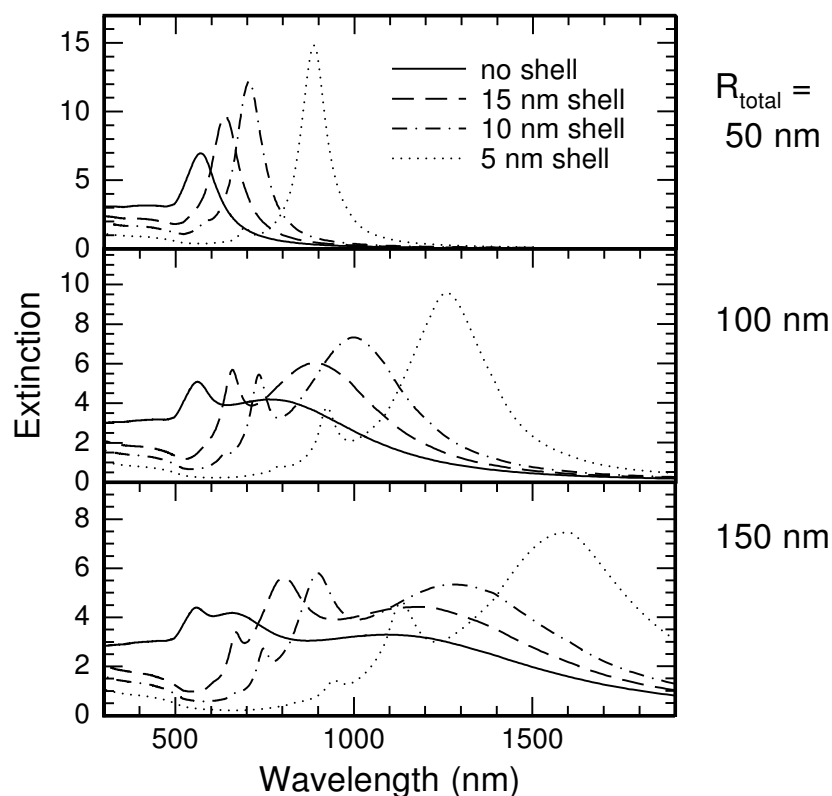


Figure 1.3: Optical extinction of solid Au particles in water (solid lines) calculated for three particle radii: 50 (top), 100 (middle) and 150 nm (bottom). Data for silica-core/Au-shell particles are also shown. The shell thickness is varied from 5 nm (dotted line), 10 nm (dash-dotted line) to 15 nm (dashed line). A thin shell results in a strong coupling between plasmons at the inner and outer surface of the metal shell.

polarized incident light will result in an extinction red-shift.

Numerical calculations by Quinten and Kreibig for linear arrays of small Ag spheres showed that the peak splitting depends on the nearest-neighbor distance and the number of particles in the array. [43] The largest peak splitting is observed for arrays with almost touching spheres. For larger inter-particle distances the peak splitting decreases, and vanishes for distances larger than 6 particle radii.

1.3.3 Large metal particles

The optical properties of metal nanoparticles are also influenced by particle size. For instance, for metal particles larger than about 30 nm the relative contribution of scattering to the extinction (sum of absorption and scattering) increases. With increasing particle size, higher order plasmon modes appear in the extinction spectrum. The plasmon resonance band of the dipolar mode shifts towards the red and its bandwidth increases. Higher-order modes can be observed in the spectrum and become more dominant. This can be explained by the fact that for larger particles the light cannot polarize the particle homogeneously and retardation effects lead to a gradient of the electromagnetic field, that can excite higher order modes.

This effect is illustrated in Fig. 1.3, where the solid lines represent the calculated extinction spectra for a Au particle in water, with a radius of 50 nm (top panel), 100 nm (middle) and 150 nm (bottom). For the $R=50$ nm particle, the peak is already red-shifted compared to the $R=25$ nm Au particle in Fig. 1.2 (peaks at 570 nm and 530 nm respectively). For the larger particles the red-shift becomes larger and also quadrupole modes ($R=100$ nm, $R=150$ nm) and the octupole mode ($R=150$ nm) are visible.

1.3.4 Metal shell particles

The optical response of spherical core-shell particles, composed of a dielectric core and a metal shell can be calculated by the Mie formalism using the extension by Aden and Kerker. [44] In these particles, plasmon modes can be excited on both the inner and outer boundaries of the shell. Coupling between these surface plasmon modes results in splitting of the plasmon resonance into two new plasmon resonances: a low-energy mode with the inner and outer shell surfaces symmetrically polarized, and a high-energy mode with the inner and outer shell surfaces oppositely polarized. [45, 46] The symmetric mode has a large net dipole moment and can interact strongly with an incident optical field; the antisymmetric mode does not couple strongly and therefore is not observed in the optical spectrum. The shift in plasmon frequency is determined by the coupling strength and increases with decreasing metal shell thickness.

Figure 1.3 demonstrates the effect of metal shell thickness on the extinction spectrum for spherical particles with a total radius of $R=50$ nm, 100 nm and 150 nm in water. The graph shows that silica-core/Au-shell particles have red-shifted spectra compared to a bulk gold particle of the same size, with a larger global shift for thinner shells. The higher order multipole modes, clearly present in the spectra for particles with radii of 100 nm and 150 nm, are also red-shifted due to coupling of the surface plasmon modes at the inner and outer surface of the metal shell. An increase of the relative peak height of the dipole mode compared to the higher order multipole modes is observed for particles with thin shells.

For metal shell particles, the plasmon frequency can thus be tuned over a large wavelength range by changing the relative size of the inner and outer radius of the shell.

1.4 Ion beam irradiation

Nowadays, a versatile and widely used tool to modify the properties of materials is ion irradiation. For example, semiconductor materials are electrically and optically doped by ion implantation, and structures are fabricated on a nano- to micrometer scale by use of focussed ion beams. Large electric fields are used to accelerate charged atoms to energies of typically 10 keV or more. Ions gradually lose their energy as they travel through a solid, both from collisions with the target atoms (nuclear stopping) and electronic excitations and ionization of atoms (electronic stopping). The loss of ion energy, stopping, depends on the ion species, the ion energy and the target material. [47]

Most structural changes are caused by nuclear collisions, since the incident ion can transfer a large fraction of its energy to target atoms. These atoms can be displaced from their original positions, resulting in the creation of defects, sputtering of atoms from the surface, and amorphization of crystalline materials.

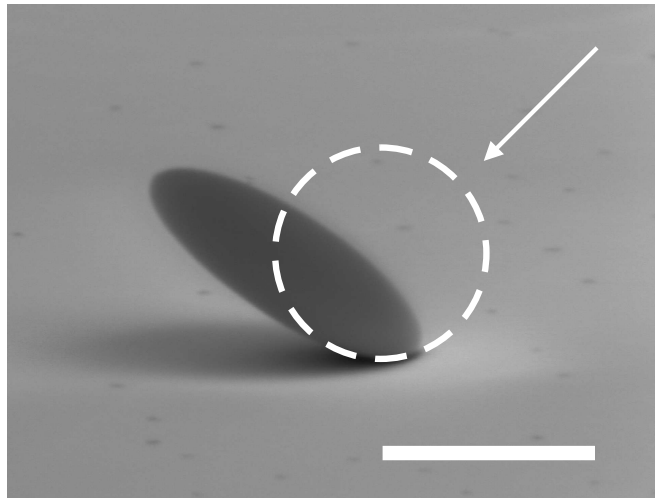


Figure 1.4: Electron microscopy image of a silica colloid ($d = 1 \mu\text{m}$) after ion irradiation with 6 MeV Au ions to a fluence of $6.5 \times 10^{14} \text{ cm}^{-2}$. The ion irradiation induces an anisotropic shape change: the initially spherical colloid (indicated by dashed circle) deforms into an oblate ellipsoid. Scale bar is 1 micron.

For ions with very high energies (typically MeV or higher), the electronic stopping is relatively large compared to the nuclear stopping. Then, the ions travel along a more or less straight path through the target material, depositing energy in a very narrow region around this ion track by electronic excitations. The temperature of this cylindrically shaped ion track with a diameter of typically a few nanometers can easily exceed the melting temperature. The resulting thermal stress in combination with the reduced viscosity leads to shear relaxation, that is frozen in upon rapid cooling of the ion track. The net effect is an anisotropic shape change. This plastic deformation effect has been observed for amorphous materials (insulators, semiconductors or metallic glasses) under MeV ion irradiation [48–54], but not for pure crystalline materials like metals, [48, 55] and is well described by a viscoelastic continuum model. [56, 57]

One of the most striking examples of this phenomenon is the deformation of silica colloidal particles under MeV ion irradiation. [55, 58] Initially spherical silica colloids expand perpendicular to the ion beam and contract parallel to the ion beam changing their shape to oblate ellipsoidal. This is illustrated in Fig. 1.4 which shows a scanning electron microscopy (SEM) image of a $1\text{-}\mu\text{m}$ -diameter silica colloid after 6 MeV Au ion irradiation at 77 K to a fluence of $6.5 \times 10^{14} \text{ cm}^{-2}$. The initial size of the colloid is indicated by the dashed circle. A shape anisotropy with a size aspect ratio (major-to-minor axis) of 1.9 is observed at this fluence.

1.5 This thesis

The work presented in this thesis focusses on the optical properties of colloidal systems composed of a metal (Au, Ag) and a dielectric (silica), with an emphasis on the relation between shape anisotropy and optical properties. The technique of MeV ion irradiation is used to modify the optical properties of the materials. The thesis is divided in three parts.

Part I: Colloidal masks

Nanosphere lithography is known as a relatively simple technique to create metal particle arrays on a substrate by evaporation through a mask of colloidal particles. One limitation is that the size of the metal particles is determined by the size of the colloids in the mask. Part I of this thesis presents two different methods to control and decouple the nanoparticle size from the size of the colloids in the mask. In Chapter 2, ion irradiation is used to cause an in-plane expansion of the silica colloids in the mask, thereby decreasing the hole size. Chapter 3 shows that the hole size can also be decreased by wet chemical growth of a layer of silica on top of the mask. In both cases, the size of the holes can be controlled at the nanoscale. Chapter 2 also shows that optical tweezers can be used to position colloids in an arbitrary geometry. The masks created in this way can then be modified by ion irradiation.

Part II: Metal cores

The MeV ion deformation process of metal cores in silica is studied in Chapter 4. While single Au colloids do not show deformation, the presence of a silica shell induces a shape change in the metal. Both in a core-shell structure and in thin films, spherical Au particles become prolate ellipsoidal with the long axis in the direction of the ion beam. The metal deformation only occurs above an electronic energy loss threshold in the silica of ~ 3.3 keV/nm. Silver cores embedded in silica do not show elongation, but rather disintegrate. The results in this Chapter indicate that solubility effects are likely to play a role in the deformation mechanism of the core-shell composite.

Another system, Ag particles embedded in ion-exchanged soda-lime glass, is described in Chapter 5. The plasmon resonance band of Ag particles in soda-lime glass splits upon MeV ion beam irradiation at an angle of 60° with the surface normal. Transmission electron microscopy shows arrays of particles aligned along the direction of the ion beam. The splitting of the plasmon peak is ascribed to electromagnetic coupling between the particles along the arrays. This effect is confirmed and further studied by full-field finite difference time domain (FDTD) calculations, presented in Chapter 6.

Part III: Metal shells

Chapter 7 presents the effect of ion irradiation on silica-core metal-shell colloids. The metal shell colloids change shape from spherical into oblate ellipsoidal. The shape change is attributed to the ion-induced anisotropic deformation process in the amorphous silica core, while the deformation is counter-acted by the mechanical constraint of the metal shell.

In Chapter 8, the optical properties of silica-core/Au-shell colloids are studied by experiments and calculations. For spherical Au-shell colloids, the effect of small changes in the core radius and shell thickness was investigated by T-matrix calculations. For particles with a size comparable to the wavelength of light, the shift of the plasmon resonance frequency is found to be relatively complex as phase retardation and plasmon coupling (at the inner and outer surface of the metal shell) can have opposite effects. Oriented oblate ellipsoidal Au-shell particles were made by ion irradiation with aspect ratios up to 1.8. Angle-dependent extinction measurements show that the relative strength of the dipole to higher-order modes can be tuned by changing the anisotropy of the particle and the

angle of incidence. Comparison to T-matrix calculations are in good agreement with the experimental data.

Chapter 9 shows that Au-shell particles with a diameter comparable to the wavelength of light can sustain resonances with electric field enhancements over a large volume in the dielectric core. The resonance frequencies found in FDTD calculations correspond to peaks in the absorption spectra calculated by the T-matrix method, and depend on the size, dielectric constant and shape of the dielectric core. The concept of a cavity mode is supported by the resonance blue-shift for longitudinal and red-shift for transverse polarized light.

Finally, Chapter 10 reports on several possible applications in nanophotonics, sensing and medicine, taking advantage of the shape control explored in this thesis.

Part I

Colloidal masks

Modification of colloidal masks by optical tweezers and ion irradiation

A method is presented to control the in-plane ordering, size and interparticle distance of nanoparticles fabricated by evaporation through a mask of colloidal particles. The use of optical tweezers combined with critical point drying gives single-particle position control over the colloidal particles in the mask. This extends the geometry of the colloidal masks from (self-organized) hexagonal to any desired symmetry and spacing. Control over the mask's hole size is achieved by MeV ion irradiation, which causes the colloids to expand in the in-plane direction, thus shrinking the size of the holes. After modification of the mask, evaporation at different angles with respect to the mask gives additional control over structure and interparticle distance, allowing nanoparticles of different materials to be deposited next to each other. We demonstrate large arrays of metal nanoparticles with dimensions in the 15–30 nm range, with control over the interparticle distance and in-plane ordering.

2.1 Introduction

Arrays of nanoparticles can find applications in photonic, electronic, magnetic and sensor devices. [17, 26, 59–62] Conventional methods used to fabricate structures of nanoparticles (like electron beam lithography) are complex, expensive, and time consuming. An alternative method to create arrays of small particles on a substrate is nanosphere lithography (NSL). This technique was pioneered in the early 1980's [63, 64] and was further developed by several groups. [65, 66] In NSL, a self-organized layer of colloidal spheres is used as a mask for a lithographic step like illumination, deposition or etching. When used as a deposition mask, an array of particles is left on the substrate after removal of the colloidal mask. NSL is a simple, fast and inexpensive method to create large arrays of particles on a substrate. Typical feature sizes after removal of the mask are 100 nm and above. Arrays of metallic nanoparticles created with NSL were used to study plasmonic resonances [67] and to fabricate plasmonic sensors. [68] Surfaces patterned with colloidal masks have also been used for catalyzing the growth of nano-fibers (e.g., of carbon [69] and ZnO [70]) and for selective protein adsorption. [71] More complex structures of particles can be created using multiple depositions at different angles and by rotating the sample during deposition. [67, 72]

Nanosphere lithography has two major disadvantages. [65, 66] Firstly, the geometry of the mask of colloidal particles is limited since it is created by self-organization: for a single layer the only structure is hexagonal close packed. Secondly, the size and spacing of the mask holes are coupled, and thus these properties can not be independently controlled.

In this paper we present a combination of two methods to resolve these limitations of nanosphere lithography: we create colloidal masks with arbitrary geometry using optical tweezers, and tune the shape of the mask using ion irradiation. In this way, the in-plane ordering as well as the size and interparticle distance of nanoparticles formed by evaporation through the mask can be controlled. Recently, two other methods have been developed to control the size of the holes independently from the size of the colloids in the mask. [72] [Chapter 3]. For a recent review article, see Ref. [73].

2.2 Experimental

To create masks with arbitrary geometry, glass or silicon substrates were given a positive surface charge and then patterned with negatively charged colloidal silica particles using optical tweezers. [74, 75] Glass microscope cover slides (diameter 19 mm, Chance, thickness #1) and Si(100) wafers were used as received. These substrates were immersed in a mixture of 170 mL ethanol and 4.5 mL ammonia (29 wt.-%). Then 23.5 mL 3-aminopropyl triethoxysilane was added and the substrate was let to react for 1.5 hours under stirring. All chemicals were analytical grade, obtained from Merck, and used as received. The substrate was then taken from the mixture and rinsed with ethanol. A sample cell was prepared by sandwiching a drop of colloidal dispersion between a (uncoated) glass microscope cover slide and a coated substrate. Silica particles with a diameter of 1.0 μm or 1.4 μm and a polydispersity less than a few percent were synthesized using a Stöber growth process and subsequent growth steps using methods described in detail elsewhere. [76–78] The size and polydispersity were determined using scanning electron microscopy (SEM, FEI XL30 SFEG, 1–15 keV) on several hundreds of particles. Op-

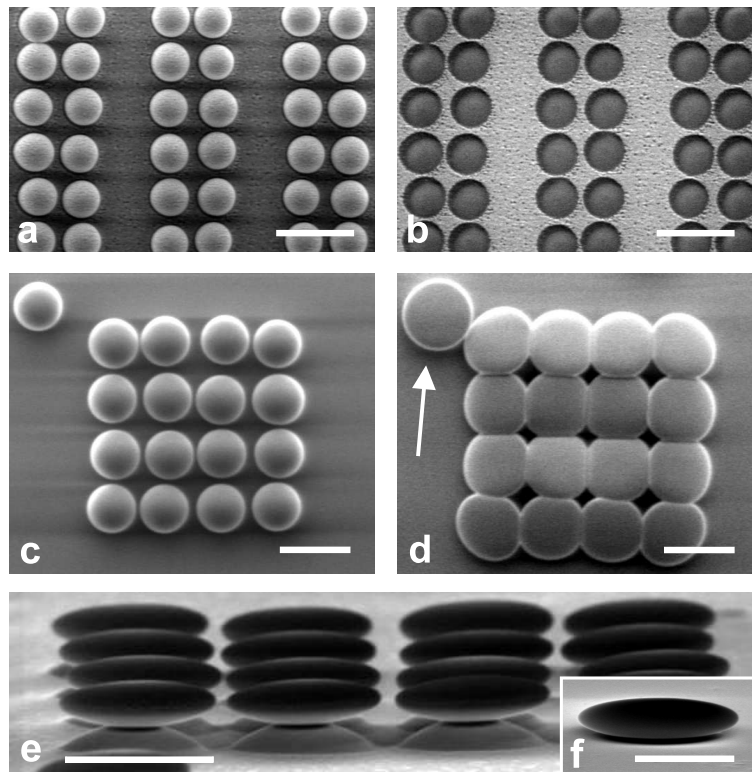


Figure 2.1: Colloidal masks made with single-particle position control using optical tweezers, and then modified with 4 MeV Xe^{4+} ion irradiation. (a) SEM image of 1.0 μm diameter silica particles positioned on a glass substrate using optical tweezers. The sample was dried using critical point drying and covered with a 10 nm thick silver layer by thermal evaporation. (b) After removal of the particles with sonication, the structure of the mask was replicated on the substrate. (c) 1.4 μm diameter silica particles positioned with square symmetry. (d) Same structure after normal-incidence irradiation with 4 MeV Xe^{4+} ions to a fluence of $2.0 \times 10^{15} \text{ cm}^{-2}$ at 90 K. The in-plane expansion of the colloidal particles can be tuned by varying the ion fluence. (e) Side-view of an array of ion beam deformed 1.4 μm diameter silica colloids (4 MeV Xe^{4+} , $2.0 \times 10^{15} \text{ cm}^{-2}$) imaged at an angle of 10° with respect to the substrate. Not only the silica particles but also the glass substrate was deformed. The size aspect ratio of the particles was 3.4. (f) Side-view (at 10°) of a ion beam deformed 1.4 μm diameter silica colloid (4 MeV Xe^{4+}) on a silicon substrate. Note that the silicon substrate did not deform, while the silica particle deformed as in Fig. 2.1(e). Scale bar in (a-e) is 2 μm ; (f) 1 μm .

tical tweezers were used to position negatively charged colloidal particles, taken from a reservoir at the bottom of the sample, on the positively charged substrate. [74] The optical tweezers setup is described in detail elsewhere. [79]

2.3 Results and discussion

This optical tweezers method allows masks to be created with control over the position of single particles. After patterning, the sample is removed from the solvent using critical point drying (CPD, Bal-tec; CPD 030) to prevent capillary forces from breaking up the structure. [75] Figure 2.1(a) shows a SEM image of a double-line array of 1.0 μm

diameter silica particles on a glass substrate after patterning and drying. The average centre-to-centre distance between the colloidal particles within each line was $1.2 \mu\text{m}$. A 10 nm thick silver layer was deposited onto the colloidal mask by thermal evaporation at a base pressure of 1.3×10^{-6} mbar. The same section of the substrate is shown in Fig. 2.1(b) after the mask was removed by sonication in ethanol. Clearly, the mask was replicated in the silver layer on the substrate. The method can be used to create more complex masks in which colloidal particles of different size, shape, and composition can be incorporated. [79, 80]

Additional control over the mask's dimensions can be achieved by ion irradiation. As we have shown earlier, under irradiation with an MeV ion beam individual colloidal particles expand in the plane perpendicular to the ion beam and shrink parallel to the ion beam. [58] This plastic deformation effect can be used to tune the size and shape of the holes in the colloidal deposition mask. Figure 2.1(c) shows a SEM image of a cubic mask pattern created with optical tweezers and CPD on a glass substrate. The center-to-center distance between the $1.4 \mu\text{m}$ diameter silica particles was $1.6 \mu\text{m}$. The same structure is shown at the same magnification in Fig. 2.1(d) after irradiation, perpendicular to the substrate, with 4 MeV Xe^{4+} ions to a fluence of $2.0 \times 10^{15} \text{ cm}^{-2}$ using a 1 MV van de Graaff accelerator. During irradiation the sample was clamped on a copper substrate that was cooled to 90 K using liquid nitrogen. The base pressure during irradiation was 5×10^{-7} mbar.

Clearly, the ion beam induced deformation has dramatically shrunk the size of the holes between the colloids. The diameter of the particle just outside the structure (marked with an arrow) increased from $1.4 \mu\text{m}$ to $2.0 \mu\text{m}$. When the deforming spheres in a mask come into contact the deformation becomes a collective process and the final dimensions are determined by the combined deformation of interacting colloids. This can be clearly seen in Fig. 2.1(d) where the shapes of the colloidal particles and the holes depend on their position in the mask. In Fig. 2.1(d), the centre-to-centre distance in the mask pattern is $1.8 \mu\text{m}$, much larger than the original spacing of $1.6 \mu\text{m}$ [Fig. 2.1(c)]. This indicates that during irradiation the expansion of the interacting colloids caused an overall expansion of the mask domain, with colloids sliding over the substrate. For large domains, buckling of the colloidal mask was observed in some cases, which we attribute to large in-plane stresses resulting from the deformation. [52]

A more open structure of silica particles is shown in Fig. 2.1(e) at a viewing angle of 10° with the substrate. The colloidal mask was irradiated with 2.0×10^{15} 4 MeV Xe^{4+} ions cm^{-2} . The average penetration depth of these ions in colloidal silica was calculated to be $1.7 \mu\text{m}$, using TRIM98, a Monte Carlo simulation program. [47] The size aspect ratio (major over minor axis) of the colloidal particles in the mask increased from 1 to 3.4. From Fig. 2.1(e) it can also be seen that the glass substrate deformed under irradiation, leading to the formation of a pedestal centered under each colloid. We attribute this to inhomogeneous anisotropic deformation of the substrate under the mask. For 4 MeV Xe^{4+} , the energy remaining after penetration through the centre of a colloid is only 0.85 MeV. As the deformation rate increases with ion energy, [53] the driving force for in-plane expansion of the substrate surface layer under the colloids will be much smaller than under the holes (where the ion energy is 4 MeV). This can lead to a plastic shape deformation of the glass substrate that causes formation of pedestals under each colloid.

To verify this hypothesis, a glass substrate covered with $1.0 \mu\text{m}$ diameter colloidal particles was irradiated with 30 MeV Cu^{5+} ions ($8.7 \times 10^{14} \text{ cm}^{-2}$) using a 6 MV tandem

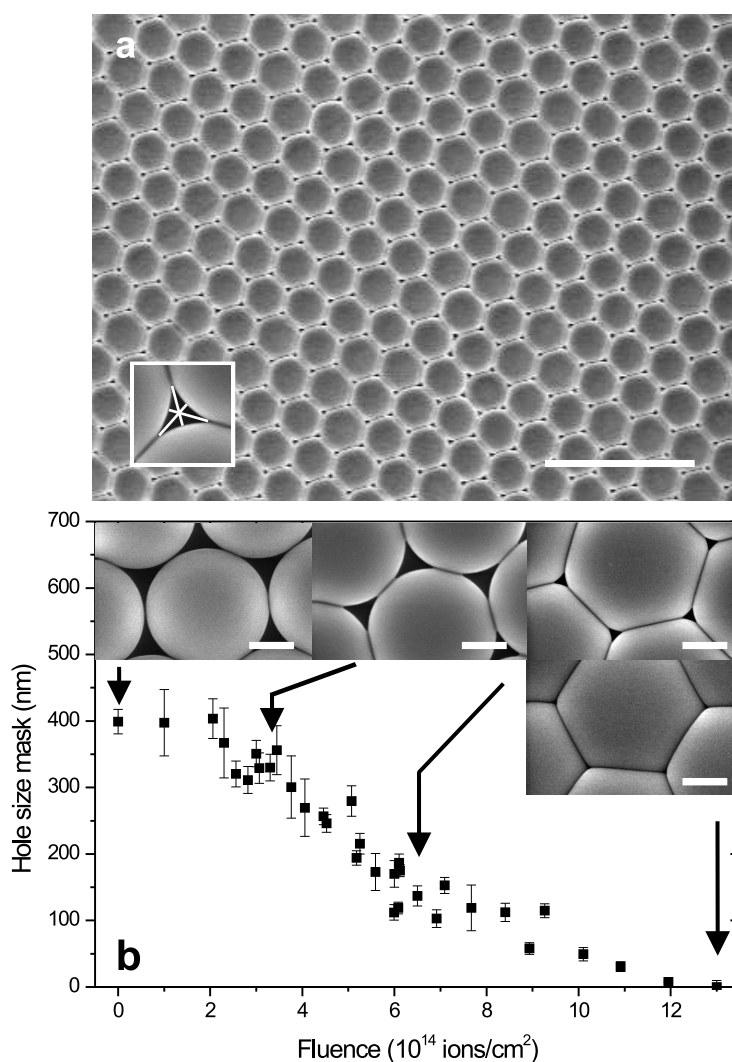


Figure 2.2: Dependence of hole size on 4 MeV Xe^{4+} ion fluence. A two-dimensional hexagonal mask of 1.4 μm diameter silica particles on a silicon substrate was irradiated with 4 MeV Xe^{4+} ions. The size of the holes gradually decreased until the holes were completely closed. The insets at the top of the image show SEM images of the mask at fluences of 0, 3.3×10^{14} , 6.5×10^{14} , and 12×10^{14} ions cm^{-2} ; corresponding hole sizes were 400, 330, 137, and 0 nm, respectively. The arrows indicate the fluences at which the images were taken. The inset in the lower left corner shows how the hole size is defined. All scale bars are 500 nm.

accelerator. The average penetration depth of these ions was calculated to be 8.6 μm . [47] At this high energy, the relative energy loss through the colloids is small, so that the substrate is irradiated at a nearly uniform energy. Indeed, under these conditions the substrate was found to stay flat.

The substrate deformation observed for 4 MeV Xe^{4+} irradiation can be avoided by using silicon as a substrate. Crystalline Si rapidly becomes amorphous under 4 MeV Xe^{4+} irradiation, and as we have recently shown, [54] the anisotropic deformation rate of amorphous silicon is about 10 times smaller than that of silica. Indeed, (amorphized) silicon substrates covered with 1.4 μm diameter silica colloids stayed flat for an ion fluence

of $2.0 \times 10^{15} \text{ Xe}^{4+} \text{ cm}^{-2}$. Figure 2.1(f) shows a silica particle on a silicon substrate after irradiation with intermediate ion fluence. It can clearly be seen that the silicon substrate remained flat while the deformation of silica particle is comparable to that of the particles in Fig. 2.1(e). While the formation of pedestals may be considered as unwanted (and can be avoided as we have shown above), we note that ellipsoidal colloidal particles on a pedestal may find use as arrays of (coupled) optical microresonators. [81]

The dependence of the size of holes in a colloidal mask on the ion fluence was determined for a two-dimensional hexagonal lattice of close-packed $1.4 \mu\text{m}$ diameter silica particles on a silicon substrate. The mask, with crystalline domains with dimensions between 20 and $50 \mu\text{m}$, was formed by self-organization during slow evaporation of a drop of a colloidal dispersion on a silicon substrate. During 4 MeV Xe^{4+} ion irradiation the sample was gradually moved along the $2.5 \times 2.5 \text{ cm}^2$ aperture through which the ion beam was scanned. A linearly varying ion fluence ranging from zero to $1.2 \times 10^{15} \text{ ions cm}^{-2}$ across the sample area was thus created. Hole sizes were determined at least five or six rows of particles away from the domain edges and an average over five holes was taken. We define the size of a hole between three colloidal particles in a hexagonal close-packed mask as the smallest distance between the point where two particles touch and a point on the surface of the third colloidal particle (see the inset in the lower left corner of Fig. 2.2(a)). As can be seen in Fig. 2.2, the hole size decreases with ion fluence, as a result of the increased in-plane particle expansion. The insets in the top of Fig. 2.2(b) show an unirradiated section of the mask, and sections irradiated with 3.3×10^{14} , 6.5×10^{14} , and $1.3 \times 10^{15} \text{ ions cm}^{-2}$. The corresponding hole sizes are 400, 330, 137, and 0 nm, respectively. Small variations in hole size observed at each fluence are attributed to polydispersity in colloid size.

To demonstrate that the ion beam deformed colloidal mask can be used to fabricate nanostructures, a 30 nm thick gold layer was deposited by electron beam evaporation (base pressure $1 \times 10^{-8} \text{ mbar}$) onto various ion irradiation-modified hexagonal masks (colloid diameter $1.4 \mu\text{m}$, 4 MeV Xe^{4+}). Subsequently, the colloidal mask was removed by sonication. As a reference, Fig. 2.3(a) shows a deposited pattern for an unirradiated mask. The size of these gold particles was 400 nm. Figures 2.3(b-d) show arrays of gold particles made using masks irradiated at 4.9×10^{14} , 7.7×10^{14} , and $11 \times 10^{14} \text{ ions cm}^{-2}$, respectively, leading to gold particle sizes of 229 nm, 119 nm, and 30 nm. The variation in nanoparticle size is 5–10%. A high-magnification image shows a Au dot with feature sizes between 15–20 nm [Fig. 2.3(e)]. As can be seen, for these small particles, inhomogeneous particle shapes are observed, which are attributed to the nucleation and growth kinetics. Thermal annealing can remove sharp features and combine metal nanoparticles that are close together. [82] Figure 2.3(f) shows a Au particle that was annealed in air at ambient pressure at 150°C for 30 minutes and subsequently at 250°C for another 30 minutes. The particle shows a more round shape and has become a single droplet-shaped particle with a diameter of about 30 nm.

To further demonstrate the versatility of the combination of optical tweezers and ion irradiation, more complex nanoparticle arrays were created by subsequent deposition of metals at different angles using an ion beam modified mask. Figure 2.3(g) shows an array of “T” structures made through subsequent silver and gold depositions through an ion-modified mask, where different depositions were done at two sets of orthogonal angles. Three silver particles were created by deposition of 11 nm silver at angles of -4.5 , 0 , and $+4.5$ degrees in a horizontal plane in Fig. 2.3(g). Two gold particles were made using a

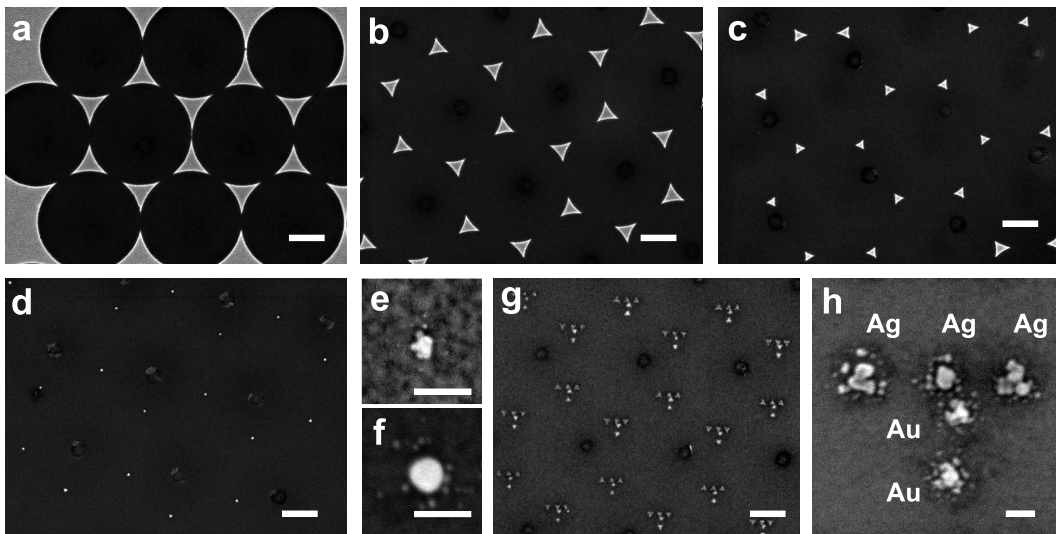


Figure 2.3: Arrays of metal nanoparticles created with an ion beam deformed mask. (a) Hexagonal array of gold particles with a size of 400 nm, created on a glass substrate using an unmodified colloidal mask of 1.4 μm diameter silica particles. (b) Hexagonal array of gold particles with a size of 229 nm, (c) 119 nm, and (d) 30 nm created with a mask modified with 4 MeV Xe^{4+} ions. (e) Image at high magnification of a Au particle with feature sizes of 15-20 nm. (f) Image of a Au particle annealed at 150°C and 250°C (both for 30 minutes). The particle has a more round and single droplet like shape. (g) Array of “T” structures with three silver and two gold nanoparticles created by deposition at different angles on a modified mask. (h) Image at high magnification of a “T” structure. The size of the particles is between 50 nm and 80 nm and their spacing is about 135 nm. Scale bar in (a-d, g) is 500 nm; in (e-f, h) 50 nm.

subsequent deposition of 10.5 nm gold at angles of -4.5 and 0 degrees in a vertical plane in Fig. 2.3(g). Figure 2.3(h) shows a single “T” structure at higher magnification. The size of the core of the deposited features was in the range 30-50 nm and the centre-to-centre interparticle spacing was about 135 nm. The spacing between the closest silver and gold nanoparticles was 62 nm. Annealing of the structure in Figs. 2.3(g) and 2.3(h), composed of both silver and gold dots, was not possible due to the different annealing kinetics of the two metals. However, metal dots in more complex structures such as “T” structures composed of a single metal are expected to change shape after annealing as shown in Fig. 2.3(f) and reference. [82] Finally, we note that during deposition the mask hole size is gradually decreasing, due to the continued deposition of metal on the colloids in the mask. Thus for very small holes, the total amount of metal that is deposited for each particle is determined by a self-limiting process.

2.4 Conclusions

We have provided a solution to two major limitations of nanosphere lithography. The geometry of the masks is extended from (self-organized) hexagonal close-packed to any desired symmetry using optical tweezers combined with critical point drying. In the present experiments colloidal particles were positioned in the mask by manual control, but the process can be fully automated to achieve a higher accuracy as well an increased

speed of patterning. Control over the hole size (independent of the size of the colloids in the mask) is achieved by ion irradiation, which causes an in-plane expansion of the mask, thus shrinking the size of the holes. By varying the ion fluence the hole size can be continuously reduced, to arbitrarily small size. In this way, hole size and spacing can be arbitrarily controlled. Recently, we have shown that deformation of colloidal spheres is also effective at ion energies below 300 keV. [53] Accelerators with such ion energies are readily available. The modified masks can be used to create arrays of nanoparticles with sizes down to tens of nanometers. Evaporation of material at different angles with respect to the mask gives additional control over structure and interparticle distance, allowing nanoparticles of different materials to be arranged with high accuracy in a variety of geometries.

Acknowledgements

Teun van Dillen is acknowledged for help with the ion irradiations; Damir Fific and Dirk Vossen for creating the templates with optical tweezers and for part of the SEM measurements. Jan Verhoeven is acknowledged for assistance with metal evaporations. Michiel de Dood, Jacob Hoogenboom, and Anna Tchebotareva are thanked for helpful discussions.

Modification of colloidal masks by wet-chemical growth

A method is presented, in which the size of the holes in colloidal masks are modified for nanolithography using a wet-chemical method. A thin layer of silica is grown on masks of silica particles. The growth mechanism of the silica coating was found to be diffusion-limited. The size of the holes can be controlled accurately using calibration and a seed dispersion. Modified masks were used for nanolithography and after metal deposition and mask removal, large arrays of nanoparticles were created. Using modified arrays of large colloidal particles (1.4 μm diameter), nanoparticles were created with a size ranging from 400 nm (for unmodified masks) down to tens of nanometers. The method is fast, simple, and inexpensive.

3.1 Introduction

In nanosphere lithography, a self-organized layer of colloidal spheres is used as a mask for a lithographic step like illumination, deposition or etching. [63–66, 73] It is a simple, fast, and inexpensive method to pattern substrates over large areas. In this Chapter, we demonstrate improvements on this technique and use the modified colloidal masks to make arrays of noble metal nanoparticles. These arrays of metal particles have many applications, [26, 59, 61] e.g., to study plasmonic resonances, [67] to fabricate plasmonic sensors, [68] to catalyze the growth of nano-fibers, [69, 70] and for selective adsorption of proteins. [71]

Nanosphere lithography also has disadvantages: for example, the size of holes in the mask are determined by the size of the colloidal particles that form the mask. Therefore, the size of the features created using nanosphere lithography is coupled to the size of the colloidal particles in the mask. [65, 66] Recently, ion beam deformation was used to control the hole size in colloidal masks. [83] [Chapter 2] Control over the hole size was also achieved by heating colloidal masks made of polystyrene colloids, and by evaporation at large off-normal angles in combination with rotation of the sample. [72, 84]

Here we present an alternative method to modify the hole size in colloidal masks for nanolithography. A wet-chemical method is used to grow a thin layer of silica on two-dimensional close-packed layers of colloidal silica particles on a substrate. The layer of silica decreases the size of the holes in the colloidal mask. We investigated the growth mechanism of the silica coating and show that the size of the holes can be controlled accurately. Modified masks were used for nanolithography: after metal deposition and mask removal, large arrays of metal nanoparticles were created. Using modified arrays of large colloidal particles with a diameter of $1.4\ \mu\text{m}$, we created nanoparticles with a size ranging from 400 nm (for unmodified masks) down to tens of nanometers.

The coating method is based on the Stöber-method [85]: a base-catalyzed reaction of alkoxy silanes in mixtures of ethanol and ammonia, which is well known for the synthesis of monodisperse colloidal silica particles. Catalyzed by the ammonia, tetra-ethoxysilane (TEOS) molecules first hydrolyze and then condense to form silica. In the early stage of the reaction small silica aggregates are formed. These coalesce until they become stable, as they grow larger and acquire more surface-charge. Once stable, the aggregates grow larger by addition of monomers and small oligomers and become spherical in shape. The final size of the colloidal spheres depends on both the number of particles formed in the early nucleation stage as well as on the amount of TEOS added to the reaction mixture. The number of particles formed in the stable suspension is a complex function of experimental conditions and is in general not accurately controllable. [76–78]

Recently, this process was modified to grow thin silica films on macroscopic surfaces. [86] Control over the thickness of the layers was achieved by addition of colloidal seeds to the reaction mixture to provide a large surface area. As in the original Stöber-process, the growth mechanism for the silica layers was found to be surface-reaction limited. [77] As a consequence, the increase in thickness of the silica layer on a macroscopic surface is equal to the increase in radius of the colloidal seed particles. Using a well-characterized seed dispersion, silica layers can be grown with nanometer control over layer thickness. [86] Here we use this method to modify colloidal masks for nanosphere lithography.

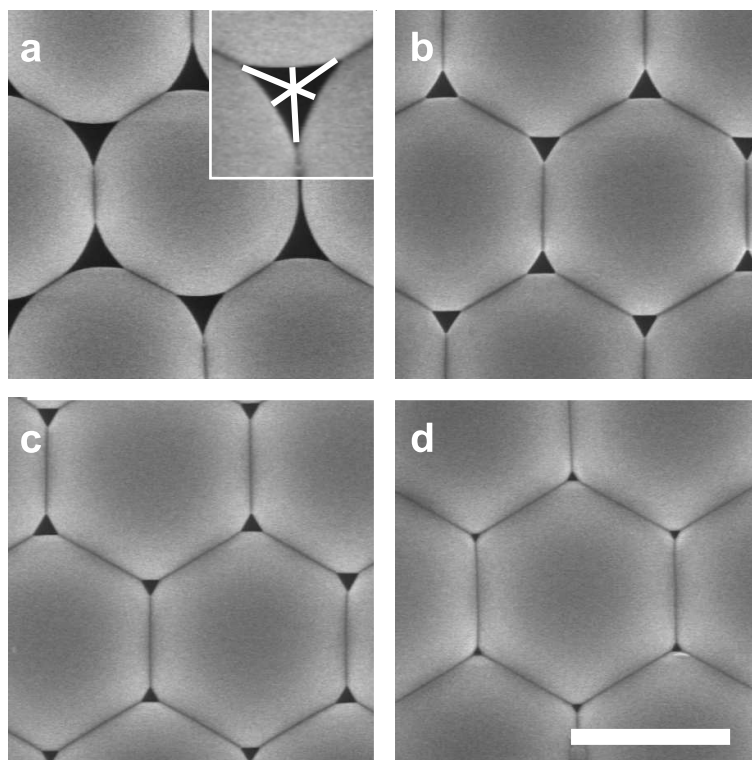


Figure 3.1: Colloidal masks formed by a layer of close-packed particles (700 nm radius), modified by growing thin layers of silica to tune the hole size. The size of the holes in an uncoated mask was 400 nm. (a) SEM image of a mask after one coating step, the size of the holes reduced to 264 nm. The inset indicates the definition of hole size. (b–d) Images of colloidal masks after two, three, and four coating steps. The size of the holes was 152 nm, 104 nm, and 55 nm respectively. The scale bar is 1 μm .

3.2 Experimental

Silica particles with a diameter of 1.4 μm and a polydispersity of 2% were synthesized using a Stöber growth process and subsequent growth steps using methods described in detail elsewhere. [76–78] The size and polydispersity were determined using scanning electron microscopy (SEM) on several hundreds of particles. Analytical grade ethanol, ammonia solution (29 wt.-%) and tetra-ethoxysilane (TEOS) from Merck were used as received. Si(100) wafers were used as substrates, as received.

First, a colloidal seed dispersion was synthesized by adding 0.360 g TEOS to a mixture of 7.867 g ethanol, 0.787 g water, and 0.715 g ammonia. After two hours of continuous stirring colloidal silica particles had formed and 75 μL dispersion was taken out of the reaction mixture. The radius of the newly formed spheres in the seed dispersion was determined to be 363 ± 8.5 nm. The number density of seed particles in the dispersion was calculated to be 2.7×10^{11} mL^{-1} .

Four substrates with colloidal masks were prepared by letting a drop of ethanol containing 700 nm radius silica colloidal particles evaporate on silicon substrates. Due to capillary forces, the particles self-organized into regions of close-packed hexagonal monolayers. The size of the holes between the particles in the colloidal mask was measured to

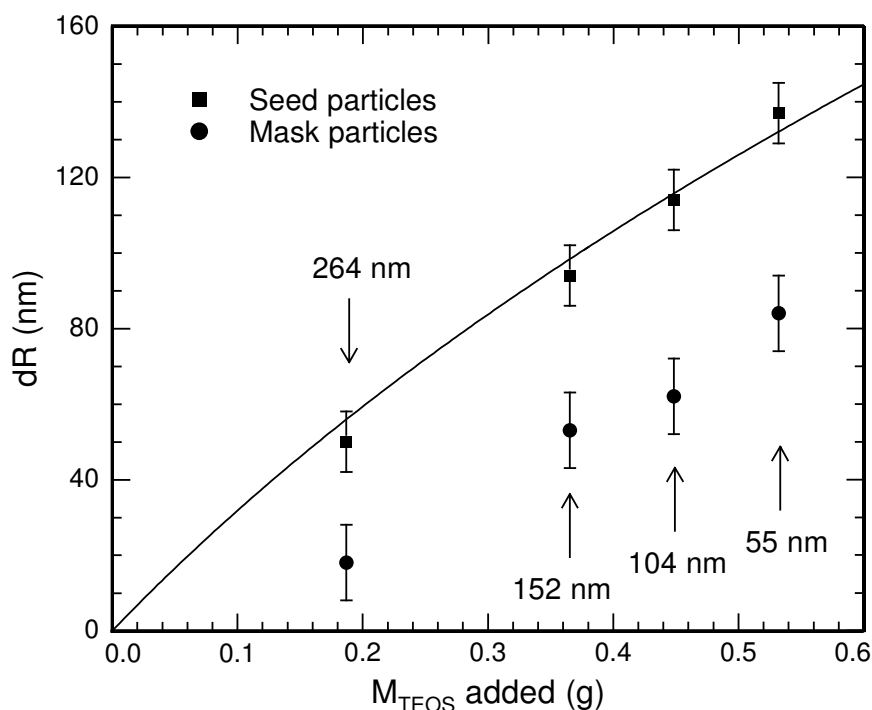


Figure 3.2: The size-increase of the seed particles in the coating mixture (squares) and the colloidal particles in the mask (circles) as a function of amount of TEOS added. The size of both particles increased, although the seed particles grew faster. For each coating step, the hole size in the mask is also indicated. The curve shows the expected relation for the surface reaction-limited growth model.

be 400 nm. The holes in the colloidal masks were characterized by measuring the three long axes of the hole's triangular shape and averaging over five holes [see the inset in Fig. 3.1(a)]. The four substrates covered with colloidal masks were then immersed in the ethanol-ammonia mixture containing the seed dispersion. Subsequently, 0.188 g TEOS was added and after two hours of stirring one substrate and 75 μL of seed dispersion were taken out of the mixture. Then, 0.178 g TEOS was added to the mixture with the seed dispersion and the three remaining substrates. After two hours, again one substrate and 75 μL of seed dispersion were taken out. These steps were repeated twice more in which 0.083 g and 0.084 g TEOS were added, respectively.

3.3 Results and discussion

Figure 3.1(a) shows a SEM image at high magnification of a colloidal mask that was taken out of the reaction mixture after the first coating step. A layer of silica was grown on the mask and the size of the holes decreased to 264 nm. This is a 136 nm reduction of the hole size compared to an uncoated mask. After the second coating the size of the holes was reduced to 152 nm [Fig. 3.1(b)]. After the third and fourth coating steps, the size of the holes was determined to be 104 nm [Fig. 3.1(c)] and 55 nm [Fig. 3.1(d)], respectively.

During the coating steps, a layer of silica was grown on the colloidal masks, the sub-

strate and on the seed colloids in the reaction mixture. The increase of the size of the particles in the mask results in a decrease of the hole size in the mask. After each growth step, the size of the seed and mask particles were determined by electron microscopy. The radius of the particles in the mask was measured on a line connecting the center of the particle and that of the hole in the mask. The graph in Fig. 3.2 shows the increase of the radius of both the seed and mask particles as a function of the amount of TEOS added. The size of the holes in the mask after each growth step is also indicated in the graph. With more TEOS added, the size of the seed particles increased more rapidly than the size of the particles in the mask.

The Stöber growth of silica colloids is well described by a surface reaction-limited model, in which the growth rate is limited by condensation of hydrolyzed monomers on the particle surface. [77, 87] The change in particle volume is then proportional to the square of the particle radius, and the increase in particle radius will be independent of size. In contrast, the growth rate in diffusion-limited growth is limited by the transport of monomers to the particle surface, the growth in particle volume is proportional to the radius of the particles. The observed difference in growth rate for seed and mask particles in Fig. 3.2 indicates that the silica growth on mask particles is more diffusion-limited than reaction-limited. Although diffusion-limited growth means that the layer thickness grown on the colloidal mask will depend on geometrical properties of the mask, which will be different for different samples, accurate tuning of the size of the holes is still possible when a calibration curve is determined.

For seeded growth, it was shown that the amount of TEOS that has to be added to increase the radius R_1 to R_2 is related to the volume of TEOS V_1 needed to prepare the particles with radius R_1 : [77]

$$V_{TEOS} = V_1 \left(\left(\frac{R_2}{R_1} \right)^2 - 1 \right). \quad (3.1)$$

Here, it is assumed that all the added TEOS grows on the existing particles and that the density of the added layer is the same as that of the core particle. This formula can be applied to the growth of the seed colloids, as the surface provided by the substrates with the masks is negligible. The result, with $R_1 = 374$ nm as determined by SEM, is shown by the solid line in Fig. 3.2, and shows a good agreement with the data.

The modified masks were then used for lithography. Figure 3.3(a) shows an array of gold nanoparticles created by deposition of 25 nm Au on a modified colloidal mask by electron beam evaporation at a base pressure of 1×10^{-8} mbar. After subsequent removal of the mask by sonication in ethanol (Branson Ultrasonic Cleaner, models 2510E and 8510E), an array of Au nanoparticles was left on the substrate. Sometimes, masks coated with a thick silica layer were found to be hard to detach from the substrate. The size of the nanoparticles in Fig. 3.3(a) was determined to be 70 nm. Since the substrate was also coated during the coating, the metal nanoparticles were deposited on a thin layer of silica. Where the colloidal mask touched the silicon substrate, indentations in the silica film can be seen.

To investigate the height-profile of a sample, an array of Au particles was imaged using an atomic force microscope [Fig. 3.3(b)]. The Au particles had a lateral size of 310 nm. Height profiles recorded on the two dashed lines indicated in Fig. 3.3(b) are plotted in Fig. 3.3(c). Each line shows two Au particles on the silica layer on top of the

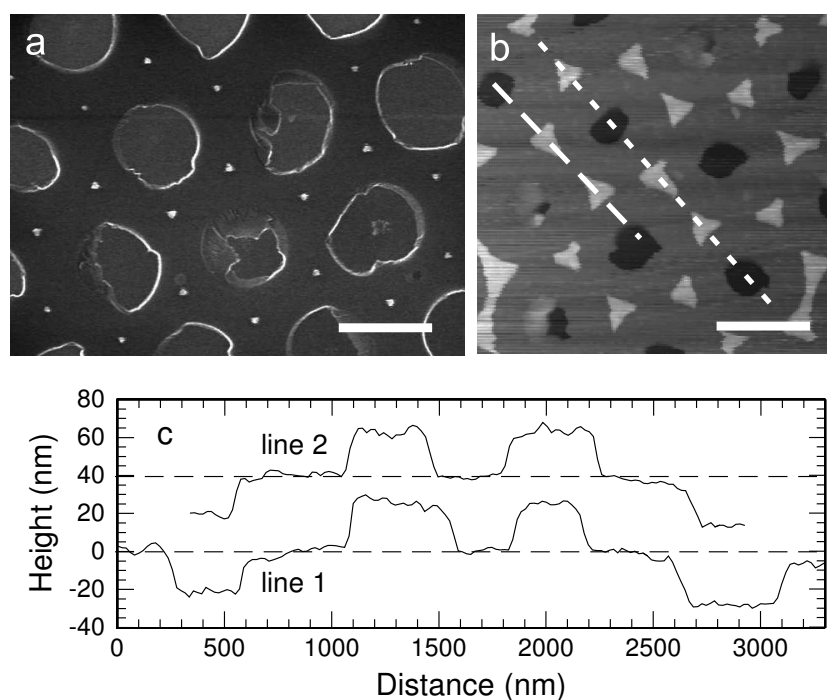


Figure 3.3: (a) SEM image of an array of gold nanoparticles created by deposition of 20 nm Au on a modified colloidal mask and subsequent mask removal by sonication of the sample. The in-plane size of the nanoparticles was 70 nm. (b) AFM image of an array of Au particles (350 nm) on a silica layer. The holes in the silica layer are caused by the particles in the mask during the coating. (c) Height profile over two Au particles on the silica layer on the silicon substrate. The thickness of the Au particles was 27 nm while the silica layer has a thickness of 29 nm. The position where the profile was taken is indicated in Fig. 3.3(b) with a dashed line. The scale bars are 1 μm .

silicon substrate. On average, the height of the Au particles was 25 nm while the silica layer had a thickness of 29 nm. For many applications, the presence of silica on the substrate poses no problem. However, modification of the surface can be prevented when the method is used on freestanding colloidal masks that are then transferred to a substrate for lithography. [66] We have shown previously that silica can be grown on many different materials (including latex spheres) using the polymer poly(vinylpyrrolidone), so that this modification method can be applied to a variety of substrates and colloidal masks. [88]

Another method to modify the size and shape of the holes is given in Fig. 3.4(a). [89] It shows a zoomed-in SEM image of small silica particles on top of larger ones. The small particles modify the size and shape of the hole in the mask of large particles. A 20 nm thick Ag layer was deposited on top of the mask. Figure 3.4(b) shows the substrate after the mask was removed. The three elongated Ag particles (on the left; oriented at an angle of 120 degrees) were created through a hole in the mask that was partially blocked by a small particle. The small Ag particle on the right was deposited through a hole, which was modified by three particles in a hole in the mask. Using controlled-drying methods, [90] large areas of binary crystals can be created that can then be used as masks for nanolithography. [65, 91] The irregular shape of the small metal particles as observed in Fig. 3.4(b) are attributed to a combination of nucleation and growth kinetics and imperfect wetting of the substrate by the metal. Thermal annealing makes the shapes more regular [82] as

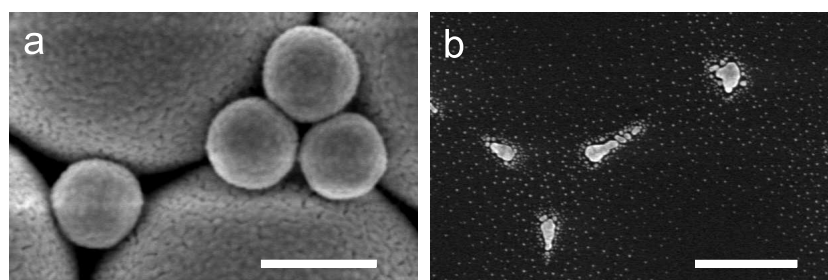


Figure 3.4: (a) SEM image at high magnification of an arrangement of small silica particles on top of larger ones. The small particles modify the size and shape of the hole in the mask. A 20 nm thick layer of Ag was deposited on the mask. (b) Ag particles created on the substrate by evaporation through a mask of large and small particles. The scale bars are 1 μm .

was also shown in Chapter 2.

3.4 Conclusions

In conclusion, we developed a method to modify the hole size of colloidal masks used for lithography. A mask is coated with a thin silica layer in the presence of a seed dispersion of silica colloids. This method allows accurate tuning of the size of the holes by the amount of TEOS added. As an example, the modified masks were used to create arrays of metal nanoparticles. The method is inexpensive, simple, and fast. The method can be used in combination with the techniques described in Chapter 2.

Acknowledgements

This work was done in close collaboration with Dirk Vossen. Anna Tchebotareva is acknowledged for help with the AFM measurements.

Part II

Metal cores

MeV ion beam deformation of metal colloids in silica

The deformation of metallo-dielectric core/shell colloids is studied under 4 MeV Xe⁴⁺, 6 MeV Au³⁺, 30 MeV Si⁵⁺, and 30 MeV Cu⁵⁺ ion irradiation. In colloids consisting of a Au core and a silica shell, the silica expands perpendicular to the ion beam, while the metal core shows a large elongation along the ion beam direction, provided the silica shell is thick enough (> 40 nm). A minimum electronic energy loss of 3.3 keV/nm is required for shape transformation of the metal core. Silver cores embedded in a silica shell show no elongation, but rather disintegrate. Also in planar SiO₂ films, Au and Ag colloids show entirely different behavior under MeV irradiation. We conclude that the deformation model of core/shell colloids must include ion-induced particle disintegration and solubility effects, possibly in combination with mechanical effects driven by stresses around the ion tracks.

4.1 Introduction

Amorphous materials subject to MeV ion irradiation can undergo anisotropic plastic deformation at constant volume. [48] The deformation is well described by a viscoelastic model, in which the thermal expansion of the cylindrically-shaped high-temperature ion track region causes shear stresses that relax by viscous flow, with the viscous strains subsequently frozen in upon rapid cooling of the ion track region. [56, 57] The deformation is induced by electronic energy loss, and thus occurs most efficiently with ions in the MeV energy range.

One of the most striking examples of this effect is the deformation of colloidal particles under MeV ion irradiation. [58, 92] Spherical silica colloids expand perpendicular to the ion beam and contract parallel to the ion beam changing their shape to oblate ellipsoidal. This ion beam deformation technique provides a unique method to tailor the shape of colloidal particles and aggregates. For example, prolate ellipsoids can be made by using subsequent ion irradiations from different directions. [58] Also, the optical properties of three-dimensional colloidal photonic crystals can be tailored by ion beam deformation. [93] And recently, we demonstrated how a colloidal mask for nanolithography can be modified by MeV ion irradiation. [83] (Chapter 2)

In general, amorphous materials (insulators, semiconductors or metallic glasses) show anisotropic deformation under MeV ion irradiation. [49–51] In contrast, pure crystalline metals do not show anisotropic deformation. [48, 55] This is attributed to the fact that epitaxial recrystallization at the solid-liquid ion track interface would restore the initial crystalline state, without anisotropic deformation. It has also been suggested that the ion track temperature in crystalline metals does not exceed the melting temperature as a result of rapid redistribution of the deposited energy in the electronic subsystem. [94]

Given the entirely different behavior of metals and silica glass under MeV ion irradiation, it is interesting to study the deformation effect on assemblies in which silica and metal are in intimate contact. In this Chapter, we study the ion irradiation-induced deformation of colloidal particles composed of a metal core with a silica shell. We show that, while single Au colloids do not show deformation, the presence of a silica shell induces a shape change on the metal. We compare data for freestanding core/shell colloids with the deformation of Au and Ag colloids that are embedded in a bulk SiO₂ film and with recent work by D'Orléans *et al.* on Co colloids in SiO₂ films. [95–98]

The motivation for this work is two-fold. First, metallo-dielectric colloids form a new class of interesting building blocks for photonic applications that critically depend on the particle shape. Ion irradiation-induced deformation provides a unique tool to tailor the optical properties. Second, studies of metallo-dielectric composites could provide information on fundamental aspects of ion-solid interactions in both silica and metal. This paper focuses on the latter.

4.2 Experimental

Au-core/silica-shell colloids were grown using Au colloids with a diameter of 14 nm as a starting point. These colloids were synthesized via the standard sodium citrate reduction method. A silica shell was then grown via functionalization of the Au particles by polyvinylpyrrolidone, after which the colloids were transferred into ethanol to enable

	4 MeV Xe ⁴⁺		6 MeV Au ³⁺		30 MeV Si ⁵⁺		30 MeV Cu ⁵⁺	
	S _e	S _n	S _e	S _n	S _e	S _n	S _e	S _n
silica	1.50	0.79	2.47	1.41	3.34	0.005	5.85	0.04
Au	2.64	3.39	4.82	6.44	10.5	0.02	16.8	0.18
Ag	2.80	2.53	4.65	4.70	8.6	0.02	14.4	0.13

Table 4.1: Overview of electronic and nuclear energy losses S_e and S_n in keV/nm for 4 MeV Xe⁴⁺, 6 MeV Au³⁺, 30 MeV Si⁵⁺ and 30 MeV Cu⁵⁺ ions in silica (density 2.0 g/cm³), gold and silver.

Stöber growth of the silica shell. [99] Using a similar process, Ag cores were coated with silica. After synthesis, a droplet of the colloidal suspensions was dried on a Si(100) substrate under nitrogen flow, so that the typical surface coverage was well below a monolayer. For transmission electron microscopy (TEM) analysis, colloids were deposited on a 10-nm thick Si₃N₄ membrane embedded in a silicon wafer.

Au and Ag colloids were also synthesized in planar SiO₂ films, made by thermal oxidation of a silicon substrate. Multiple-energy Au and Ag implants were used with energies in the range 45–200 keV to yield constant Ag or Au depth profiles at a concentration of 1.6×10^{21} cm⁻³. Spherical colloids were then formed in SiO₂ by thermal annealing at 500°C (Ag) or 1150°C (Au).

Ion irradiation was performed using Van de Graaff tandem accelerators in Utrecht, Montreal and Rossendorf. The samples were mounted onto a copper substrate holder that was cooled to 77 K using liquid nitrogen, since the largest anisotropic deformation is observed at low temperatures. [53, 100] The ion beam was electrostatically scanned across an area of typically a few cm². Electron microscopy (SEM: 5–30 keV, and TEM: 120–200 keV) was used to determine the particles' size and shape before and after ion irradiation.

4.3 Results and discussion

4.3.1 Au-core/silica-shell colloids

Figure 4.1(a) shows a TEM image of a spherically-shaped Au-core/silica-shell particle with a Au core diameter of 14 nm and a silica shell thickness of 75 nm. A TEM image of a collection of these colloids after irradiation with 30 MeV Cu⁵⁺ ions (1×10^{15} cm⁻²) is shown in Fig. 4.1(b). The ion beam direction is schematically indicated by the arrow. Clearly, during irradiation the silica shell has turned into the expected oblate ellipsoidal shape. The Au core however, has deformed in an entirely different manner: it is effectively elongated along the ion beam and narrowed perpendicular to the beam. [101] The typical length of the Au rods observed in the image is 35–50 nm. Assuming volume conservation this translates into a size aspect ratio of about 6.

This intriguing deformation effect was studied further by irradiations with other ions than Cu. Figure 4.1(c) shows a TEM image of core/shell colloids (Au diameter $d_{Au} = 15$ nm, silica shell thickness $t_{silica} = 65$ nm) after irradiation with 4×10^{14} Xe⁴⁺ cm⁻². Again, clear deformation of the silica shell is observed, but no measurable shape change

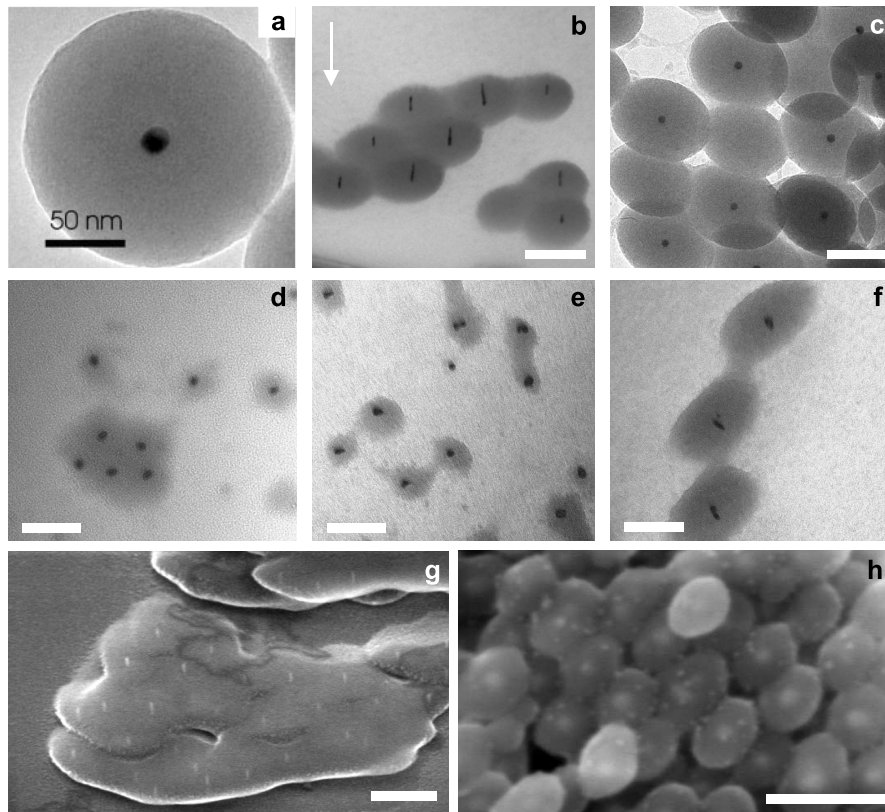


Figure 4.1: TEM (a-f) and SEM (g-h) images of (a) Au-core/silica-shell colloid ($d_{Au} = 14$ nm, $t_{silica} = 72$ nm); (b) Au-core/silica-shell colloid ($d_{Au} = 14$ nm, $t_{silica} = 65$ nm) after 30 MeV Cu^{5+} irradiation ($1 \times 10^{15} \text{ cm}^{-2}$); (c) Au-core/silica-shell colloid ($d_{Au} = 15$ nm, $t_{silica} = 72$ nm) after 4 MeV Xe^{4+} irradiation ($4 \times 10^{14} \text{ cm}^{-2}$); (d,e,f) Au-core/silica-shell colloids ($d_{Au} = 14$ nm, $t_{silica} = 26$ nm (d), 39 nm (e), 72 nm (f)) after 30 MeV Cu^{5+} irradiation ($2 \times 10^{14} \text{ cm}^{-2}$); (g) Au-core/silica-shell colloids ($d_{Au} = 15$ nm, $t_{silica} = 65$ nm) after 30 MeV Cu^{5+} irradiation ($2 \times 10^{15} \text{ cm}^{-2}$); (h) Ag-core/silica-shell colloids ($d_{Ag} = 26$ nm, $t_{silica} = 47$ nm) after 30 MeV Si^{5+} irradiation ($4.7 \times 10^{14} \text{ cm}^{-2}$). Scale bars 50 nm (a), 100 nm (b-f) or 200 nm (g, h).

of the Au core is found. This indicates that the deformation mechanisms of metal core and silica shell are not directly related. Additional experiments using 30 MeV Si^{5+} ions also showed no deformation of the Au core. In Table 4.1 the electronic and nuclear energy losses for 4 MeV Xe^{4+} , 6 MeV Au^{3+} , 30 MeV Si^{5+} , and 30 MeV Cu^{5+} ions are listed for irradiations in silica, Ag and Au. [47] Comparing these numbers, we find an electronic energy loss threshold (in the silica) for deformation of the Au core of $S_e^{th} > 3.3$ keV/nm. Note that, as we have shown earlier, anisotropic deformation of (colloidal) silica shows no measurable threshold ($S_e^{th} < 0.4$ keV/nm). [53]

To study this in more detail, a series of core/shell particles was made with different silica shell thicknesses. Figures 4.1(d,e,f) show TEM images of particles with a 14-nm thick Au core, embedded in silica shells with a thickness of about 30 nm (d), 40 nm (e), or 70 nm (f) after 30 MeV Cu^{5+} irradiation. For the latter shell thickness a clear elongation of the Au cores is observed. * This indicates that the deformation of the metal core

*Note that in Fig. 4.1(f) not all elongated Au cores seem aligned in the same direction. This is attributed

is somehow related to ion-induced effects in the silica shell. An additional observation of similar nature, published in Ref. [101], is that for core/shell particles of equal size and shell thickness the deformation of the metal core depends on the local surroundings of the particles: particles that are stacked two or three layers thick and are in contact before irradiation exhibit significantly larger deformation of the metal core than isolated particles. From these two independent experiments (varying shell thickness and varying colloid contact) we conclude that the Au core deforms more efficiently when more silica surrounds it.

Figure 4.1(g) shows an SEM image of a two-dimensional array of Au-core/silica-shell particles ($d_{Au} = 15$ nm, $t_{silica} = 65$ nm) that was irradiated with 30 MeV Cu^{5+} (2×10^{15} cm^{-2}). Clearly, at this high fluence the silica shows large deformation, and the colloids have completely flown together. The Au cores, however, again show a clear elongation along the ion beam, leading to the formation of a regular array of aligned Au nanorods with lengths as long as 30 nm.

Next, we study the irradiation of core/shell colloids composed of a silver core and a silica shell. Figure 4.1(h) shows an SEM image of a Ag-core/silica-shell colloid ($d_{Ag} = 26$ nm, $t_{silica} = 47$ nm) after 30 MeV Si^{5+} irradiation to a fluence of 4.7×10^{14} cm^{-2} . An entirely different effect is observed for Ag than for the Au cores described above: the Ag cores have disintegrated and reassembled in small nanoparticles that seem to preferentially form at the colloid's surface. The difference between the ion irradiation effects on Au and Ag cores is striking and provides a hint that the mechanism for elongation of the metallic cores may include effects of melting and vaporization of the metal, as well as diffusivity and solubility of the metal in the glass matrix. Disintegration of small Co clusters (radius smaller than 6–8 nm) and anisotropic deformation of larger Co clusters in silica was also observed by D'Orléans *et al.* for 200 MeV I irradiations. [95] The effects are ascribed to the fragmentation or deformation creep of the clusters in the thermal spike region. In another study, Heinig *et al.* [102] also observed disintegration of nanoparticles under ion irradiation. They attributed this to an “inverse Ostwald ripening process” that can occur under particular conditions of ion irradiation kinetics and thermodynamics. The ion beam-induced disintegration of the Ag cores is then related to the large solubility and particular bonding nature of Ag in the silica network. Moreover, Bernas *et al.* [103] have found that ion irradiation-induced nucleation and growth of Ag nanoparticles in silica glass has a strong thermodynamically driven component.

One model that we have proposed earlier to explain the elongation of the Au core is an indirect deformation scenario in which the in-plane strain generated by ion tracks in the silica shell imposes a stress on the metal core. [101] With the metals being relatively soft under ion irradiation, this in-plane stress may then cause the metal core to flow in the out-of-plane direction, i.e., along the direction of the ion beam, by Newtonian viscous flow. This argument seems consistent with the fact that larger elongation is found for colloids with a thicker silica shell, or for colloidal assemblies that are more closely packed. [101] The fact that entirely different electronic stopping thresholds are found for elongation of the Au core ($S_e^{th} > 3.3$ keV/nm) and the deformation of the silica shell ($S_e^{th} < 0.4$ keV/nm) implies that this indirect deformation model is too simple, unless a radiation-induced Newtonian flow mechanism is invoked in which the metal would only flow above a particular threshold electronic energy loss. However, we have shown

to the fact that the TEM grid has wrinkled somewhat during irradiation

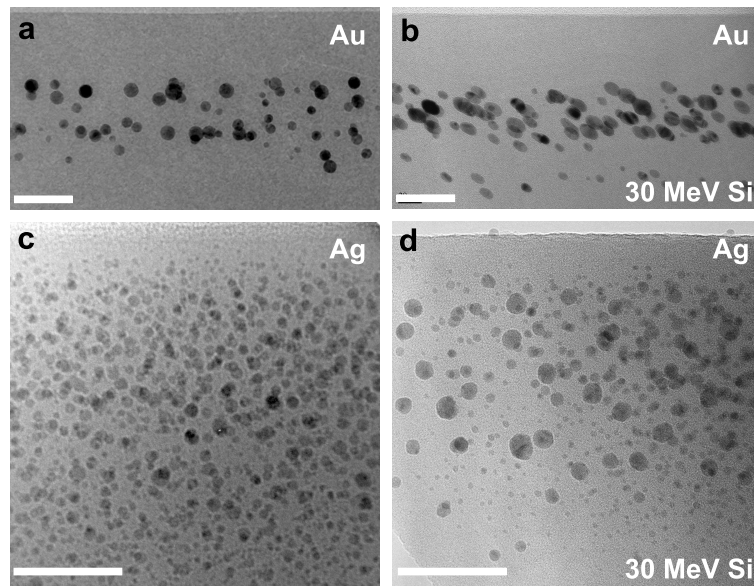


Figure 4.2: Cross-section TEM images of: (a) Au colloids in SiO₂ formed by Au ion implantation (peak concentration $1.6 \times 10^{21} \text{ cm}^{-3}$) followed by thermal annealing at 1150°C (1 hr.); (b) same as (a), after irradiation with 30 MeV Si⁵⁺ ($9.3 \times 10^{14} \text{ cm}^{-2}$) at an angle of 60° off-normal; (c) Ag colloids in SiO₂ formed by Ag ion implantation (peak concentration $1.6 \times 10^{21} \text{ cm}^{-3}$) followed by annealing at 500°C (1 hr.); (d) same as (c), after irradiation with 30 MeV Si⁵⁺ ($9.3 \times 10^{14} \text{ cm}^{-2}$) at an angle of 60° off-normal. Scale bars 50 nm.

previously that radiation-induced viscous flow is an effect that is determined by energy deposition in atomic displacements, rather than electronic excitations. [52] It would thus be less efficient for 30 MeV Cu⁵⁺ irradiation than for 4 MeV Xe⁴⁺ or 30 MeV Si⁵⁺ irradiation, contrary to what is observed. This implies that the indirect deformation scenario does not seem consistent with the data. Most likely, ion-induced particle disintegration in combination with thermodynamical effects play a role, possibly in combination with mechanical effects driven by stresses around the ion tracks. Recent experiments by Vredenberg *et al.* on the deformation of colloidal Au particles embedded in planar SiO₂ films will shed further light on this issue. [104]

4.3.2 Au and Ag colloids in planar SiO₂ films

To further study the different behavior of Au and Ag, we prepared Au and Ag colloids in planar SiO₂ films, using ion implantation and thermal annealing. Figures 4.2(a,c) show cross-section TEM images of the Au and Ag doped layers after implantation and thermal annealing. The Au implanted sample shows Au colloids arranged in two bands, centered at depths of 80 nm and 100 nm, with typical colloid diameters of 5–20 nm. The Ag implanted sample shows a large density of much smaller colloids.

After irradiation with 30 MeV Si⁵⁺ ($9.3 \times 10^{14} \text{ cm}^{-2}$) at an angle of 60° relative to the surface normal, clear deformation of the Au colloids is observed [Fig. 4.2(b)]. Similar to what is observed for the Au-core/silica-shell colloids [Figs. 4.1(b,f,g)], the Au elongates along the ion beam. A typical size aspect ratio of 2 is observed. Figure 4.2(d) shows the Ag doped sample after irradiation under the same conditions. No deformation of the Ag

colloids is observed. This again indicates that thermodynamical effects are likely to play a role in the deformation mechanism.

4.4 Conclusions

In Au-core/silica-shell colloids, the silica expands perpendicular to the ion beam, while the metal core shows a large expansion along the ion beam direction, provided the silica shell thickness is large enough (> 40 nm). By comparing experiments at different ion energies it is concluded that the metal deformation only occurs above an electronic energy loss threshold in the silica of about 3.3 keV/nm. Silver cores embedded in a silica shell do not show elongation, but rather disintegrate. Also in planar SiO₂ films, Au and Ag colloids show an entirely different behavior. We conclude that the deformation model must include ion-induced particle disintegration in combination with thermodynamic effects, possibly in combination with mechanical effects driven by stresses around the ion tracks.

Acknowledgements

The colloidal particles were made by Christina Graf. Some of the irradiations of Fig. 4.1 were done by Sjoerd Roorda (University of Montréal) and Teun van Dillen. Bart Kooi (Groningen University) is gratefully acknowledged for TEM analysis in the early phase of this work, Frans Tichelaar (Delft University) is gratefully acknowledged for TEM analysis in Section 4.3.2. We also happily acknowledge many stimulating discussions with Karl-Heinz Heinig (Research Center Rossendorf), Harry Bernas (CSNSM, Orsay) and Marcel Toulemonde (Caen).

MeV ion induced anisotropic plasmon resonances of Ag nanocrystals in glass

Ion irradiation of silica glass containing Ag nanocrystals with 30 MeV Si^{5+} ions results in an alignment of Ag nanocrystals in arrays along the ion tracks. Optical transmission measurements show a large splitting of the surface plasmon resonance bands for polarizations longitudinal and transverse to the arrays. The splitting is in qualitative agreement with a model for near-field electromagnetic plasmon coupling within the arrays. Resonance shifts as large as 1.5 eV are observed, well into the near-infrared.

5.1 Introduction

The interaction of light with small metal clusters embedded in a dielectric medium has been investigated extensively for many years. [37] Nanometer-sized clusters of noble metals in glasses exhibit strong absorption of visible light, due to collective motions of the free electrons which are called surface plasmons. The resonance frequency in spherical, non-interacting clusters depends on the size and the dielectric constants of the metal and the surrounding medium. In ensembles of particles, electromagnetic coupling among particles causes plasmon bands to shift. [42] Numerical simulations showed the effect of particle size, next-neighbor distance, number of particles and shape of aggregates on the extinction spectra of aggregates of nanometer-sized silver spheres. [43] Significant plasmon blue- and red-shifts are predicted for strongly coupled ensembles. Very recently, it was shown experimentally that such interacting metal nanoparticles can serve as miniature waveguides in which electromagnetic energy can be transported via a dipolar near-field interaction. [17]

It is thus clear that nanoscale arrangements of metallic particles in glass are of great interest to study the fundamentals of plasmon interactions on small length scales. By tuning the inter-particle interaction and particle shape, the plasmon resonance can be shifted to a wavelength of $1.5 \mu\text{m}$. This may enable several applications in telecommunications, including polarization-dependent waveguides and non-linear optical devices which take advantage of the high electromagnetic fields in plasmonic structures.

Recently, we have shown that anisotropic metal colloids can be fabricated controllably by MeV ion irradiation of colloidal particles which consist of a gold core surrounded by a silica shell. [101] This shape change is attributed to an anisotropic deformation effect in the silica that is known to occur in amorphous materials. [58] In this letter, we describe the effect of MeV ion irradiation on silver nanocrystals embedded in a planar sodalime glass film. Optical transmission data show polarization-dependent plasmon bands of silver, with red- and blue-shifts occurring for polarizations parallel and orthogonal to the irradiation axis, respectively. The splitting is attributed to an ion beam induced alignment of the Ag nanocrystals into linear arrays and can be tuned by varying the ion fluence.

5.2 Experimental

Silver nanocrystals were made in a sodium-containing borosilicate glass by a combination of $\text{Na}^+ \leftrightarrow \text{Ag}^+$ ion exchange and ion irradiation. [105] A 1 mm thick Schott BK7 glass wafer was immersed in a salt melt containing 5 mol% AgNO_3 in NaNO_3 . One sample was ion exchanged for 7 minutes at 310°C , other samples for 10 minutes at 350°C . After the ion exchange, Ag nanocrystals were nucleated by an 1 MeV Xe^+ irradiation (normal incidence, room temperature, $1 \times 10^{16} \text{ cm}^{-2}$). This nanocrystal formation process is well-documented and ascribed to the enhanced mobility of Ag^+ ions due to atomic displacements caused by the ion beam. [105, 106] Subsequently, the samples were subjected to a 30 MeV Si^{5+} ion beam at 77 K under an angle of 60° off-normal. Si^{5+} ions at this high energy exhibit very high electronic energy loss, a prerequisite for anisotropic deformation processes which are thought to be caused by the highly anisotropic thermal spike along the ion trajectory. The Si^{5+} beam flux was in the range of $(1-5) \times 10^{11} \text{ cm}^{-2}\text{s}$. Fluences were chosen between 0 and $3 \times 10^{15} \text{ cm}^{-2}$. Note that the fluences projected normal

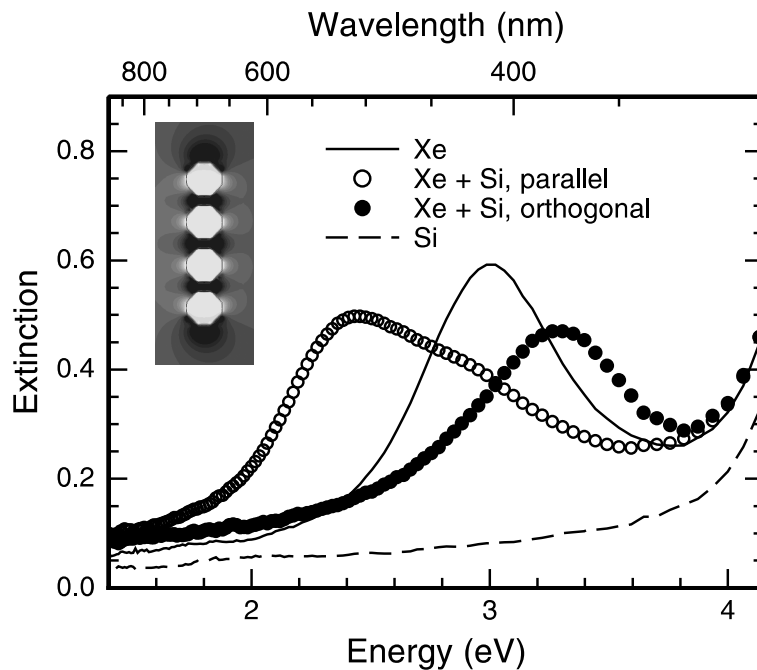


Figure 5.1: Optical extinction spectra of Ag ion exchanged BK7 glass samples irradiated with 1 MeV Xe^+ (drawn line) to form Ag nanocrystals, and with subsequent 30 MeV Si^{5+} at an angle of 60° off-normal (circles), using normal-incidence light. The Si^{5+} irradiation ($2 \times 10^{14} \text{ cm}^{-2}$) causes a large split in the plasmon bands for polarizations transverse (closed circles) and longitudinal (open) to the direction of the Si^{5+} beam as projected onto the surface. The inset shows a representative time snapshot of the electric field amplitude distribution obtained from a FDTD simulation with enhanced field amplitudes both inside (white, positive field) and between (black, negative field) the Ag particles.

to the surface are half these values.

Rutherford backscattering spectrometry was performed to determine the composition of the glass after the ion exchange. The Ag surface concentration is ~ 6 at.%, and the depth profile extends to 600 nm for a 7 min./ 310°C ion exchange and to 1100 nm for a 10 min./ 350°C condition. The projected range of 1 MeV Xe^+ , i.e., the depth over which silver nanocrystals are formed, is 360 nm. Simulations [47] indicate that at an incoming angle of 60° the projected range of 30 MeV Si^{5+} amounts to $4.8 \mu\text{m}$, which is well beyond the depth of the ion exchanged region.

Optical transmission spectra were taken with a spectroscopic ellipsometer at normal incidence. Transmission electron microscopy (TEM) images were taken using a 400 keV electron beam. Preparation of plan-view TEM samples was done using a conventional backthinning method by polishing and ion milling using a 4 keV Ar ion beam under an angle of 6° with the surface.

5.3 Results and discussion

Figure 5.1 shows the optical extinction versus energy of the samples made by the 7 min./ 310°C ion exchange. After the initial Xe^+ irradiation, the ion exchanged glass shows an

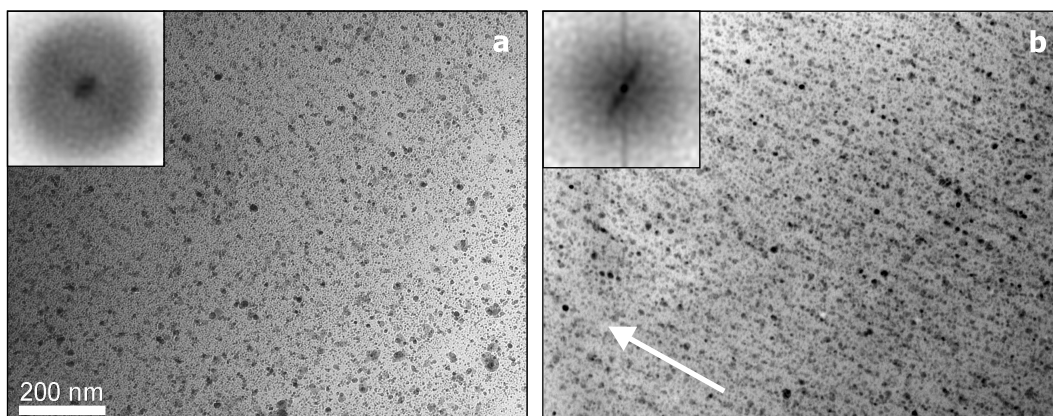


Figure 5.2: Plan-view TEM images of Ag^+ ion exchanged BK7 glass after 1 MeV Xe^+ (a), and after subsequent 30 MeV Si^{5+} ion irradiation (b). Scales of (a) and (b) are identical. The ion beam was at 60° off-normal and its projection onto the surface is indicated by an arrow. Clear alignment of Ag nanocrystals is observed along the ion beam direction. The insets show the spatial Fourier transform of the images (full scale 0.3 nm^{-1}).

extinction peak at 3.0 eV (410 nm), due to the surface plasmon absorption of Ag nanocrystals in a BK7 glass matrix (refractive index 1.61). This absorption band is polarization independent, as expected. From a fit of Mie theory to the spectrum, [105] it is estimated that approximately 11% of the Ag^+ ions have agglomerated into nanocrystals. After Xe^+ irradiation the glass shows a bright yellow color. After the subsequent irradiation with 30 MeV Si^{5+} ions to a fluence of $2 \times 10^{14} \text{ cm}^{-2}$, the color of the glass changed to red and is now angle-dependent. This is confirmed by the optical extinction measurements shown in Fig. 5.1, taken using normal-incident light polarized either parallel (open circles) or orthogonal (closed circles) to the direction of the Si^{5+} beam projected onto the surface. Also shown in Fig. 5.1 is a reference measurement for an Ag^+ ion exchanged sample that was irradiated with Si^{5+} only; it does not show a plasmon absorption band and is colorless.

Plan-view TEM images are shown in Fig. 5.2, taken under normal incidence. Figure 5.2(a) shows the Ag nanocrystals formed after 1 MeV Xe^+ irradiation, with typical diameters in the range 2–15 nm, randomly distributed in the glass. Figure 5.2(b) shows data taken after Xe^+ and Si^{5+} irradiations: randomly oriented Ag nanocrystals are observed, but in addition, arrays of aligned nanoparticles are found. These arrays are along the direction of the ion tracks (arrow). The redistribution of Ag is ascribed to the effect of the thermal spike of the 30 MeV Si^{5+} ions, possibly in combination with anisotropic strain generated along the track. [107] The anisotropy is also observed in the spatial Fourier transform (inset) of Fig. 5.2(b), in contrast to that of Fig. 5.2(a). Note that no clear shape change is observed, as was seen for Au cores in silica colloids. [101]

The splitting of the plasmon bands observed in Fig. 5.1 can be explained by electromagnetic coupling among the aligned nanocrystals. [43] For polarizations parallel to the particle array, such coupling is known to result in a red-shift. Conversely, transverse polarization will result in a blue-shift. Finite-difference time domain (FDTD) simulations of arrays similar to those observed in Fig. 5.2(b) show that the splitting due to the coupling can be well over 1 eV. As an example, a representative time snapshot of the electric field

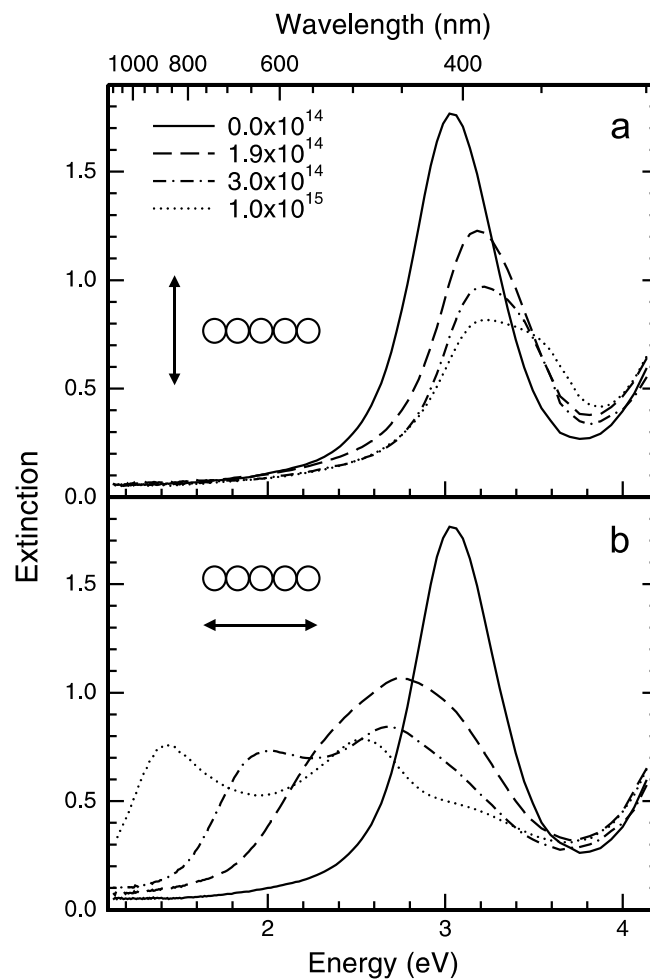


Figure 5.3: Optical extinction spectra for Ag^+ ion exchanged and Xe^+ irradiated BK7 glass irradiated with 30 MeV Si^{5+} at different ion fluences up to $1 \times 10^{15} \text{ cm}^{-2}$ (indicated in the figure). The polarization of the incoming light is transverse (a) or longitudinal (b) to the irradiation direction projected onto the surface. The splitting of the plasmon band can be tuned by changing the ion fluence and a shift well into the near-infrared is observed.

amplitude distribution obtained from FDTD simulation of a four Ag nanoparticle array is shown as an inset in Fig. 5.1. The strongly enhanced field between adjacent particles is indicative of strong interparticle coupling. Details of the simulation with quantitative results are presented in Chapter 6. [108]

The plasmon band shift can be tuned by varying the Si^{5+} ion fluence, as is illustrated in Fig. 5.3. Here optical extinction spectra are shown for Si^{5+} fluences up to $1 \times 10^{15} \text{ Si}^{5+} \text{ cm}^{-2}$ (10 min./ 350°C). With increasing Si^{5+} fluence, the plasmon absorption band for the transverse polarization is blue-shifted [Fig. 5.3(a)], whereas the plasmon absorption band for the longitudinal polarization is red-shifted [Fig. 5.3(b)]. At a fluence of $1 \times 10^{15} \text{ Si}^{5+} \text{ cm}^{-2}$ a red-shift by as much as 1.5 eV is observed, well into the near-infrared (870 nm). Another feature to notice in Fig. 5.3(b) is a second absorption band around 2.5 eV for high Si^{5+} fluences. We attribute this to the formation and alignment of new Ag nanocrystals during the Si^{5+} irradiation, and to the growth of existing nanocrystals. Note that after the original Xe^+ irradiation, only 10% of the Ag^+ ions are incorporated into nanocrystals,

while 90% remain in solution. The slight difference in shape of the extinction spectra for Si^{5+} fluences of $2 \times 10^{14} \text{ cm}^{-2}$ in Fig. 5.1 and Fig. 5.3 is attributed to different ion exchange conditions for the two cases, resulting in different Ag depth profiles. A next challenge is to further increase the Si^{5+} ion fluence and investigate if the plasmon resonance can be shifted further, into the important telecommunication bands around $1.3 \mu\text{m}$ and $1.5 \mu\text{m}$.

5.4 Conclusions

In conclusion, we have shown that 30 MeV Si^{5+} ion irradiation of BK7 glass containing Ag nanocrystals induces a partial redistribution of the nanocrystals into linear arrays along the ion tracks. The anisotropy causes a splitting in the optical extinction spectra, so that different surface plasmon resonance bands for longitudinal and transverse polarizations are observed. Resonance shifts as large as 1.5 eV are observed, well into the near-infrared and are in qualitative agreement with a model for near-field electromagnetic plasmon coupling.

Acknowledgements

The work presented in this Chapter was done in close collaboration with Luke Sweatlock and Harry Atwater (Caltech). Arjen Vredenberg (Utrecht University) is acknowledged for assistance with MeV ion irradiation in Utrecht, and Bart Kooi (Groningen University) is acknowledged for TEM measurements.

Highly confined electromagnetic fields in arrays of strongly coupled silver nanoparticles

Linear arrays of very small silver (Ag) nanoparticles (diameter about 10 nm, spacing 0–4 nm) were fabricated in sodalime glass using an ion irradiation technique. Optical extinction spectroscopy of the arrays reveals a large polarization-dependent splitting of the collective plasmon extinction band. Depending on preparation condition, a red-shift of the longitudinal resonance as large as 1.5 eV is observed. Simulations of the three-dimensional electromagnetic field evolution are used to determine the resonance energy of idealized nanoparticle arrays with different interparticle spacing and array length. Using these data, the experimentally observed red-shift is attributed to collective plasmon coupling in touching particles and/or in long arrays of strongly coupled particles. The simulations also indicate that for closely coupled nanoparticles (1–2 nm spacing) the electromagnetic field is concentrated in nanoscale regions (10 dB radius: 3 nm) between the particles, with a 5000-fold local field intensity enhancement. In arrays of 1 nm-spaced particles the dipolar particle interaction extends to over 10 particles, while for larger spacing the interaction length decreases. Spatial images of the local field distribution in 12-particle arrays of touching particles reveal a particle-like coupled mode with a resonance at 1.8 eV and a wire-like mode at 0.4 eV.

6.1 Introduction

In recent years, significant progress has been made towards reducing the size of optical devices. This trend towards miniaturization is driven by the increase in system functionality and reduction in power dissipation that may be achieved when highly integrated photonic networks replace today's discrete devices and standalone modules. Another important motivation is a vision of an architecture in which photonic circuits integrate seamlessly into large scale electronic systems. This requires waveguides that bridge the gap in size between conventional micron-scale integrated photonics and nanoscale electronics. Additionally, nanostructured materials often possess strong nonlinear properties that can be exploited in the development of novel active devices, since the confinement of light to small volumes can lead to nonlinear optical effects even with modest input power.

In purely dielectric materials, the optical diffraction limit places a lower bound on the transverse dimension of waveguide modes at about $\lambda_0/2n$, i.e., several hundreds of nanometers for visible light. [109, 110] Plasmonic waveguides, on the other hand, employ the localization of electromagnetic fields near metal surfaces to confine and guide light in regions much smaller than the free space wavelength, and can effectively overcome the diffraction limit.

In plasmonic systems there is generally a tradeoff between the size of the electromagnetic mode and loss in the metallic structures. With this design principle in mind there are several choices for plasmonic waveguiding technologies which may prove useful for various applications. For example, thin metal stripes support long-range surface plasmon polaritons with an attenuation length as long as millimeters, but lack subwavelength mode confinement. [12, 111–115] Another geometry is metallic nanowires, which indeed can provide lateral confinement of the mode below the optical diffraction limit. Nanowires have larger attenuation than planar films, but light transport over a distance of several microns has been demonstrated. [116] Finally, metal nanoparticles are used to achieve three-dimensional subwavelength confinement of optical-frequency electromagnetic fields in resonant “particle plasmon” modes. [1, 34, 37] Nanoparticles provide highly enhanced local fields which are promising for molecular sensors [18–20, 117] or miniature nonlinear optical elements, [23, 118–121] and arrays of these particles can act as waveguides over modest distances. [14] Indeed, linear chains of metal nanoparticles have been shown to support coherent energy propagation over a distance of hundreds of nanometers [17] with a group velocity around two-tenths the speed of light in vacuum. [122] The minimum length scales in fabricated structures were determined by the resolution of electron beam lithography, with particle diameters of $30 \times 30 \times 90$ nm, and interparticle spacings of 50 nm.

In this paper, we investigate the mode confinement and plasmon coupling in nanostructures with even smaller length scales, composed of linear chain arrays of Ag nanoparticles with diameters in the 10 nm range and interparticle spacing as small as several nanometers. This work is inspired by our recent experimental results in which linear Ag nanoparticle chain arrays with such small length scales are formed in silica glass by ion irradiation. [123] Other methods for generating very small ordered metal structures include pulsed laser irradiation [124] and biologically templated assembly. [125]

We first present experimental optical extinction spectroscopy data that show evidence for strong plasmon coupling in ion-beam synthesized Ag nanoparticle chain arrays. We compare experimental extinction data with full-field 3D electromagnetic simulations for

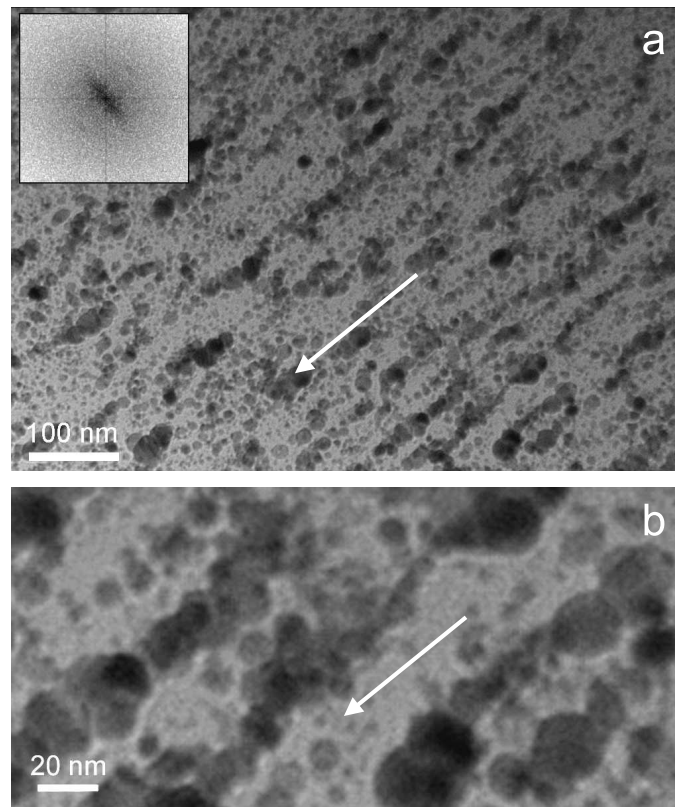


Figure 6.1: Plan-view TEM images of Ag nanoparticles in sodalime glass after 30 MeV Si^{5+} ion irradiation at two different magnifications. Nanoparticle arrays are observed along the ion beam direction (indicated by arrows). The inset in (a) shows a spatial Fourier transform image of the micrograph confirming this anisotropy. The typical particle diameter in the micrographs is 10 nm, albeit with significant size polydispersity. Touching or closely spaced particles are observed, in arrays with a length of up to about 10 particles.

arrays with various chain length and particle spacing. The simulations corroborate the experimental data and reveal large local field enhancements in arrays of strongly coupled nanoparticles.

6.2 Nanoparticle array fabrication

Linear nanoparticle arrays in glass are formed by use of high energy ion irradiation technique as follows. [123] First, ionic Ag^+ is introduced into sodalime silicate glass (BK7) by immersion in a melt of AgNO_3 , 10% by mass, in NaNO_3 at 350°C for 10 minutes. Silver displaces the constituent sodium via an ion exchange interaction, resulting in a Ag^+ content of 6 at% near the surface. Next the sample is irradiated with 1 MeV Xe^+ ions to a fluence of $1 \times 10^{16} \text{ cm}^{-2}$ at normal incidence to induce the nucleation and growth of Ag nanoparticles. The typical particle diameter is in the range of 5–15 nm, and the particles preferentially form in a $\sim 80 \text{ nm}$ thick near-surface region of the silica glass. [126] Finally, the sample is irradiated with 30 MeV Si^{5+} ions at an angle of 60° with respect to the surface normal while cryogenically cooled to 77 K.

Figure 6.1 shows a plan-view electron microscopy (TEM) image on a sample irradi-

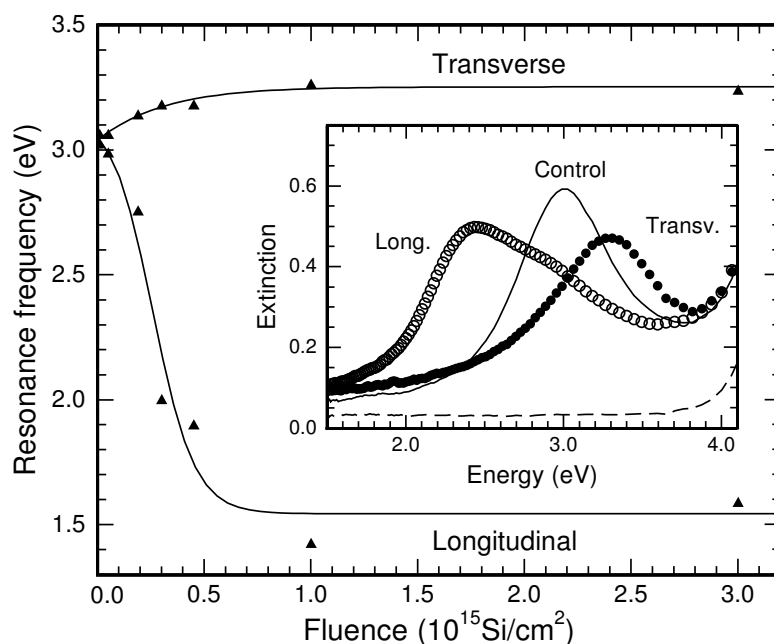


Figure 6.2: Measured optical extinction resonance peak energy for silver nanoparticle arrays in glass as a function of 30 MeV Si^{5+} fluence. The polarization of the incident light is transverse (open circles) or longitudinal (solid) to the projection of the ion beam direction into the normal plane. The inset shows typical extinction spectra for both polarizations in a sample before irradiation (“control”) and after irradiation with 2×10^{14} 30 MeV Si^{5+} cm^{-2} .

ated with 2×10^{14} Si^{5+} cm^{-2} . A polydisperse Ag particle size distribution is found, with a typical diameter of 10 nm and an upper bound of about 20 nm diameter. The majority of Ag particles appear to have been incorporated into quasi-linear chain arrays, aligned along the ion beam direction. This observation is confirmed by spatial fast Fourier transform of the image, inset in Fig. 6.1(a). The redistribution of Ag is ascribed to the effect of the thermal spike caused by silicon ions’ electronic energy loss. Figure 6.1(b) shows a magnified view of the particle arrays. While in these plan-view images it is not possible to separately identify individual arrays, as they overlap in the image, we estimate a typical array length of up to 10 particles, with particles either touching or very closely spaced.

6.3 Optical absorption spectroscopy

The inset to Fig. 6.2 shows optical extinction spectra taken under normal incidence of a sample before (“control”) and after irradiation with 30 MeV Si^{5+} ions to a fluence of 2×10^{14} cm^{-2} . Data were derived from optical transmission spectra measured using a spectroscopic ellipsometer with the incident beam perpendicular to the sample surface. The wavelength was scanned from 300 nm to 1100 nm in 5 nm steps. Before irradiation, an extinction peak is observed at an energy of 3.0 eV (free space wavelength 410 nm), corresponding to the surface plasmon dipole excitation of isolated small Ag nanoparticles in a sodalime glass matrix (refractive index $n = 1.60$). After irradiation, two distinct spectra are observed for incident light polarized either parallel or perpendicular to the ion beam

incidence direction projected into the sample surface plane. The splitting of plasmon extinction bands can be explained by “collective particle plasmon” resonances which result from electromagnetic coupling between neighboring particles in linear arrays. [42, 43] When incident light is polarized transverse to the array axis, repulsion between like surface charges on neighboring particles increases the energy required to drive a resonant oscillation and therefore results in a spectral blue-shift. Conversely, attraction between nearby unlike surface charges under longitudinally polarized incident light will result in an extinction red-shift.

The main panel of Fig. 6.2 shows the peak energy of the transverse (open circles) and longitudinal (solid) mode extinction spectra as a function of Si^{5+} ion fluence up to $3 \times 10^{15} \text{ cm}^{-2}$. The transverse branch shows a modest blue shift that saturates at 3.2 eV (390 nm) while the longitudinal absorption peak can be tuned over a wide range, from 3.0 eV (410 nm) to 1.5 eV (830 nm), into the near infrared.

The longitudinal resonance red-shift of over 1.5 eV is much greater than that previously recorded in chains of noble metal particles with relatively large diameter and spacing, for which a red-shift of 100 meV is observed. [17, 122, 127] The 1.5 eV shift is attributed to the very strong particle coupling in the present arrays. The ability to tune the resonance frequency into the near infrared is clearly valuable, as it enables applications in the important telecommunications band around $1.5 \mu\text{m}$. Also, the strong interparticle coupling implies a large enhancement of electromagnetic fields [128] in the interparticle gaps, as will be discussed further on. In the context of nanoparticle waveguides, the extraordinarily large splitting of the plasmon bands indicates large bandwidth and high group velocity for transport. [15, 129] However, very strongly coupled nanoparticles are suitable for waveguiding only over short distances, as significant spatial overlap of the mode with the metal particle leads to severe damping. [130]

6.4 Finite integration simulation procedure

The influence of geometrical parameters on the collective plasmon resonance of linear chains of Ag nanospheres is studied by three-dimensional full-field electromagnetic simulations which employ finite-element integration techniques to solve Maxwell’s equations. [131] We keep the particle size constant at 10 nm diameter, and assume that the particles are spaced evenly along a line with perfect axial symmetry. Particle spacing was varied from 0 nm (touching particles) to 4 nm. The optical constants of silver are modelled with a Drude model:

$$\epsilon(\omega) = 5.45 - 0.73 \frac{\omega_p^2}{\omega^2 - i\omega\gamma} \quad (6.1)$$

with $\omega_p = 1.72 \times 10^{16} \text{ rad s}^{-1}$ and $\gamma = 8.35 \times 10^{13} \text{ s}^{-1}$, which provides a good fit to tabulated experimental data [35] throughout the visible and infrared. The index of the surrounding glass matrix is set to $n = 1.60$. The simulation volume is a rectangular solid which extends at least 100 nm beyond the nanoparticle surfaces in all directions. The mesh is linearly graded with a 10:1 ultimate ratio, i.e., if the grid cells in the immediate vicinity of the particles are about 0.25 nm on each side, those on the outer boundary of the simulation volume are about 2.5 nm on each side. Technical limitations constrain the mesh size under these conditions to about 2 million total grid cells. In all simulations the

incident light is polarized longitudinally relative to the array. We focus on the longitudinal plasmon resonance because the optical response has a strong functional dependence on geometrical parameters, and because the extraordinary tunability of the longitudinal resonance may be of interest for a variety of applications.

A two-step process is used to find the collective particle-plasmon resonant mode and its frequency for each array. First, the simulation volume is illuminated by a propagating plane-wave with an off-resonance frequency that allows the particle chain to absorb energy. Second, the incident field is switched off and the electric field amplitude is observed in the time domain as any particle modes excited by the incident plane-wave resonantly decay or “ring down”. The data presented below are all monitored at nanoparticle centers, but in general the time response of the electric field in interparticle gaps and other points of lower symmetry are also observed to provide additional information about the mode structure. A fast Fourier transform (FFT) of these data gives the spectral response that enables the resonant frequencies to be identified. Since the absorption and ringdown are resonant phenomena, the frequency at which the peak FFT response occurs is directly comparable to the frequency of maximum extinction in an optical spectrum. Once the spectrum was outlined in this way, on-resonance excitation was used to excite individual modes to examine the corresponding spatial distribution of the field intensity. Such distributions can be used to discriminate between spectral features which correspond to the collective dipole excitation and other physical resonances or, in some cases, unphysical artifacts of the simulation or frequency domain transform which can be eliminated once identified. In some cases small “hot spots” were observed in the intensity maps, which occurred at slight faceted corners of the rendered nanospheres. By varying the grid size and geometry these were identified as artifacts of the simulation. When the grid cell linear dimensions were reduced to 0.25 nm in the immediate vicinity of the metal nanoparticles, these hot-spot artifacts had a negligible effect on the overall field distribution. This requisite fine mesh density has the indirect effect of constraining the maximum simulation size to linear arrays of about 12 nanoparticles.

Figure 6.3(a) shows peak-normalized Fourier transform amplitude spectra of particle ringdown for four-particle chains of 10 nm diameter Ag particles with interparticle spacings of 1 nm, 2 nm, and 4 nm, and for an isolated particle. We verified that the peak frequency value is robust against small changes to mesh cell density, sphere smoothness, or other minor variations in simulation procedure. In contrast, the apparent linewidth and spectral shape of the resonance were found to be somewhat dependent on arbitrary factors such as the total ringdown time and the absorption cross section of the structure at the off-resonance excitation frequency. The Fourier transform spectra often also contain several peaks with normalized amplitude less than one. Investigation of spatial energy density profiles using selective-frequency excitation revealed that low energy secondary peaks (e.g., around 2 eV in Fig. 6.3(a)) correspond to artifact modes particular to the 3D polygonal representation of the nanoparticle. The weak features observed in the spectra of Fig. 6.3 at energies slightly greater than the primary peak may correspond to real multipolar nanoparticle resonances, but further investigation via selective-frequency excitation simulation proves impossible due to the low scattering strength of the resonance and spectral proximity to the primary peak. The primary peak, however, was found to correspond to the dipole excitation in all cases. From the above analysis we conclude that the peak energy of the Fourier transform spectra is a good metric for the dipole resonance energy, and can thus be compared with experimental peak extinction energies.

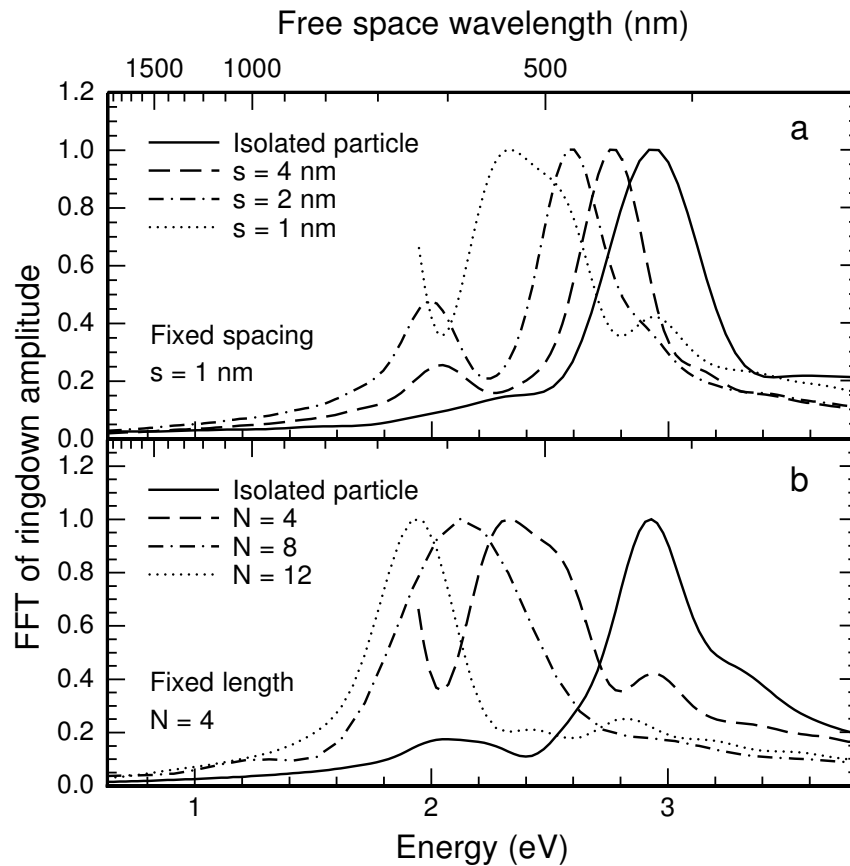


Figure 6.3: Simulated longitudinal extinction spectra for linear arrays of 10 nm diameter Ag particles in glass. (a) Array of four particles spaced by 1, 2, or 4 nm. (b) Array of 4, 8, or 12 particles with interparticle spacing fixed at one nanometer. A reference spectrum for a single Ag particle is also shown in each panel. Each spectrum is normalized to the height of the strongest extinction peak, which we identify as the collective dipole resonance.

6.5 Results and discussion

The resonance peak for isolated particles in Fig. 6.3(a) occurs at 2.93 eV (free space wavelength 424 nm), in good agreement with the experimental data (Fig. 6.2), indicating that the initially prepared Xe^+ -irradiated sample (i.e., without ordered nanoparticle arrays) consists of uncoupled nanoparticles. This is consistent with earlier work showing that under these Xe^+ irradiation conditions about 33% of the incorporated Ag^+ is agglomerated in nanoparticles with a mean diameter of 5–10 nm, while the remaining 67% remains embedded in the glass network as Ag^+ ions. The corresponding interparticle distance is about 3 particle diameters, too large for significant interparticle coupling. [105, 126]

Figure 6.3(a) also shows that a decrease in particle spacing in the 4-particle array increases the interparticle coupling, leading to increased resonance red-shift. At 1 nm spacing the simulated resonance occurs at 2.35 eV (528 nm). Figure 6.3(b) shows the effect of total chain length on simulated spectral response of Ag nanoparticle chains with the interparticle spacing fixed at 1 nm. Data are shown for arrays with a total length of 12, 8, 4, and 1 particle(s). As can be seen, increasing the chain length causes a larger

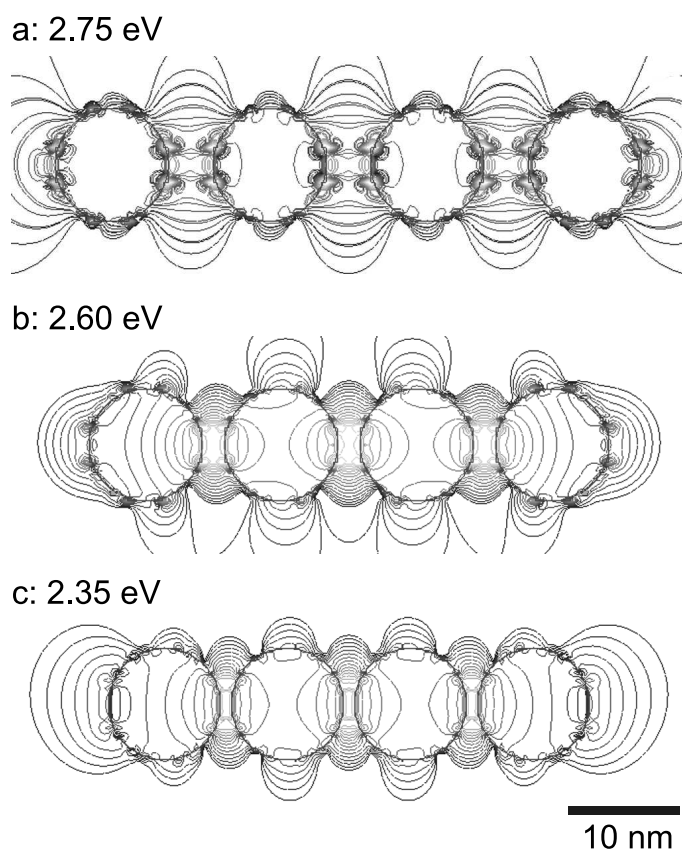


Figure 6.4: Two-dimensional spatial images of the electric field intensity in a plane through the particle centers of four Ag nanospheres with interparticle spacing of (a) 4 nm, (b) 2 nm, (c) 1 nm at resonant excitation. The background is normalized to maximum instantaneous intensity of the incident plane-wave. Each contour line represents an intensity difference by a factor of 1.8 (4 lines represent one order of magnitude).

shift towards lower frequencies, implying that the particle interaction extends beyond the first nearest-neighbor. In the twelve-particle chain the observed frequency is 1.92 eV (647 nm), a difference as large as 1.0 eV compared to the single-particle plasmon resonance. We expect that the effect of increasing chain length will saturate in chains of not more than 20 particles, based on Quinten and Kreibig's numerical calculations for Ag particles in air. [43] In less strongly coupled chains, with 2 nm or 4 nm spacing, we found that extending the overall length of the chain beyond 4 particles did not lead to a further shift in resonance frequency. This result is consistent with our earlier work, [130] in which it was reported that in chains of widely spaced and therefore relatively weakly coupled Au particles, the resonance frequency was not a strong function of array length.

Figure 6.4 shows the spatial images of the peak instantaneous electric field intensity (i.e., E^2) at steady state for arrays of four 10-nm diameter particles, excited on resonance. Data are shown for interparticle spacings of 4 nm (a), 2 nm (b), or 1 nm (c). The background level is normalized to the maximum instantaneous square amplitude of the incident plane-wave. Note that this normalization level is different than the plane-wave background at the same instant in time as the field profile snapshot, since there is a phase lag between the amplitude peaks in the driving wave and in the resonant response.

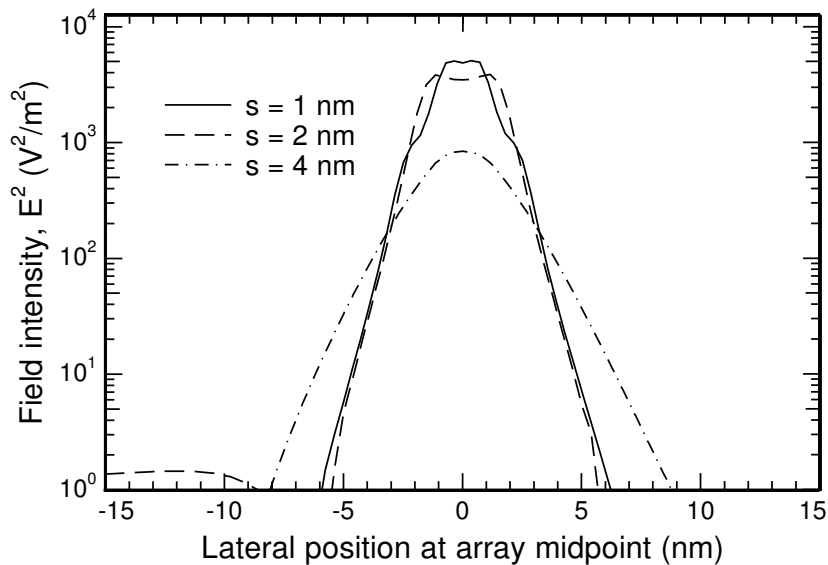


Figure 6.5: Electric field intensity on a line through the dielectric gap at the midpoint of an array of four Ag nanospheres with interparticle spacing of (a) 4 nm, (b) 2 nm, (c) 1 nm at resonant excitation. Maximum instantaneous intensity of the incident plane-wave is 1 (V/m)^2 .

Each contour line represents an intensity difference by a factor 1.8 (four lines correspond to one order of magnitude). The maximum local field is observed in the dielectric gap between the two metal particles at the midpoint of the array. The factor by which the field intensity at the array midpoint exceeds the background level is approximately 800 in the weakly coupled array, Fig. 6.4(a), and about 5000 in the more strongly coupled array (c). For comparison, the maximum field intensity enhancement near an isolated nanoparticle driven resonantly is typically 30. The giant 5000-fold intensity enhancement is consistent with previous reports of 10^6 – 10^8 -fold enhancement of the effective Raman scattering cross-section near metallic nanostructures, given the fact that Raman scattering is quadratic in field intensity. [18, 19]

Figure 6.5 shows the field intensity along a line normal to the particle axis through the interparticle gap at the midpoint of a 4-particle array. The field confinement is most pronounced for the array with the smallest spacings, 1 nm and 2 nm, where the lateral distance (from the array axis) at which the field diminishes by 10 dB is 3 nm; it vanishes by 30 dB in less than 6 nm. Given that the resonant excitation wavelength for this mode in bulk glass is 330 nm, this clearly demonstrates the giant field enhancement and localization in these closely-spaced nanoparticle arrays. Figure 6.5 also shows that for 4 nm spacing the field is less concentrated, with a 10 dB decay distance of 5.5 nm and peak field intensity nearly 10-fold lower than for the 1-nm spaced array. This demonstrates that true nanoscale engineering is required to advantage of these high field concentration effects. Indeed, the ion-irradiation-induced nanoparticles arrays in Fig. 6.1 are an example of that.

In TEM images such as Fig. 6.1 we observe a strong possibility that in some arrays the interparticle separation has been reduced to the point that the nanoparticles just touch their neighbors. We refer to these arrays as having “0 nm interparticle spacing”. In simulations the neighboring spheres are defined to overlap each other by about 0.25 nm (one grid cell

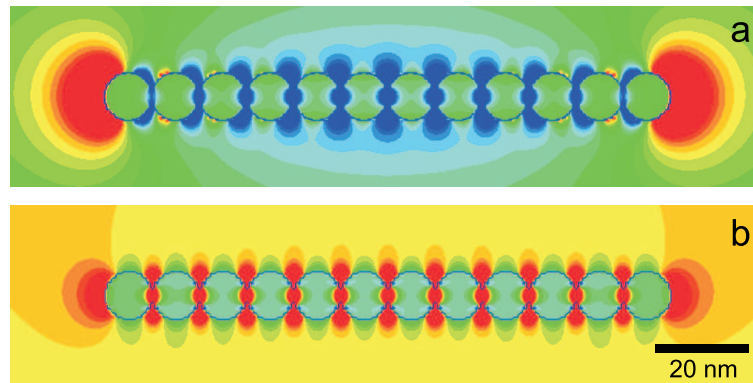


Figure 6.6: [Color] Distribution of the longitudinal component of the electric field (E_x) in the vicinity of an array of twelve Ag particles with 10 nm diameter, illustrating two distinct modes. (a) an antenna-like mode resembling that of a single elongated wire is excited resonantly at 0.35 eV; (b) a coupled particle-like mode resembling that of a chain of independent particles is excited resonantly at 1.65 eV. The slight axial asymmetry of the field distribution is caused by superposition of the resonant mode with the exciting plane-wave.

depth) and therefore share a circular boundary surface with a radius of about 1 nm. In this case, two distinct modes are found in the spectrum. For an array length of 12 particles these occurred at 0.35 eV (free space wavelength 3500 nm) and 1.65 eV (750 nm). As described in section 6.5, we selectively excite and study the spatial distribution of the electric field for the two cases. In this case, however, the additional low energy peak is not an edge or corner artifact but has real physical significance. This is demonstrated in Fig. 6.6, which shows the longitudinal component (E_x) of the electric field in a system which consists of a linear array of 12 touching Ag spheres excited at the two resonance frequencies. Areas colored red have positive field amplitude, while areas colored blue have negative field amplitude. In a snapshot of the chain driven by a longitudinally polarized plane-wave at 0.35 eV [Fig. 6.6(a)], regions of positive E_x are observed at either end, with negative E_x throughout the body of the array. This electric field pattern indicates that positive surface charge is concentrated on the rightmost particle, and negative charge on the leftmost particle. The mode is typical of a single wire antenna, and requires surface charge to flow from particle to particle along the entire length of the array. Alternatively, when the same structure is driven at 1.65 eV [Fig. 6.6(b)] the coupled-dipole resonance is selectively excited. The field diagram alternates from positive in each dielectric gap to negative inside each particle. This indicates an alternating surface charge distribution in which each individual particle is polarized but electrically neutral. Thus, in the touching-particle configuration, the system can support two kinds of longitudinal resonance: the particles can still act as individual coupled dipoles, or instead, as a single continuous wire antenna.

Although particle- and wire-like modes of touching particle chains have strongly shifted peak resonance frequencies, we found that they do not in general exhibit an extremely high degree of local field amplification. The lack of a dielectric gap means that the interparticle interaction is only weakly capacitive in nature, and therefore only a small magnitude of opposing surface charge builds up on neighboring particles. However, a contrary influence also comes into play. The sharp “crevice” formed between two inter-

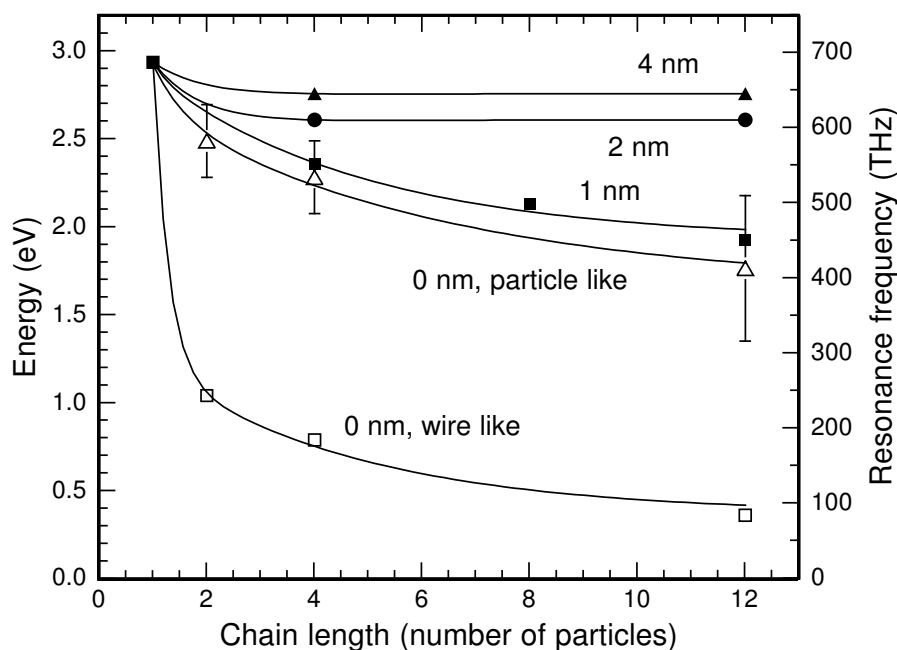


Figure 6.7: Simulated longitudinal collective resonance frequency for linear arrays of various overall length, ranging from one to twelve Ag particles each 10 nm in diameter. Series represent interparticle spacings from zero to four nanometers. In the case of zero nanometer spacing, frequencies of both coupled-nanoparticle-like and wire-like modes are plotted.

secting spheres may contribute to shape induced enhancement to the local fields. For the specific geometric configuration and material properties input to our simulation, we found the former effect to dominate. Various aspects of coupled modes in nanoparticle dimers, including the touching-particle case, are discussed in Refs. [132–134].

Figure 6.7 shows a compilation of longitudinal resonance energies for linear arrays of 10 nm diameter Ag particles, plotted as a function of chain length. The data series represent interparticle spacings of 4, 2, 1, or 0 nm. In the case of zero nanometer spacing, the energies of coupled-nanoparticle-like and wire-like modes are plotted separately (indicated “particle like” and “wire like”). The particle-like resonances are broad, as indicated by error bars on that series. The Figure shows that for 12-particle array length the resonance of the most strongly coupled arrays (0 or 1 nm spacing) shifts by about 1.1 eV, to a peak resonance energy of around 1.82 eV. More weakly coupled chains saturate at peak energies above 2.50 eV.

We now compare these data with the experimental particle distributions and resonance energy measurements in Figs. 6.1 and 6.2. Although the nanoparticle distributions are quite inhomogeneous, indeed, touching and nearly-touching particles are observed in the TEM, that according to our simulations lead to large plasmon shifts. The decrease in plasmon energy with increasing fluence [Fig. 6.2] can be attributed to either (or both) a gradual growth in particle array length or a decrease in interparticle spacing. The experimentally observed peak resonance for high fluence irradiation in Fig. 6.2 is 1.5 eV. The resulting resonance energy is thus lower than the lowest coupled-particle mode energy calculated in Fig. 6.7 (1.8 eV). This may indicate that long chains ($N > 12$ particles)

form at large fluence. Alternatively, wire-like modes in small chains could be dominating as interparticle spacing approaches zero. Further investigation of the relative interaction cross-section for the wire and particle modes would be necessary to support this hypothesis.

For applications of field enhancements at the important telecommunication wavelength of $1.5\ \mu\text{m}$ (0.8 eV), very strongly coupled arrays of nanoparticles are required. Comparing our data with those our results from arrays of larger particles, [122] and with previous results in the literature, [43] it appears that it is the combination of particle center-to-center spacing and diameter, rather than interparticle spacing alone, that is a key parameter determining coupling strength. Finally, we note possible applications of the wire-like mode in the THz frequency domain, in particular for very long array lengths.

6.6 Conclusions

Linear arrays of very small Ag particles in glass, made using ion irradiation, show a strong anisotropy in optical extinction spectra, which is attributed to strong coupling between the particle plasmons. Full-field simulations of the electromagnetic field distribution on arrays of closely spaced Ag nanoparticle arrays show that coupling between the plasmonic particle modes leads to a reduction in the longitudinal resonance energy. In weakly coupled arrays, in which 10 nm particles are separated by 2 or 4 nm interparticle gaps, the resonance shift is less than 0.4 eV. For the “strongly coupled” case of 1 nm spacing, or touching particles, a shift larger than 1.0 eV is observed. In those arrays the longitudinal plasmon resonance energy decreases with the total chain length up to at least 10 particles. In particle arrays with 1 nm spacing, the simulations indicate a giant 5000-fold enhancement in field intensity between the particles. The resonant electric field is concentrated in extremely small regions with a radial dimension of 3 nm (at 10 dB point). By comparing the simulated data with the experimental optical data it is concluded that plasmon coupling behavior in the experimental samples is dominated by short arrays of touching particles, and/or long arrays of strongly coupled particles. Due to the great utility of wavelength tunability and local field enhancement for applications such as nonlinear optics and sensing of small volumes, nano-sized ordered or quasi-ordered ensembles of very closely spaced metal particles serve as an ideal platform for active device regions in integrated plasmonic networks. Innovative nanoscale engineering and fabrication (as the ion irradiation technique used here) are required to synthesize particle arrays with these interesting properties.

Acknowledgements

This work is performed in close collaboration with Luke Sweatlock and Harry Atwater (Caltech). Bart Kooi (University of Groningen) is acknowledged for TEM, and Arjen Vredenberg (Utrecht University) for assistance with MeV ion irradiation. Kobus Kuipers (FOM-AMOLF) is gratefully acknowledged for stimulating discussions and advice. David Sheets (Caltech) is acknowledged for scripting simulation macro files.

Part III

Metal shells

Ion beam deformation of metal shell colloids

Spherical colloids composed of a silica core (diameter: 300–500 nm) and gold or silver shell (20–60 nm thick) were irradiated with 6 MeV Au³⁺ and 30 MeV Cu⁵⁺ ions. The irradiation changes the shape into oblate ellipsoidal, with the anisotropy determined by the ion fluence. A major-to-minor diameter ratio of 1.5 is achieved after irradiation with 30 MeV Cu⁵⁺ ions to a fluence of $5 \times 10^{14} \text{ cm}^{-2}$. The observed shape change is the result of an ion-induced anisotropic deformation process in the amorphous silica. At constant fluence, the net observed anisotropy decreases with increasing Au-shell thickness, which implies that the Au-shell imposes a mechanical constraint on the deformation of the silica core. The addition of an outer silica shell to the silica-core/Au-shell colloids enhances the deformation. These anisotropic metallo-dielectric colloids can be used as novel building blocks in photonic materials.

7.1 Introduction

Metallo-dielectric colloids, consisting of a metal and a dielectric material in a core/shell geometry, form a new class of interesting building blocks for photonic materials. Coherent oscillations of the conduction electrons in the metal give rise to strong plasmon resonances. The plasmon frequency depends on the size, shape, composition and the optical constants of the surrounding medium. For metal shells, the optical response also depends on the relative ratio of the core radius and the shell thickness. By variation of this core-to-shell ratio, the plasmon frequency can be shifted from the visible into the infrared (2.3 eV to 0.1 eV). [34, 37, 135, 136]

While many papers have been published on spherical core/shell systems, *anisotropic* composite colloids give an additional parameter to tailor the optical response. Control over the shape of the anisotropic composite particles is of great importance, for example in studies of electro-magnetic field enhancements near highly curved metal surfaces. One approach to synthesize monodisperse anisotropic core/shell particles with a metal shell is seeded growth, as was shown recently by Limmer *et al.* [137] for silica and titania nanorods, and by Wang *et al.* for hematite spindles. [138] Another approach, as will be shown in this paper, is to use ion irradiation to change the shape of initially spherical colloids to oblate ellipsoidal.

Over the last few years, ion beam-induced plastic deformation of colloidal particles was addressed in several papers. [92, 139, 140] It was shown that colloids expand biaxially perpendicular to the ion beam direction and contract uniaxially along the ion beam direction, while their volume remains constant. The aspect ratio of the ellipsoids can be accurately tuned by varying the ion fluence. This plastic deformation is known to occur with amorphous materials, with the deformation rate dependent on the electronic energy loss of the penetrating ions. Ion irradiation is a directional technology, and the ellipsoidally shaped colloids are thus all aligned along the ion beam direction. This enables optical characterization of well-oriented particles by averaging over large ensembles. The deformed particles can also be removed from the substrate and brought back in solution by sonication. [139] Depending on the irradiation conditions and the desired aspect ratio, the particle yield of the ion beam deformation technique is typically 10^8 - 10^9 particles (0.5–5 mg) per hour, sufficient for fundamental studies.

Recently, ion irradiation was applied to metallo-dielectric colloids comprising a Au core and a silica shell. [101] It was found that the irradiation turned the spherical silica shells into oblate ellipsoids and the spherical metal cores into prolate ellipsoids. Gold cores without a silica shell remained spherical under ion irradiation.

In this Chapter we study colloids of the reverse core/shell geometry, i.e., colloids consisting of a silica core (diameter: 300–500 nm) and a shell of gold or silver (20–60 nm thick), and investigate their plastic deformation upon ion irradiation. We find that the shape of the spherical colloids changes into oblate ellipsoidal, with the final degree of anisotropy determined by the ion fluence. The observed deformation is attributed to the ion-induced anisotropic deformation process in the amorphous silica. Comparing samples with different Au-shell thicknesses at constant fluence, we find that the net observed anisotropy decreases with increasing Au-shell thickness, indicating that the Au-shell imposes a mechanical constraint on the deformation of the silica core.

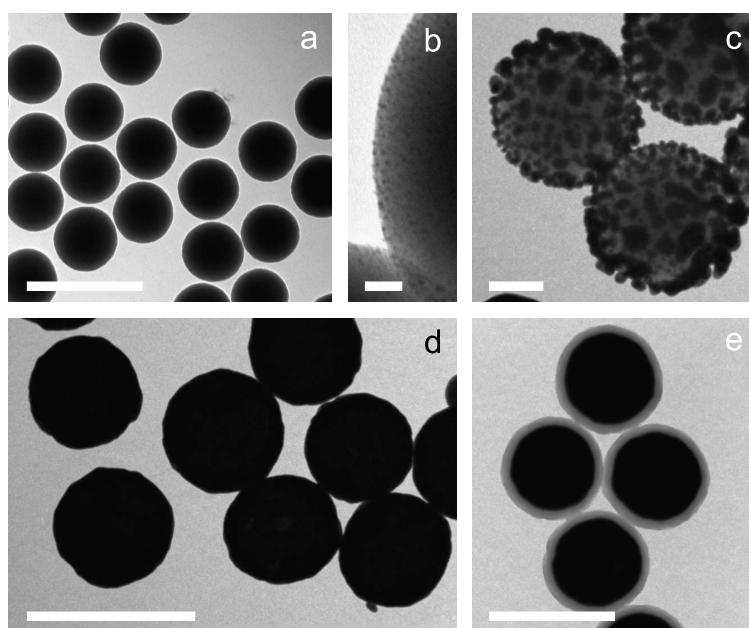


Figure 7.1: Transmission electron microscopy images illustrate different steps in the synthesis of metal shells. (a) monodisperse silica cores of about 310 nm in diameter, (b) 1–2 nm Au colloids on these silica cores, (c) intermediate stage during growth, (d) completed Au-shells, (e) Au-shell colloids coated with a silica layer of about 40 nm. The scale bars are 500 nm (a, d, e), 50 nm (b) and 100 nm (c).

7.2 Experimental

Silica-core/Au-shell colloids were synthesized using the method described in Ref. [99]. In brief, monodisperse silica colloids with diameters in the range between 300 nm and 500 nm were synthesized using the Stöber method [85] and functionalized with 3-aminopropyl-trimethoxysilane to enable the attachment of small gold nanoclusters (1–2 nm in diameter). Figure 7.1(a) shows a TEM image of silica colloids of 310 nm in diameter. The Au-shell was then grown via reduction of an aged solution of chloroauric acid by addition of a hydroxylamine hydrochloride solution [Figs. 7.1(b-d)], with the small gold particles on the silica cores acting as the seed crystals in the reduction reaction. The thickness of the Au-shell was controlled by the ratio of the amount of precursor particles and the volume of the gold salt solution. Thicker Au-shells were grown by seeded growth. An additional outer silica shell was grown via functionalization of the silica-core/Au-shell particles by polyvinylpyrrolidone, [88] after which the colloids were transferred into ethanol to enable the growth of the outer silica shell via a Stöber reaction [Fig. 7.1(e)]. In a similar way, Ag-shells were grown on Au-decorated silica beads by reduction of silver nitrate with formaldehyde in the presence of ammonia and dodecylbenzyl sulfonic acid. [141]

After synthesis, a droplet of the colloidal suspension was dried on a Si(100) substrate under nitrogen flow, so that the typical surface coverage was well below a monolayer.

The ion irradiations were performed using a 6 MV Van de Graaff accelerator. The ion beam was electrostatically scanned across a $1.0 \times 1.0 \text{ cm}^2$ area. Ion beams of 30 MeV Cu^{5+} , 6 MeV Au^{3+} were used either at normal incidence or at an angle of 45° with respect to the substrate normal. The ion beam energy flux was in the range of $0.04\text{--}0.9 \text{ W cm}^{-2}$

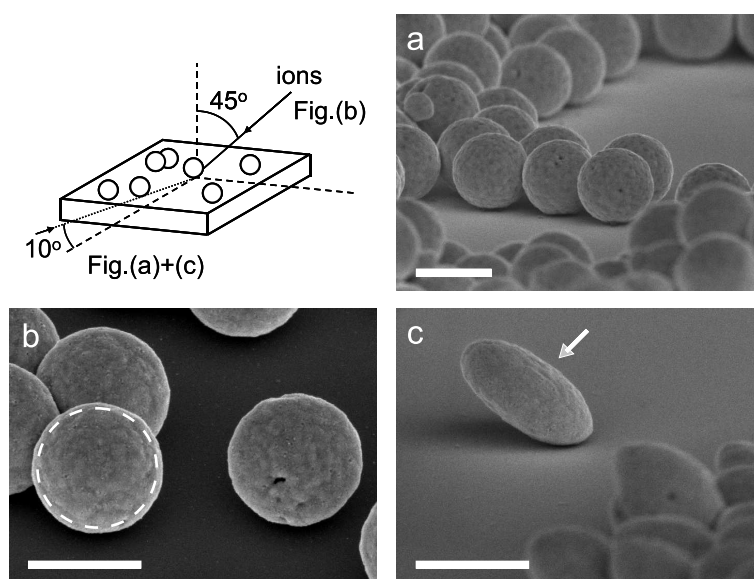


Figure 7.2: SEM images of silica-core/Au-shell colloids on a silicon substrate: (a) unirradiated, (b, c) irradiated with 30 MeV Cu^{5+} ions at 45° at 77 K to a fluence of $5 \times 10^{14} \text{ cm}^{-2}$, viewing angle parallel (b) or almost perpendicular (c) to the ion beam direction. The upper left schematic shows the ion beam direction and the SEM viewing angles. The scale bars are 500 nm.

for all irradiations. During the irradiation, the samples were clamped to a liquid-nitrogen-cooled Cu substrate holder. Scanning electron microscopy (SEM) at 5–30 keV was used to determine the particles' size and shape before and after ion irradiation.

7.3 Results and discussion

Figure 7.2(a) shows a side-view SEM image (10° -tilt angle) of Au-shell colloids on a Si substrate before ion irradiation. The angle of irradiation and the view angles are indicated in the schematic inset. The total diameter of the colloids is 530 ± 18 nm. From this, by assuming that the polydispersities of the core and the shell colloids are independent, [99] the Au-shell is calculated to be (46 ± 11) nm thick. Next, the sample was irradiated with 30 MeV Cu^{5+} ions to a fluence of 5×10^{14} ions cm^{-2} at 45° . Figure 7.2(b) shows irradiated colloids, imaged along the ion beam direction. The dashed circle indicates the circumference of the unirradiated particles. It is clear that the colloids have expanded in the direction perpendicular to the ion beam. In Fig. 7.2(c), the colloids are imaged almost perpendicular to the ion beam direction, at a side-view tilt angle of 10° with respect to the substrate surface. Clearly, the colloids have contracted along the ion beam. The silica core remains uniformly covered with Au after deformation. These irradiated colloids have an average size aspect ratio (major over minor diameter) of 1.47 ± 0.16 .

The ion irradiation-induced plastic deformation of amorphous materials can be described by a visco-elastic thermal spike model. [56, 57] An energetic ion that penetrates a solid heats a small cylindrical region along the ion track in less than 10^{-12} s. The rapid thermal expansion of this thermal spike causes deviatoric (shear) stresses that relax by Newtonian viscous flow at ion track temperatures above the flow temperature. The

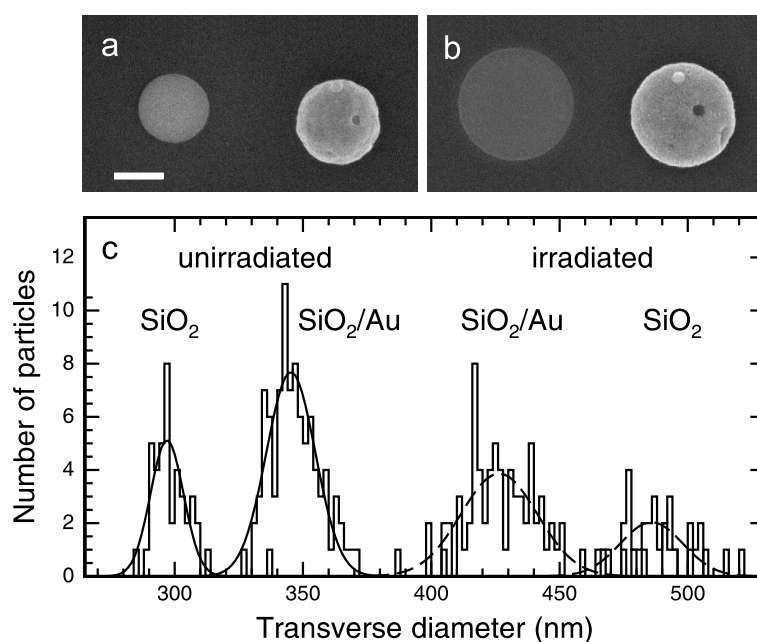


Figure 7.3: Top view SEM images of the same colloids (a silica core colloid and a silica-core/Au-shell colloid) before (a) and after (b) irradiation with 30 MeV Cu⁵⁺ ions at normal incidence to a fluence of $1 \times 10^{15} \text{ cm}^{-2}$. The scale bar is 200 nm. (c) Histograms of the transverse diameter of Au-shell colloids and silica reference colloids before (lines) and after irradiation (dashed lines).

resulting viscous strains freeze in for large track cooling rates, resulting in a net local anisotropic deformation of the material. The macroscopic deformation then is the result of many ion impacts in each colloid. For the fluence and colloids of Fig. 7.2, a typical number of 10^6 ions impacted on each colloid. In contrast to amorphous materials such as silica, crystalline materials like metals do not show anisotropic deformation under ion irradiation. [49, 54] This effect is attributed to epitaxial recrystallization at the solid-liquid interface of the molten cylindrical thermal spike region. In addition, track temperatures in crystalline metals are not likely to exceed the melting temperature as a result of rapid redistribution of the deposited energy in the electronic subsystem. [94, 142] For these metal shell colloids, however, melting has been observed at a temperature of 300°C, well below the bulk melting temperature. [143] No melting have been observed during the ion irradiation experiments, indicating that the temperature in the metal shell did not exceed 300°C. Given the deformation observed in Fig. 7.2, the deforming silica core must thus impose a deformation on the Au-shell that would otherwise not deform under irradiation. We attribute the conformal shape transformation of the metal to radiation-induced viscous flow that leads to an effective softening of the metal under irradiation. Indeed, stresses in metals such as Al and W are known to relax by ion irradiation-induced Newtonian viscous flow. [144, 145] This is further supported by the observation that the metal shell surface appears somewhat smoothed after the irradiation [see Fig. 7.2(c) and Fig. 7.3(b)]. Since plasmonic properties of these core/shell colloids are sensitive to surface roughness, this is an interesting additional effect of the ion irradiation.

To directly compare the deformation of core/shell colloids with that of pure silica colloids (i.e., without Au-shell), droplets of both colloidal suspensions were dried on a silicon substrate. The average radii of the silica colloids and silica-core/Au-shell colloids

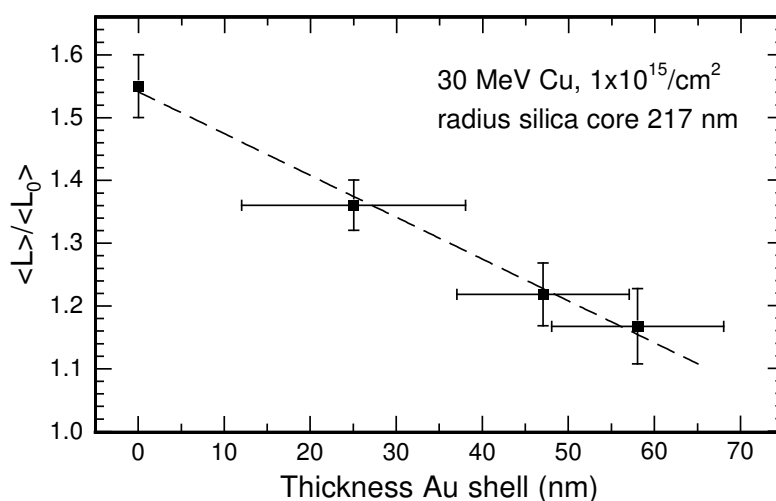


Figure 7.4: Averaged normalized transverse diameter versus Au-shell thickness for silica-core/Au-shell colloids irradiated with 30 MeV Cu^{5+} to a fluence of $1 \times 10^{15} \text{ cm}^{-2}$. The observed deformation is reduced upon an increase in Au-shell thickness. The dashed line is a guide to the eye.

were (149 ± 4) nm and (173 ± 6) nm, respectively. The average thickness of the Au-shell thus amounts to (24 ± 7) nm. Fig. 7.3(a) shows a top-view SEM image of a silica colloid (left) and a silica-core/Au-shell colloid (right). After irradiation with 30 MeV Cu^{5+} ions to a fluence of $1 \times 10^{15} \text{ ions cm}^{-2}$ at normal incidence the same two colloids were imaged again, as shown in Fig. 7.3(b). Note that the nanoscale features (e.g., the hole) of the Au-shell are preserved. As expected, the transverse dimensions of both types of colloids have increased. However, the transverse diameter of the silica colloid is now larger than that of the silica-core/Au-shell colloid. Figure 7.3(c) shows the distributions of the transverse diameter of the colloids before and after the ion irradiation. Gaussian fits through these data show that the average transverse diameter of the silica colloids increased from (297 ± 6) nm to (486 ± 12) nm, while the average transverse diameter of Au-shell colloids increased from (345 ± 10) nm to (426 ± 15) nm. From this, we conclude that the presence of the Au-shell reduces the ion beam-induced anisotropic deformation of the silica core.

We have also performed experiments on the deformation of silica cores covered with a silver shell. Very similar deformation effects are observed as for the Au-shell, with the Ag flowing conform with the silica core's shape, leading to the formation of an anisotropic Ag-shell.

To examine the effect of the Au-shell thickness on the deformation process in more detail, silica-core/Au-shell colloids were synthesized using identical silica cores of radius (217 ± 10) nm and varying Au-shell thickness. After the synthesis, the thickness of the Au-shell was found to be (25 ± 13) nm, (47 ± 10) nm, and (58 ± 10) nm. A 30 MeV Cu^{5+} beam at an angle of 45° was used to deform the colloids. The fluence was $1 \times 10^{15} \text{ ions cm}^{-2}$. In Fig. 7.4 the average transverse diameter $\langle L \rangle$ is plotted versus the thickness of the Au-shell. The data were normalized to the average diameter $\langle L_0 \rangle$ before irradiation. We observe that the anisotropic deformation decreases upon an increase of the thickness of the Au-shell.

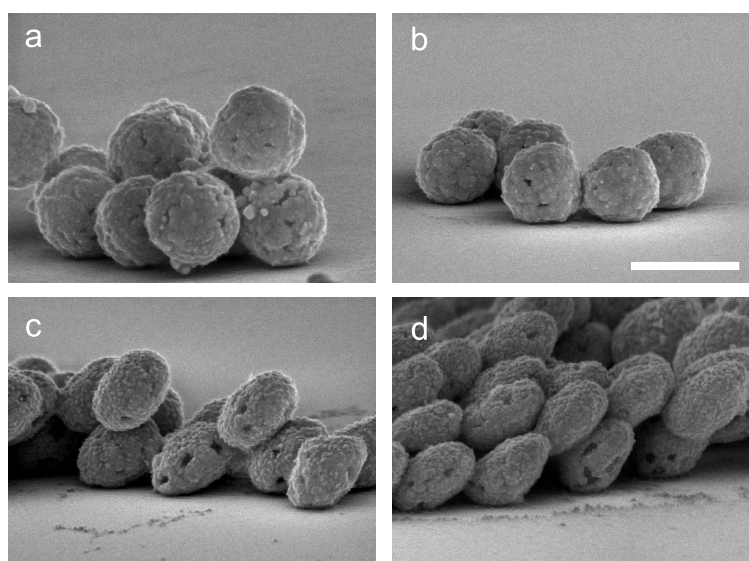


Figure 7.5: SEM images of silica-core/Ag-shell colloids on Si before (a) and after 6 MeV Au^{3+} irradiation at fluences of $1.0 \times 10^{14} \text{ cm}^{-2}$ (b), $2.2 \times 10^{14} \text{ cm}^{-2}$ (c) and $4.5 \times 10^{14} \text{ cm}^{-2}$ (d). All images are taken at the same magnification and at a side view angle of 10° . The anisotropic deformation of the partly etched silica core becomes visible only at higher fluences. Scale bar is 500 nm.

It is by now quite well established that the electronic stopping S_e of the energetic ions is responsible for the ion beam-induced plastic deformation of amorphous materials like silica. [53, 146] The decrease in S_e in the silica due to the energy loss in the Au-shell is only 1% for the dimensions under consideration. [47] The reduced deformation of the silica core must thus be due to the mechanical constraint of the metal shell. Indeed, for very large shell thicknesses, no deformation of the core is expected. Our data in Fig. 7.4 predict this to occur for Au-shells on silica colloids (with a radius of 217 nm) thicker than about 100 nm.

It is interesting to compare our data with those by Garrido *et al.*, who studied multilayered systems, composed of a crystalline layer of Au or W sandwiched between two layers of amorphous Ni_3B . [147] Upon ion irradiation with 500 MeV I ions, they observed that the crystalline layer was subjected to a tensile stress due to the expanding adjacent amorphous layer. In this case, the metal layer then counteracts the expansion of the amorphous layers by means of macroscopic elastic forces. It was found that the net deformation decreased with thickness of the crystalline layer, similar to our experiments.

Another proof that the anisotropic deformation of metal shell colloids is driven by the ion-induced deformation of the silica core, is given by irradiation of metal shell colloids with incomplete cores. Ag-shells were grown on silica cores with a diameter of 400 nm. [141] After the synthesis, the silica cores were uniformly etched by a so far unknown process to about a diameter of 300 nm. The size of the etched silica cores was determined by heating the Ag-shells for 1 hour at 350°C to melt the 20 nm thick silver shells. Non-etched silica cores measured 391 ± 10 nm in diameter after the anneal.

The Ag-shell colloids with etched cores were irradiated with 6 MeV Au^{3+} ions at an angle of 45° to fluences in the range of 1.0 – $6.5 \times 10^{14} \text{ cm}^{-2}$. SEM images, taken at a side view angle of 10° before and after irradiation, are shown in Figure 7.5. At a low fluence,

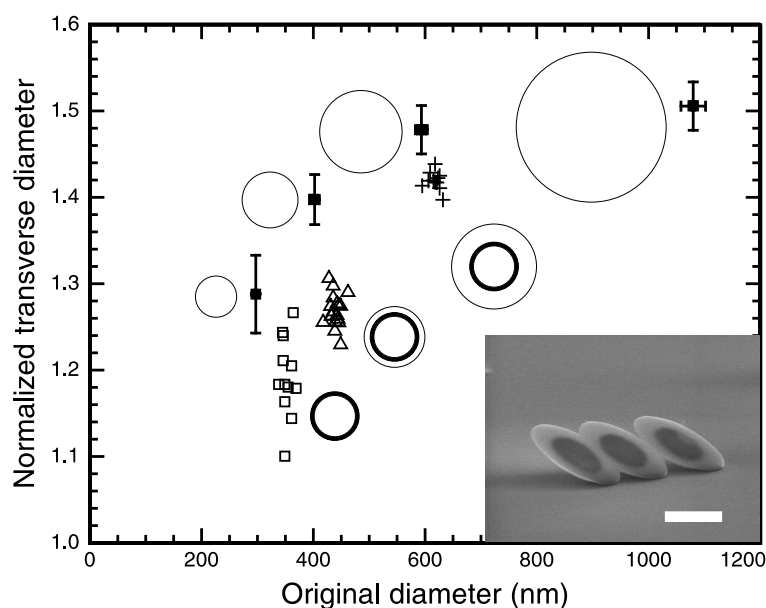


Figure 7.6: Normalized transverse diameter versus the original diameter of the silica and the silica-core/Au-shell/silica-shell colloids after irradiation with $6.5 \times 10^{14} \text{ Au}^{3+} \text{ cm}^{-2}$ at an angle of 45° : silica (closed squares), silica-core/Au-shell (open squares) and silica-core/Au-shell colloids with an outer silica shell (open triangles/crosses). The core/shell/shell structure of the colloids is also indicated schematically. A side-view SEM image of irradiated Au-shell colloids with a thick silica shell is shown as inset. The scale bar is 500 nm.

Fig. 7.5(b), the overall size of the colloids has shrunk, which is ascribed to flow of the metal shell onto the shrunk silica cores. At higher fluences, the anisotropic deformation induced in the silica core becomes prominent as can be observed in Fig. 7.5(c) and (d).

Next, we investigated the plastic deformation of silica colloids covered with a Au-shell and an additional silica shell. This outer silica shell is useful in preventing aggregation of the metal shell colloids during growth and drying of colloidal crystals (by reduction of the van der Waals forces). It could also serve as a host for optical emitters such as dyes, rare earth ions or quantum dots, whose emission can be modified by the local field enhancements. The thickness of this outer silica shell was either $(44 \pm 7) \text{ nm}$ or $(133 \pm 7) \text{ nm}$. The Au-shell colloids consisted of a silica core with a radius of $(149 \pm 4) \text{ nm}$ covered with a $(24 \pm 7) \text{ nm}$ thick Au-shell. Silica colloids of different sizes, made using seeded Stöber growth, were used as a reference for the deformation experiments. The colloids were irradiated with 6 MeV Au^{3+} ions to a fluence of $6.5 \times 10^{14} \text{ ions cm}^{-2}$ at an angle of 45° at 77 K. The resulting deformation of the colloids versus the colloid diameter before irradiation is shown in Fig. 7.6. The core/shell/shell structure of the colloids is schematically depicted as well.

Three conclusions can be drawn from this graph. Firstly, for pure silica colloids (closed squares) the ion beam-induced anisotropic deformation rate decreases with decreasing diameter. As will be shown in a separate paper, this effect is due to capillary stresses resulting from the surface tension. [148] Secondly, as was already shown above, Au-shell colloids (open squares) show a smaller relative deformation than the corresponding silica core colloids (closed squares, diameter 300 nm). The spread in the data reflects the polydispersity of the shell thickness. Thirdly, Au-shell colloids with an additional

silica shell (open triangles, crosses) deform less than pure silica colloids of equal size, but for increasing silica shell thickness, the overall deformation approaches that of pure silica colloids. The inset in Fig. 7.6 shows a side-view SEM image of irradiated Au-shell colloids with thick silica shells. In the image, taken using a 30 keV electron beam, the embedded (deformed) Au-shell appears as a clear contrast. This is a result of the backscattered electrons of the substrate and the Au-shell, that generate additional secondary electrons, which then are both detected. Due to the sensitivity of the backscattered electrons to the tilt angle of the sample, the inverse contrast can be observed as well (for example at normal incidence).

7.4 Conclusions

In conclusion, we have shown that MeV ion irradiation can be used to turn spherical colloids with a silica core and a metal shell into oblate ellipsoids. A typical major-to-minor aspect ratio of 1.5 is achieved after irradiation with 30 MeV Cu^{5+} to a fluence of $5 \times 10^{14} \text{ cm}^{-2}$. The anisotropic plastic deformation is attributed to the ion-induced deformation of the silica core, counteracted by the mechanical constraint of the metal shell. At constant fluence, an increase of the metal shell thickness reduces the deformation, while the addition of an extra silica shell results in deformation rates that approach the deformation rates of silica. Due to the high level of control over the aspect ratio and to the well-defined orientation inherent to the method, these anisotropic metallo-dielectric colloids may be ideal building blocks in photonic applications.

Acknowledgements

The work presented in this Chapter was done in close collaboration with Christina Graf (synthesis) and Teun van Dillen (initial irradiation experiments). Arjen Vredenberg is acknowledged for the help with irradiations in Utrecht.

Optical properties of spherical and anisotropic gold shell colloids

Core/shell colloids consisting of a metal shell and a dielectric core are known for their special optical properties. The surface plasmon resonance of these metal shell particles strongly depends on the ratio between the relative dimensions of the core and shell. In addition, size and shape play an important role: larger particles show excitation of higher order modes, and anisotropic particles show split transverse and longitudinal modes. In this Chapter, we investigate the optical properties of spherical and oblate ellipsoidal Au-shell colloids. Experimental data are in good agreement with T-matrix calculations on single particles.

8.1 Introduction

The unusual optical properties of metal structures with dimensions smaller than or comparable to the wavelength of light are topic of intensive research. The key concept in this field is the surface plasmon resonance, a collective resonant oscillation of the conduction electrons in the metal confined to the interface between the metal and a dielectric.

For small metal particles, the surface plasmon is confined to the particle and is therefore also called a localized surface plasmon. The resonance frequency strongly depends on the shape of the particle, but also on the size and the dielectric constant of the surrounding medium. [34, 37] Under illumination at resonance the electromagnetic fields at the surface can be enhanced by several orders of magnitude. Because of the enhanced field intensities and the tunability of the resonances, numerous applications are possible. Examples include surface enhanced Raman scattering (SERS), optical waveguiding and biochemical sensing. [149]

Structures composed of a metal shell on a dielectric core exhibit a larger tunability of the surface plasmon frequency than the opposite geometry (metal-core/dielectric-shell), since the former resonance is very sensitive to the thickness of the metal shell. [44, 136] For decreasing metal shell thickness, a red-shift of the plasmon resonance is observed. This is attributed to the electromagnetic coupling between the surface plasmon modes on the inner and outer boundary of the metal shell, resulting in two new eigenmodes. [45, 46] This process is similar to the hybridization of atomic orbitals that creates molecular orbitals. The red-shifted symmetric mode (with like charges on the inner and outer boundary of the shell) has the largest dipole moment and couples most strongly with the incoming field, whereas the overall dipole moment of the blue-shifted anti-symmetric mode (corresponding to opposite charges on the inner and outer boundary of the shell) is negligible due to the antiparallel alignment of the dipoles. [46]

Anisotropic particles show a split in plasmon resonance into a transverse and longitudinal mode. In literature, only a few articles have been published on anisotropic core/shell particles, probably due to the difficulty to control the precise size and shape of the particles. Limmer *et al.* [137] and Wang *et al.* [138] have reported on the fabrication and optical characterization of rod-like dielectric particles with a metal coating. Wang reported on a red-shift of the longitudinal plasmon resonance by about 200 nm from 1080 to 1270 nm as the shell thickness on 340 nm long hematite spindles is reduced from 28 to 10 nm. However, hematite absorbs light in the visible and hence limits the use of these particles in optical applications. Wang *et al.* also show calculations with local field enhancements of 7000 at resonant excitation, similar in magnitude to results reported on closely-spaced metallic nanoparticles. [33, 108, 150]

Recently, we have shown that oblate ellipsoidal Au-shell particles with a continuously and precisely variable shape can be fabricated using MeV ion irradiation. [151] The highly energetic ions induce an elongation perpendicular to the ion beam and a shrinkage parallel to the ion beam, and the degree of anisotropy can be tuned by the ion fluence. With this new technique, in detail described in Chapter 7, it is possible to make large substrates with relatively monodisperse oblate ellipsoidal particles, with the short axis aligned in the direction of the ion beam. This enables angle-dependent optical extinction measurements on large numbers of same-oriented anisotropic particles, providing information on the shape- and orientation-dependent optical properties of the particles with simple optical techniques.

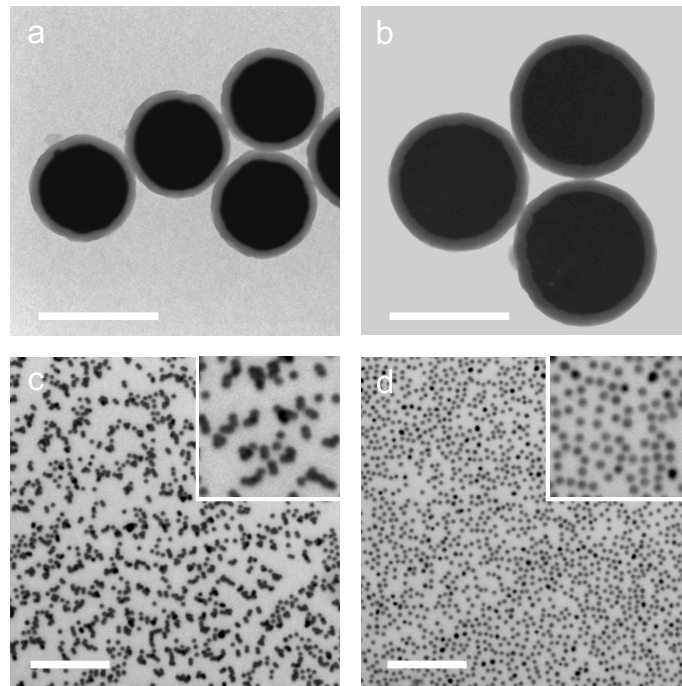


Figure 8.1: Transmission electron microscopy images of silica-core/Au-shell colloids covered with an outer silica shell: system A (a) and B (b). Both are on the same scale; the scale bar measures 500 nm. Fig. 8.1(c) and (d) show optical microscopy images in reflection mode of samples with colloids of system A at a high surface coverage, dried without (c) and with (d) use of critical point drying. The insets show an area of $9 \times 9 \mu\text{m}^2$. The scale bars in (c,d) are $10 \mu\text{m}$.

In this Chapter, we investigate the optical properties of spherical and oblate ellipsoidal Au-shell particles with sizes comparable to the wavelength of light. Both experimental data and calculations are presented. First, for spherical particles, we investigate the dependence of the optical extinction spectra on the core radius and shell thickness. The optical extinction spectra of these large particles show higher order plasmon modes as the light cannot polarize the particle homogeneously. The calculations show that, upon an increase in shell thickness, the extinction peaks can either shift towards the blue or red as a result of the competition between the plasmon hybridization (shifting peaks less red for thicker shells) and the size of the particle (shifting peaks more red for larger overall size). Next, we present measurements of the optical extinction of anisotropic Au-shell colloids, both as a function of angle of the incident light relative to the particle orientation and as a function of size aspect ratio. The experimental data are found to be in good agreement with T-matrix calculations for single oblate ellipsoidal Au-shell particles.

8.2 Fabrication

8.2.1 Synthesis of spherical Au-shell colloids

Spherical Au-shell particles were fabricated using the method of Ref. [99] and covered with a thin silica shell. [88] Both systems were purified by repeated sedimentation and redispersion in ethanol. In this Chapter, we will investigate particles consisting of a silica

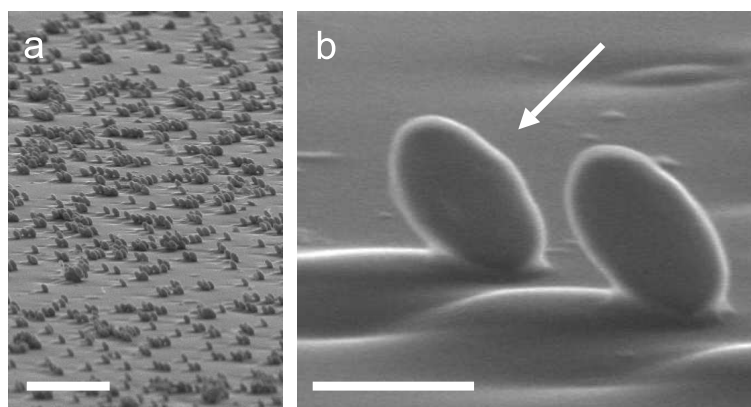


Figure 8.2: Side view SEM images (at 10°) of sample B after irradiation with 4 MeV Xe ions for a fluence of $1 \times 10^{15}/\text{cm}^2$ at an angle of 45° . The particles are all aligned with the short axis in the direction of the ion beam, indicated by the arrow. The scale bars are $5 \mu\text{m}$ (a) and 500 nm (b).

core of radius 156 nm covered with a 25-nm thick Au-shell and a 40-nm thick outer silica shell (system A); and colloids with a silica core of radius 228 nm covered with a 38-nm thick Au-shell and a 60-nm thick outer silica shell (system B). The particle sizes were determined by transmission electron microscopy (TEM). TEM images of both systems are shown in Figs. 8.1(a) and (b). The size polydispersity is 3% for the silica core and about 5% for the Au-shell colloids. From this follows, assuming that the polydispersities are independent, a polydispersity in shell thickness of 10.2 nm (40%) and 15.0 nm (39%) for system A and B, respectively.

8.2.2 Preparation of substrates

Samples for optical measurements were made in the following way. Standard microscope slides of 1 mm or $150 \mu\text{m}$ thickness were cleaned with chromosulphuric acid and then rinsed several times with water and ethanol. The glass slides were then coated with poly(allylamine) hydrochloride (PAH, $M_w = 15000 \text{ g/mol}$) as described in Ref. [152].

Samples of system B were prepared by putting the glass slides in a colloidal suspension in ethanol with a concentration of $8.8 \times 10^7 \text{ particles mL}^{-1}$ with a filling height of 0.8 cm and the colloids were allowed to sediment for at least 6 h. After that, the solvent was carefully removed with a pipette and the samples were dried in air. Samples fabricated by method B contain both single and clustered particles. All samples have a coverage of less than a monolayer, see Fig. 8.1 and 8.2(a).

For system A, deionized water with a resistivity of $18 \text{ M}\Omega$ (Millipore) was further deionized by use of ion resin beads (Biorad AG 501-X8). Prior to the sedimentation step, the colloids were dispersed into the purified water to increase the thickness of the electrostatic double layer of the (negatively) charged colloids. A droplet of the suspension was then put on the (positively-charged) PAH-coated substrate and the colloids were allowed to sediment for 3 hours. Critical point drying with liquid CO_2 (Baltec CPD030) was used to prevent colloid clustering and/or removal by the surface tension forces that otherwise would occur during drying. This effect is clearly seen in the optical reflection microscopy images in Fig. 8.1(c,d). Two samples with the same colloid coverage were dried in air (c)

or with critical point drying (d). Whereas the sample dried in air has a considerable number of clustered particles, the sample made by use of critical point drying only contains single, non-touching particles.

8.2.3 Ion irradiation

MeV ion beam irradiation was used to change the shape of the colloids from spherical to oblate ellipsoidal. [151] After the irradiations, the average aspect ratio (major over minor-axis) of the colloids was determined by scanning electron microscopy (SEM). Samples with colloids of system A were irradiated by 6 MeV Au³⁺ ions at an angle of $45\pm 5^\circ$ to fluences of 4×10^{14} cm⁻², 7×10^{14} cm⁻² and 1×10^{15} cm⁻², yielding size aspect ratios of 1.3 ± 0.15 , 1.5 ± 0.2 and 1.7 ± 0.2 , respectively, as deduced from SEM. Samples with colloids of system B were irradiated with 4 MeV Xe⁴⁺ ions at an angle of $45\pm 5^\circ$ to a fluence of 1×10^{15} cm⁻². The size aspect ratio of the colloids was 1.8 ± 0.2 . SEM images of irradiated colloids of system B, taken at a side view angle of 10° with the sample surface are shown in Fig. 8.2. It is clear from these images that the particles are aligned in the direction of the ion beam.

8.2.4 Optical extinction

Optical extinction measurements were done using a dual-beam Cary 5 spectrophotometer. The samples, covered with immersion oil to match the refractive index of the silica substrate (Cargille Inc., Type B, Formula Code 1248, $n = 1.5150$), were mounted on a rotatable sample holder. The illuminated area was reduced by use of circular pinholes with a diameter of 1 mm.

8.3 Spherical Au-shell particles

The optical properties of Au-shell colloids are very sensitive to the dimensions of the dielectric core and metal shell. [135] Optical extinction measurements can thus provide information about these dimensions. In this section, we will compare measured extinction spectra to Mie calculations of the extinction efficiency. [34] The extinction efficiency is defined as the extinction cross section normalized by the geometrical cross section of the particle.

Figure 8.3 shows the measured extinction spectra for spherical particles of system A (a) and system B (c) embedded in immersion oil (solid line). The spectrum of system A shows three peaks at wavelengths of about 680 nm, 820 nm and 1434 nm; the spectrum of system B is less structured and shows a broad peak at 600–850 nm. In the same panels, the results of calculations for single particles are shown (dashed lines). The calculations were done using the size parameters from TEM as input parameters (system A: $R_{core} = 156$ nm, $t_{Au} = 25$ nm; system B: $R_{core} = 228$ nm, $t_{Au} = 38$ nm). The experimental dielectric constants of Au by Johnson and Christy [36] were used to model the gold shell. The calculation for system A reproduces the main features in the experiment quite well. For system B, the agreement is less good although the main peak around 500–800 nm is observed both in the experiment and the calculation. The fact that the peak structure in the experiment is not as sharp or even absent as in the calculation, is ascribed to the

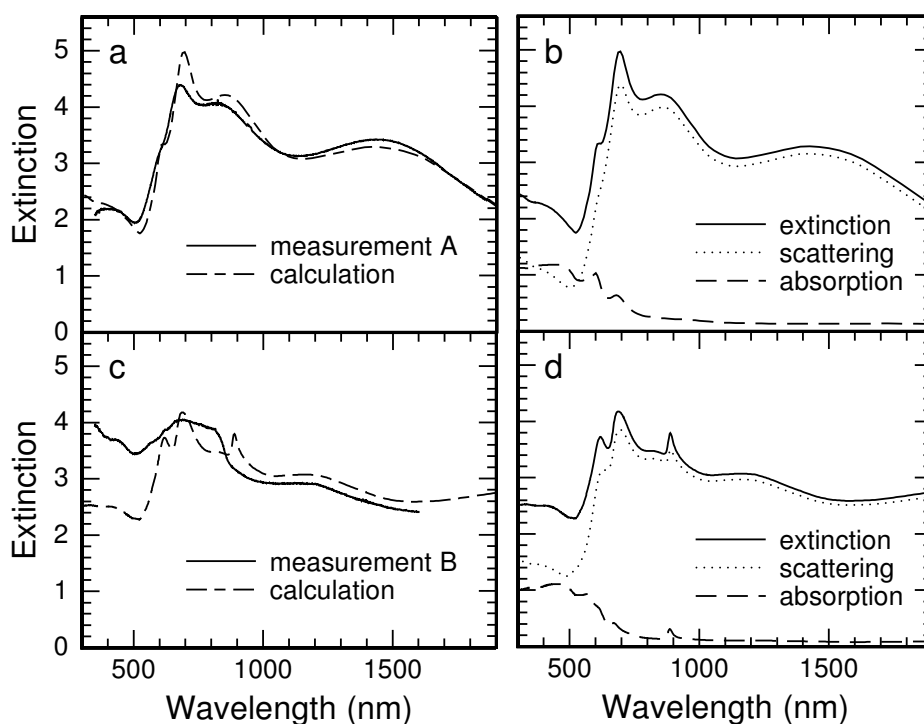


Figure 8.3: Optical extinction measurements (solid line) and calculations (dashed line) for Au-shell particles of system A (a) and system B (c). The embedding medium is oil. Calculations were done for particles with dimensions $R_{core} = 156$ nm and $t_{Au} = 25$ nm [system A, (b)] and $R_{core} = 228$ nm, $t_{Au} = 38$ nm [system B, (d)]. The contributions of scattering (dotted line) and absorption (dashed line) to the extinction (solid line) of the calculations shown. The measured extinction spectra were scaled to overlay the calculated spectra.

particle size inhomogeneity (see below), and possibly by some particles touching each other [Fig. 8.1(c)]. Figures 8.3(b,d) show the contributions of the scattering (dotted line) and the absorption (dashed line) to the extinction efficiency (solid line). As can be seen, the extinction for particles of this size is mainly caused by scattering rather than by absorption.

The dependence of the extinction spectra on the size of the core and the thickness of the shell was studied by Mie calculations, concentrating on the size range of the colloids of system A [Fig. 8.3(a)]. Figures 8.4(b-d) show the results of calculations for core radii of 153 nm, 156 nm and 159 nm. In each panel, graphs are shown for four different shell thicknesses: 20, 25, 30 and 35 nm. To facilitate the comparison between experiment and theory, the measured extinction spectrum of Fig. 8.3(a) is shown in the top graph. The peaks in the spectrum are labelled with D, Q and O, referring to the dipole, quadrupole and octupole modes, respectively. Fig. 8.4(b) shows the results for a fixed core radius of 153 nm. As the shell thickness increases from 20 nm (dotted line) to 35 nm (solid line), several changes in the spectrum are observed. The largest change is seen for the quadrupole peak which almost vanishes for increasing shell thickness. The same trends are observed for core sizes of 156 nm [Fig. 8.4(c)] and 159 nm [Fig. 8.4(d)]. By comparison of the calculated and measured spectra, we deduce that the shell thickness of the

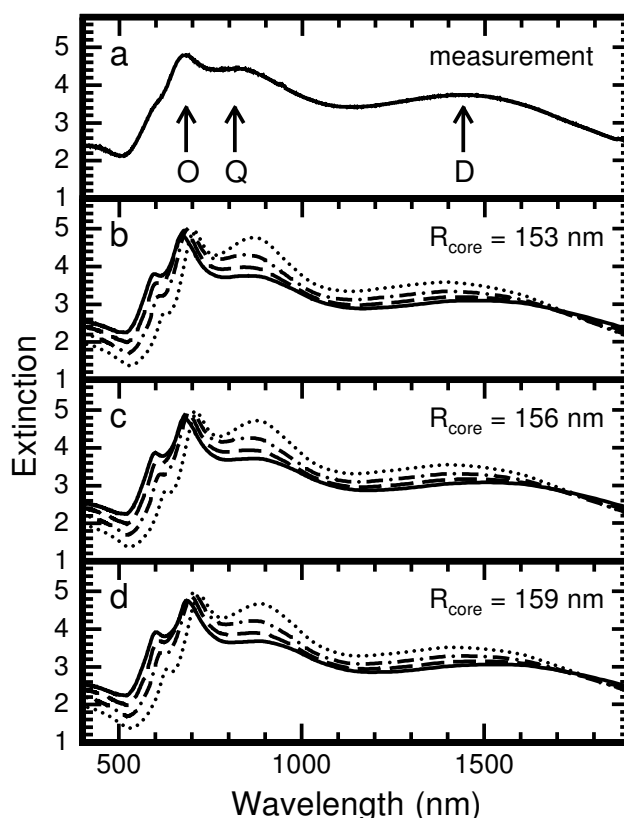


Figure 8.4: Measured extinction spectrum of system A (a) and calculations of the extinction for Au-shell particles with a core radius of 153 nm (b), 156 nm (c) and 159 nm (d). The thickness of the Au-shell is 20 nm (dotted), 25 nm (dash-dot), 30 nm (dash) and 35 nm (solid lines). The peaks are labelled with D (dipole), Q (quadrupole) and O (octupole).

colloids is in the range of 25–30 nm, in agreement with TEM data.

The positions of the octupole, quadrupole and dipole peaks were determined from the extinction spectra, and plotted versus total particle radius in Fig. 8.5. Data are plotted for three different core radii (153, 156 and 159 nm), and the curves thus reflect the effect of varying the shell thickness. Fig. 8.5 shows that for a fixed total radius of 181 nm (i.e., the size of colloids of system A), the peak wavelengths of the octupole and quadrupole mode are very sensitive to both the core radius and the shell thickness: a change of only 6 nm in core radius (e.g., from 153 nm to 159 nm, i.e., a change in shell thickness from 28 to 22 nm) causes a red-shift of about 40 nm. In measurements on large ensembles of particles, small size variations will thus result in a broadening and flattening of these peaks.

The observed blue-shift of the octupole peak [Fig. 8.5(a)] for increasing total radius is ascribed to the reduced interaction between the plasmon modes at the inner and outer boundary of the Au-shell. The quadrupole [Fig. 8.5(b)] and dipole modes [Fig. 8.5(c)] show a more complex dependence on size. For thin shells a decrease with increasing shell thickness is observed, as for the octupole mode, but for larger shell thickness an increase

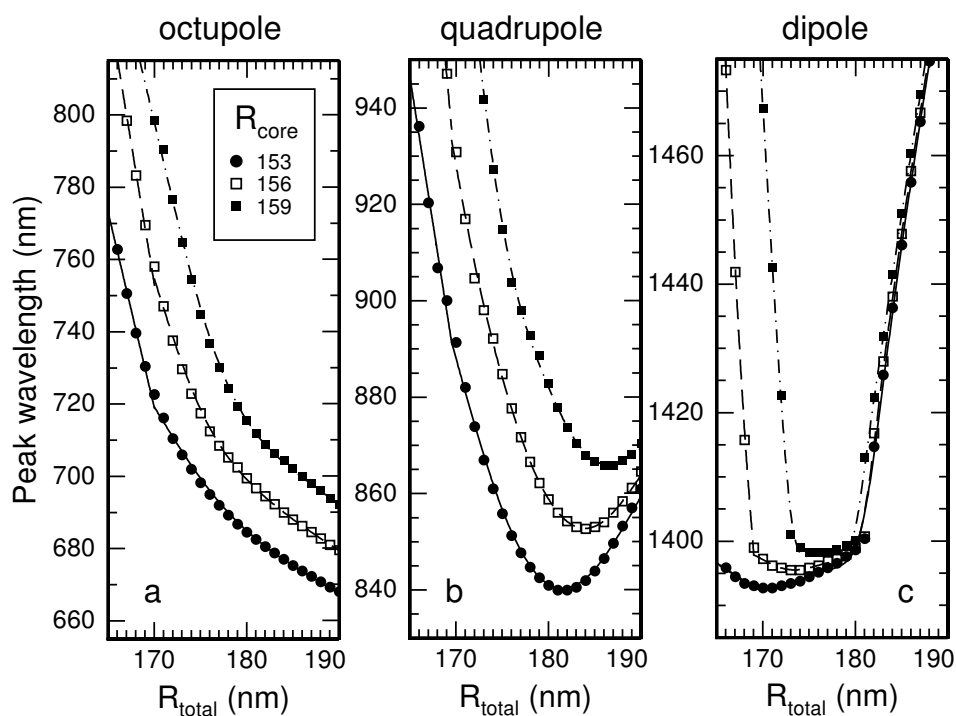


Figure 8.5: Resonance wavelength of the octupole (a), quadrupole (b) and dipole (a) extinction peaks versus total radius, for silica-core/Au-shell spheres with core radii of 153 nm (circles), 156 nm (open squares) and 159 nm (filled squares). The embedding medium is silica.

in resonance wavelength is observed. This is ascribed to phase retardation effects, that are known to red-shift the resonance wavelength for increasing size. [34, 37] Indeed, the observed red-shift of the dipole peak for particles with a total radius of 180 nm and larger, is similar to that of solid Au particles of the same size.

We conclude that for the range of size parameters studied here, there is a trade-off between the coupling between the surface plasmons at the inner and outer boundary of the Au-shell (causing a red-shift for thinner shells) and phase retardation effects (causing a red-shift for large particles).

We finally remark that the results of the calculations also depend on the optical constants used to model the Au-shell. The exact dielectric constants of Au by this fabrication method are not known and may differ from literature values. Small variations in optical constants can result in significant peak shifts in the calculations. For example, for a Au-shell particle in silica with a core radius of 156 nm and a Au-shell of 25 nm, the quadrupole extinction peak varies by 15 nm using either (smoothed) data of Palik [35] or those of Johnson and Christy. [36] Also, for very thin metal shells (smaller than ~ 10 nm), the dielectric constant may be size-dependent due to a change in relative contributions of electron scattering at the surface. [34, 37] This would result in a broader and a less structured extinction spectrum. [38] However, recent light scattering measurements on single Au-shell particles suggest that the resonance broadening found in ensemble measurements is mostly due to the polydispersity in size. [39]

In the following sections, we will use the particle dimensions obtained from TEM

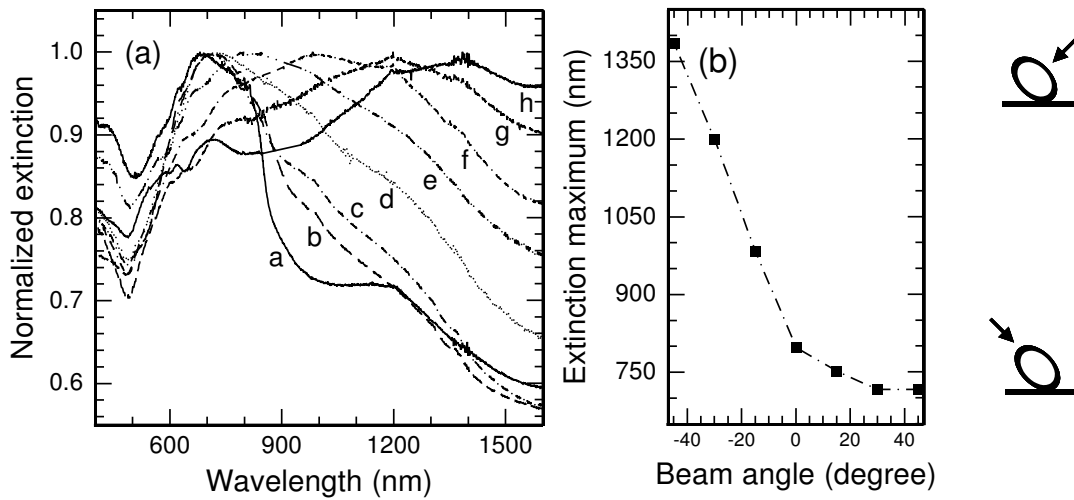


Figure 8.6: Optical transmission spectra of ion irradiated Au-shell colloids of system B as a function of angle of the incident light beam [Fig. 8.6(a)]. The angle was varied from -45° (i.e., parallel to ion beam direction, spectrum h) to $+45^\circ$ (i.e., perpendicular to the ion beam direction, spectrum b) in steps of 15° . The transmission spectrum for spherical colloids is shown for reference (spectrum a). The maxima of the spectra in Fig. 8.6(a) are plotted in Fig. 8.6(b) as a function of the angle of the incident optical beam.

measurements as input for the calculations, and continue to use bulk dielectric constants for Au from Johnson and Christy.

8.4 Anisotropic Au-shell particles

8.4.1 Angle-dependent extinction

Angle-dependent extinction spectra were measured using a rotatable sample holder and unpolarized light. Fig. 8.6(a) shows the normalized extinction spectra of the sample with ion beam-deformed colloids of system B, taken at different angles of the incident light with respect to the surface normal. Measurements were done at angles of -45° (spectrum h, i.e., light approximately along the ion beam direction) to $+45^\circ$ (spectrum b, perpendicular to the ion beam) in steps of 15° . When converted using Snell's law, this external angular range corresponds to $-29^\circ - +29^\circ$ inside the sample ($n = 1.5$). As a reference, spectrum (a) in Fig. 8.6(a) shows the extinction of a sample with unirradiated, spherical colloids. We observe that the extinction of the anisotropic colloids is broader and strongly angle-dependent: the maximum in extinction shifts to the infrared for angles more parallel to the ion beam direction. This shift is clearly seen in Fig. 8.6(b), where the extinction maxima are plotted as a function of angle of incidence. We observe that the extinction maximum ranges between ~ 700 nm and 1400 nm. Note that the orientation was given incorrectly in Ref. [151]

The influence of the aspect ratio on the spectral shift was investigated in more detail using sample A in which calculations showed a closer match with experimental data [see Fig. 8.3(a)] and where no particles were in contact. As a reference, the spectra of spherical

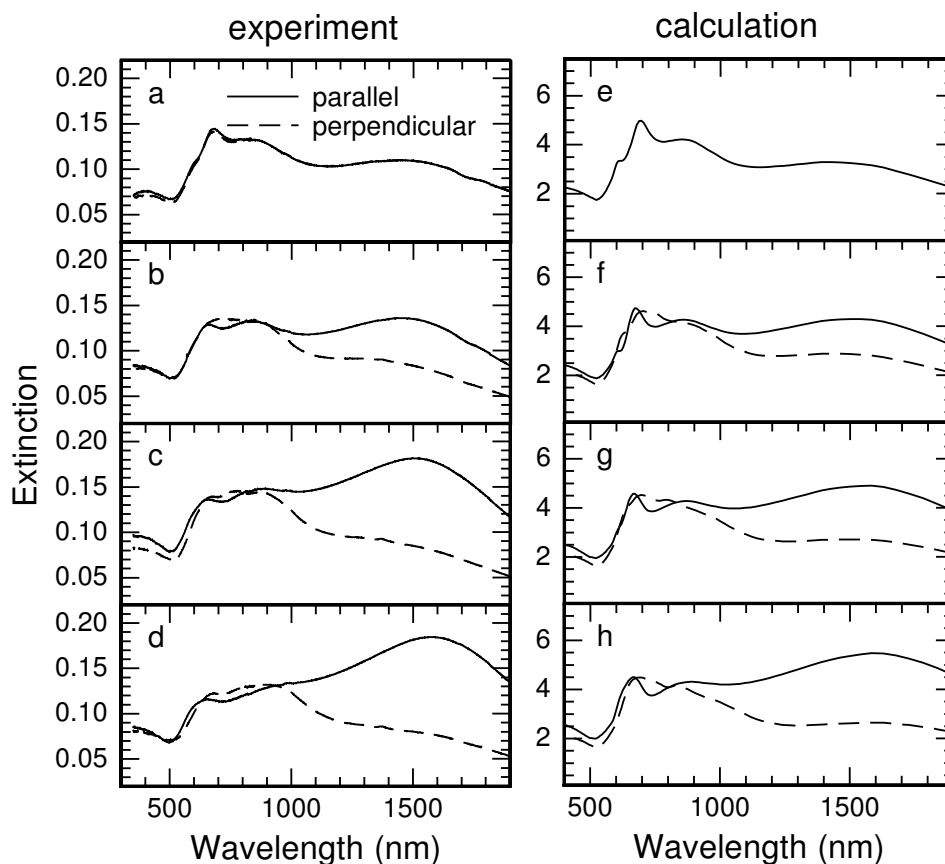


Figure 8.7: Optical extinction spectra for unpolarized light of spherical (a) and irradiated (b-d) Au-shell particles (system B) measured at an angle of -45° (solid lines) and $+45^\circ$ (dashed lines) to the sample normal. After ion irradiation at 45° to fluences of 4×10^{14} ions cm^{-2} (b), 7×10^{14} ions cm^{-2} (c) and 1×10^{15} ions cm^{-2} (d), the two spectra are different. T-matrix calculations of an oblate Au-shell particle with aspect ratios of 1.0 (e), 1.3 (f), 1.5 (g) and 1.7 (h) at constant volume show quantitatively the same behavior.

colloids taken at angles of -45° and $+45^\circ$ are shown in Fig. 8.7(a). As expected, there is no noticeable distinction observed in these spectra when the angle is varied. Figures 8.7(b-d) show the extinction spectra for unpolarized light measured on oblate ellipsoidal particles with an aspect ratio of 1.3 ± 0.15 (b), 1.5 ± 0.2 (c) and 1.7 ± 0.2 (d). A clear difference between the two spectra is observed, even for the smallest size aspect ratio of 1.3. For light incident at -45° (parallel to the ion beam direction, solid lines), we observe that the extinction in the infrared part of the spectrum (region of the dipole mode) is enhanced. The relative contribution of the quadrupole and octupole peaks also changes. For light incident at $+45^\circ$ (perpendicular to the ion beam, dashed lines), the extinction peak in the infrared is decreased, and a broad extinction peak is observed around 700 nm. Quantitatively similar effects, but more pronounced are observed for particles with a larger anisotropy. As the particle anisotropy is increased, the dipole mode shows a gradual red-shift, which is ascribed to retardation effects, as with increasing size aspect ratio (fluence) the dimensions of the long axes become larger.

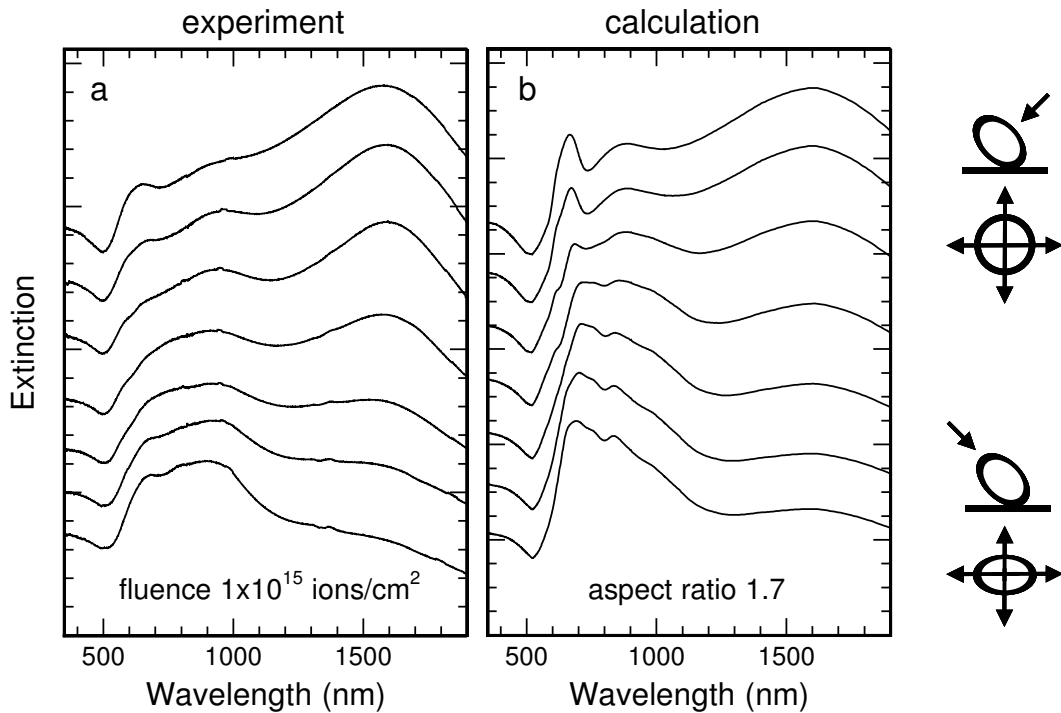


Figure 8.8: Optical extinction measurements (a) and calculations (b) for Au-shell particles with aspect ratio of 1.7 at angles from -45° (top) to $+45^\circ$ (bottom) in steps of 15° (unpolarized light). Spectra are shifted vertically for clarity.

Calculations of the optical extinction were done for an oblate ellipsoidal silica-core/Au-shell particle in silica using the T-matrix method. [41, 153–156] A spherical particle with a silica core with radius of 156 nm covered by a 25-nm thick Au-shell was used as a starting point. The shape of the particle was then changed into an oblate ellipsoid by keeping the volume constant. The core and the shell are considered as two concentric ellipsoids with the same aspect ratio, in which case the shell thickness is not constant over the particle. This shape is predicted by the viscoelastic model that describes the ion beam deformation experiments very well. [57, 92] Figure 8.7 shows the results for aspect ratios of 1 (e, sphere), 1.3 (f), 1.5 (g) and 1.7 (h). These aspect ratios equal the size anisotropy of the colloids found in SEM. The calculation results resemble many of the features observed in the experiments [Figs. 8.7(a-d)], both for the orientations parallel (solid lines) and perpendicular (dashed lines) to the symmetry axis of the particles. For example, the blue-shift of the octupole peak, the red-shift of dipole peak, and the difference in extinction in the IR part of the spectrum for two orientations are well reproduced. The calculations also show that for unpolarized light incident perpendicular to the symmetry axis, in contrast to the orientation parallel to the symmetry axis, the peak structure is broad and without much structure, as is observed experimentally.

While Fig. 8.7 presents extinction data for light incident parallel and perpendicular to the symmetry axis, Fig. 8.8 shows the extinction taken over a range of angles for the sample with the highest aspect ratio (fluence $1 \times 10^{15} \text{ cm}^{-2}$, aspect ratio 1.7). The angle of the incident light with respect to the surface normal is changed from -45° to $+45^\circ$, in

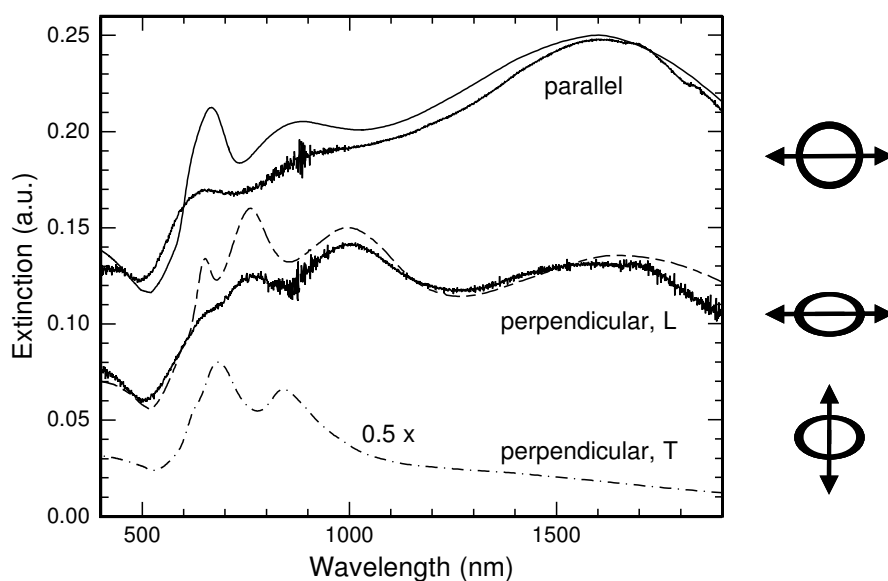


Figure 8.9: Optical extinction spectra of oblate ellipsoidal Au-shell particles with aspect ratio of 1.7 using light polarized along the long axis of the particles. Light is incident parallel (top) and perpendicular (center) to the symmetry axis. The top graph is shifted vertically for clarity. Calculation results are represented by thin lines, and include the spectrum for light perpendicular to the symmetry axis with the polarization along the short axis (dash-dotted line).

steps of 15° . The spectra are plotted with a vertical offset for clarity. As the angle is changed from -45° (top, parallel) to $+45^\circ$ (bottom, perpendicular), we observe a gradual change in the shape of the spectra: the extinction in the infrared part (dipolar mode region) decreases, and the extinction at 500–1000 nm (higher order modes) becomes one distinct, but broad peak.

A better understanding of the spectral shapes can be obtained from extinction measurements with polarized light. Fig. 8.9 shows two measured extinction spectra for particles with an aspect ratio of 1.7 (system A, fluence $1 \times 10^{15} \text{ cm}^{-2}$), each with the polarization of the incident light beam parallel to one of the long axes of the oblate ellipsoidal particles (see the schematic in the Fig. 8.9). In the same graph, the results of the calculation are plotted for the same orientation and polarization of the incident light (thin solid and dashed lines). The calculations match the experimental dipolar peak around 1600 nm rather well, and show a double and triple peak structure between 600 and 1000 nm for the two incident directions. These peaks are also observed experimentally, though less pronounced. In the quasi-static limit, in which the particle size is much smaller than the wavelength of light, the resonances related to the long axes of an oblate ellipsoid only depend on the aspect ratio of the particle, not on the orientation of the particle with respect to the propagation direction of the light. [34] The particles in this experiment have sizes comparable to the wavelength of light. Light incident perpendicular to the symmetry axis has a longer optical path *in* the particle than light incident parallel to the symmetry axis of the particle, and can thus experience more phase retardation. Therefore, the peaks are shifted towards the red and a new higher order mode becomes visible at 660 nm.

The experimental and calculated extinction spectra for polarized light incident along

the symmetry axis in the top graphs of Fig. 8.9 are similar to the corresponding spectra obtained with unpolarized light (top spectra in Fig. 8.8). Indeed, this is what we expect for light parallel to the symmetry axis of the oblate ellipsoidal particles, as this orientation is polarization independent (circular cross section).

Fig. 8.9 also shows the calculation result for light incident perpendicular to the symmetry axis of the particle, but with polarization along the short axis of the particle (dash-dotted line, bottom graph). The spectrum is divided by a factor of two for clarity. Two peaks are observed, and their position is shifted with respect to the peaks in the spectrum for polarization along the long axis of the particle. The sum of the two spectra for polarized light (for light incident perpendicular to the symmetry axis) gives the broad and unstructured peak in the spectrum observed for unpolarized light [e.g., Fig. 8.7(d)].

8.5 Conclusions

In conclusion, we have investigated the optical properties of spherical and oblate ellipsoidal Au-shells. We showed that the optical extinction is determined both by the size of the particle and the thickness of the Au-shell. Extinction measurements on the anisotropic particles, fabricated and aligned using MeV ion irradiation, show a strong dependence on the angle of incidence. For example, the peak associated with the dipole mode of the particle, in the infrared part of the spectrum, is favored for light incident along the short axis of the particle and red-shifts as the aspect ratio is increased. The agreement between calculations for single particles and the ensemble averaged experimental data is very good.

Acknowledgements

Christina Graf is acknowledged for the synthesis of the Au-shell particles and the optical measurements of system B. The Mie and T-matrix codes were written by Alexander Moroz. Job Thijssen (Utrecht University) is acknowledged for stimulating discussions. Prof. Dr. L. W. Jenneskens and Dr. C. A. van Walree (Utrecht University) are thanked for the use of the CARY 5 spectrophotometer.

Optical cavity modes in gold shell particles

Gold (Au) shell particles with dimensions comparable to the wavelength of light exhibit a special resonance, with a tenfold field enhancement over almost the entire dielectric core at resonant excitation. Full-field finite difference time domain simulations and T-matrix calculations show that the resonance frequency of this mode is sensitive to the dielectric constant, size and shape of the dielectric core. For anisotropic oblate Au-shells, the resonance frequency shifts towards the red for plane-wave illumination polarized along the short axis of the particle in agreement with an ellipsoidal cavity in a metal surrounding. This cavity-mode has a quality factor of 35 and may be used in nano-engineered light sources, lasers, or sensors.

9.1 Introduction

Small (noble-)metal particles exhibit interesting optical properties due to the collective oscillation of conduction electrons (surface plasmons). This localized surface plasmon mode causes confinement of the electromagnetic field near the surface, and leads to strong absorption and scattering in the visible and near-infrared depending on geometry, size and shape of the metal particle. The enhanced local fields can be used to enhance the fluorescence emission of dyes close to the metal surface [157], to give increased signals in Raman spectroscopy [158, 159], or to increase the photostability of photoluminescent dyes by shortening the excited-state lifetime. [160, 161]

The strength of the local electric field strongly depends on the shape and size of the metal particle. The highest field enhancements are obtained at the plasmon resonance frequency and close to highly curved surfaces. The plasmon frequency of most noble metals occurs in the visible for solid particles. [37] Dielectric-core/metal-shell particles exhibit a larger tuning range: the plasmon frequency can be tuned throughout the visible and near-infrared spectrum by a change in relative dimensions of the core and the shell. [44, 135, 136] Additional tunability can be obtained by shape anisotropy, that induces a splitting of the plasmon resonance in blue-shifted transverse and red-shifted longitudinal plasmon bands. [34, 138] (see Chapter 8)

The near-field optical response of metallic particles to the incident light wave can be calculated by a variety of methods. Geometries with a high degree of symmetry are usually treated by analytical Mie theory and the T-matrix method (Chapter 8, Ref. [34]). Numerical methods such as the discrete dipole approximation (DDA) and the finite difference time domain method (FDTD) are more versatile than exact methods in the sense that non-symmetrical structures (e.g., triangles, arrays of metal particles, particles with rough surfaces) and non-symmetrical situations (e.g., particles on a substrate) can be treated as well. [16, 33, 162–164] Optical absorption and scattering, as well as the local electromagnetic fields and induced charge densities at the surfaces, can be calculated with these methods.

Surface enhanced Raman spectroscopy (SERS) measurements on spherical metal-shell particles show a Raman signal enhancement by a factor of 10^6 in solution and 10^{10} on substrates, when compared to Raman spectra taken away from the metal. [159, 165, 166] In SERS, the total electromagnetic contribution is generally considered to be proportional to the fourth power of the electric field. Experiments and calculations indicate that the enhancement of the SERS signal is maximal for small particles with core radius in the size range of 50-100 nm. [159] The surfaces of the metal-shell colloids can be very rough as a consequence of the fabrication method and can thus give rise to “hot spots” in the electromagnetic field density. The effect of the surface roughness on the near-field distribution of the electric field was therefore studied by FDTD. [163] For single nanoshells of 50 nm in radius, it was found that the surface roughness and defects in the shell affected the local field enhancement significantly. However, far field properties (optical absorption and scattering) were found to be remarkably insensitive. It was also shown by FDTD calculations that, for longitudinal excitation of prolate (rod-like) Au-shell particles with a size aspect ratio of 6.3, local field intensity enhancement factors can be as high as 7000 with a large enhancement extending several tens of nanometers from the surface of the particle. [138]

In contrast to SERS, the enhancement of the luminescence intensity by the plas-

mon fields is limited by non-radiative energy transfer to the surface plasmons in the metal. [167, 168] This luminescence quenching takes place at small distances (< 10 nm) between the dye and the metal. At larger distances, however, the electromagnetic field enhancement by the surface plasmon in the metal is still present and fluorescence enhancement may be observed. As a result, there is an optimal distance between the dye and the metal for fluorescence enhancement, typically in the range of 20 to 40 nm. [157, 161]

In this chapter, FDTD and T-matrix calculations are employed to study the plasmon resonances and field distributions in large Au-shell particles with dimensions comparable to the wavelength of light. The calculations are inspired by the work on oblate ellipsoidal Au-shells made by MeV ion irradiation as described in Chapter 7 and Ref. [151]. Resonance frequencies and local fields are obtained from FDTD calculations and compared to far field absorption and scattering spectra obtained from T-matrix calculations. In addition, FDTD simulations provide insight in the dynamics of the time evolution of the electromagnetic field in and close to the particle. Both spherical and anisotropic Au-shells are considered.

The results indicate that Au-shell particles with a diameter of the order of the wavelength of light show a strong resonance with a ten-fold enhanced electric field throughout the entire dielectric core. From the dependence of the resonance frequency on size and dielectric constant of the dielectric core, we conclude that it is a geometric cavity mode. This is further supported by the observation of a blue-shift of the resonance frequency for longitudinal polarization and a red-shift for transverse polarization for oblate Au-shells. Since the field enhancement occurs in a large volume, not only close to the metal, this cavity-based resonance may be useful for the enhancement of luminescence of optical emitters (such as quantum dots, dyes, rare-earth ions) placed in the dielectric core. [169]

9.2 FDTD calculation scheme

Three-dimensional full-field electromagnetic simulations based on finite difference time domain techniques were employed to study the electromagnetic field distributions of spherical and anisotropic Au-shell colloids. [131] The dielectric core of the Au-shell particle has a radius of 228 nm and is covered by a 38-nm thick Au layer (after Ref. [151]). The embedding medium is taken equal to that of the core material, with a dielectric constant of $\epsilon = 2.10$ (silica). The optical response of gold is modelled using the Drude model:

$$\epsilon(\omega) = \epsilon_{high} - \frac{\omega_p^2}{\omega^2 - i\omega\gamma} \quad (9.1)$$

with $\epsilon_{high} = 9.54$, $\omega_p = 1.35 \times 10^{16}$ rad s $^{-1}$ and $\gamma = 1.25 \times 10^{14}$ s $^{-1}$, which provides a reasonably good fit to tabulated experimental data [36] for photon energies smaller than 3 eV.

The particle is placed in the center of a rectangular simulation box with dimensions about three times the particle size. For example, the box' dimensions for a sphere of 266 nm in radius were $1.3 \times 1.3 \times 1.3 \mu\text{m}^3$ and for an oblate ellipsoid with aspect ratio of 2.5, the simulation box measured $1.5 \times 1.5 \times 1.0 \mu\text{m}^3$. Due to the large field gradients near the curved metal surfaces, the standard grid with equal mesh size throughout the domain is not well suited. Therefore, an algorithm was used that allows a finer mesh near the metal region. The mesh cell density had a linear gradient of 10:1, with the finest mesh close to the particle. Due to computer constraints, the number of mesh cells was limited to

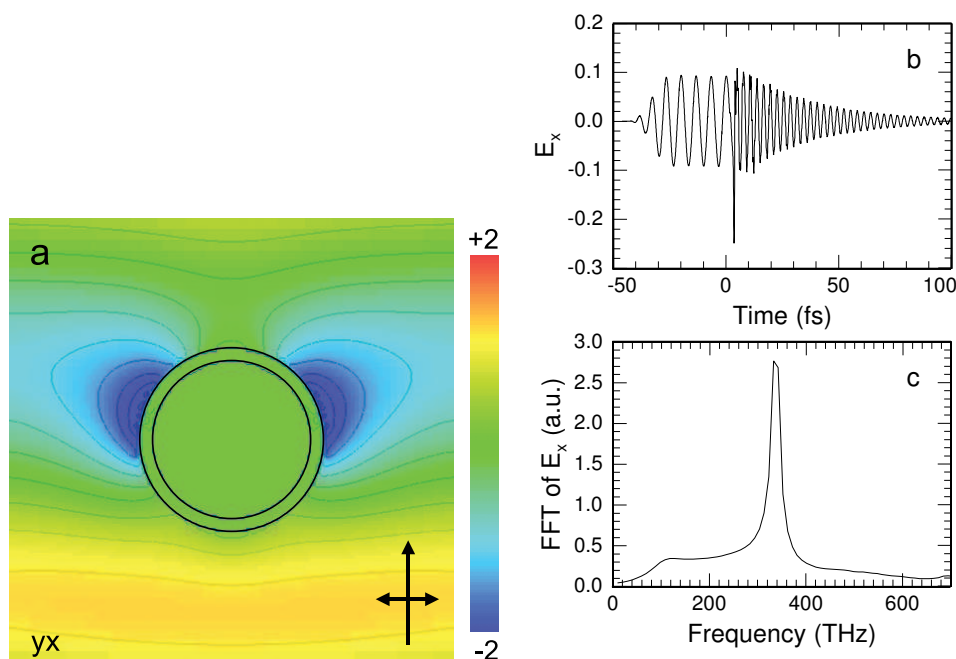


Figure 9.1: [color] (a) FDTD calculation snapshot [at $t = 0$ in Fig. 9.1(b)] of the x-component of the electric field of a plane-wave propagating in the y-direction, at a frequency of 150 THz, and interacting with a spherical Au-shell ($R_{core} = 228$ nm, $t_{Au} = 38$ nm) in silica. The plane-wave is polarized horizontally in the plane (double arrow) and its amplitude is normalized to 1 V/m. The color scale ranges from -2 to +2. The difference between two consecutive contour lines is 0.4. The two concentric circles indicate the inner and outer boundary of the gold shell. (b) The excitation and relaxation trace of the x-component of the electric field in a monitor point in the center of the particle. The plane-wave is turned off at $t = 0$. (c) Fast Fourier transform of the decay of the x-component of the electric field, showing a resonance peak at a frequency of 335 THz.

3 million grid cells. This means that for the large particles under consideration, the cells in the immediate vicinity of the particle had a width of about 5 nm and those on the outer boundary of the simulation volume had widths of about 35 nm. The simulation results were found to be robust against small changes to mesh cell density. In all simulations, the incident light was linearly polarized along one of the main axes of the particle.

A two-step process was used to determine the particle-plasmon resonant mode and its frequency. First, the simulation volume is illuminated by a switched-on propagating plane-wave with an off-resonance frequency that allows the particle to get polarized and store energy. Second, the incident field is switched off and the electric field amplitude is monitored in the time domain as the particle modes excited by the incident plane-decay (ring down). This signal is transformed into the frequency domain by a fast Fourier transform (FFT) to provide information on the particle resonances. Once the resonance frequencies are determined in this way, on-resonance excitation is used to excite individual modes to examine the corresponding spatial distribution of the field intensity. Such distributions can be used to discriminate between spectral features which correspond to physical resonances and unphysical artifacts of the simulation or of the frequency domain transform. For example, small “hot spots” can occur in the intensity maps as a result of faceted corners in the rendering of the curved surfaces.

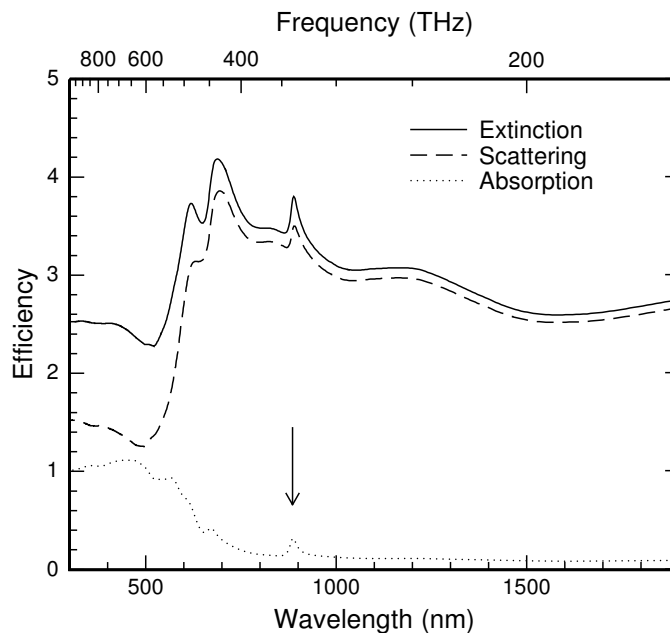


Figure 9.2: T-matrix calculation of extinction (solid), scattering (dashed), and absorption (dotted line) cross section efficiency spectra of a Au-shell sphere in a silica matrix ($R_{core} = 228$ nm, $t_{Au} = 38$ nm). The resonance peak at 885 nm is indicated by an arrow.

9.3 Au-shell sphere

Figure 9.1 illustrates the different steps in the FDTD calculation. A snapshot in time of the electric field is shown in Fig. 9.1(a) for an incident plane-wave at an off-resonance frequency of 150 THz (free space wavelength $\lambda = 2.0$ μm), interacting with a Au-shell particle with a core radius of 228 nm and a Au-shell thickness of 38 nm. The image shows the plane that contains both the propagation direction of the plane-wave (indicated by the vertical arrow) and the polarization (indicated by the horizontal arrow). Close to the metal shell, the amplitude of the electric field is enhanced by about a factor of 3 (not seen in the Fig. 9.1(a), due to saturation of the color scale). Figure 9.1(b) shows the time evolution of the electric field amplitude in a monitor point at the center of the particle. The incident plane-wave is switched off at time $t = 0$, whereupon the particle's relaxation is observed. The FFT of the decay trace is shown in Fig. 9.1(c), and reveals a main resonance peak at 335 THz ($\lambda = 895$ nm).

Since the absorption and ringdown are resonant phenomena, the frequency at which the peak FFT response occurs is directly comparable to the frequency of maximum absorption in an optical spectrum. Figure 9.2 shows the extinction spectrum of the Au-shell particle as calculated by the T-matrix method (solid line). The contributions of absorption (dotted line) and scattering (dashed line) are shown as well. The spectra show that the extinction for this particle is mainly due to scattering. Tabulated optical constants for Au by Johnson and Christy were used for the calculation of these spectra. [36] Therefore, the contribution of the interband transitions at wavelengths smaller than 600 nm is also observed in the absorption spectrum. These are absent in the FDTD calculation as this employs a Drude model for the dielectric constants. The absorption spectrum in Fig. 9.2

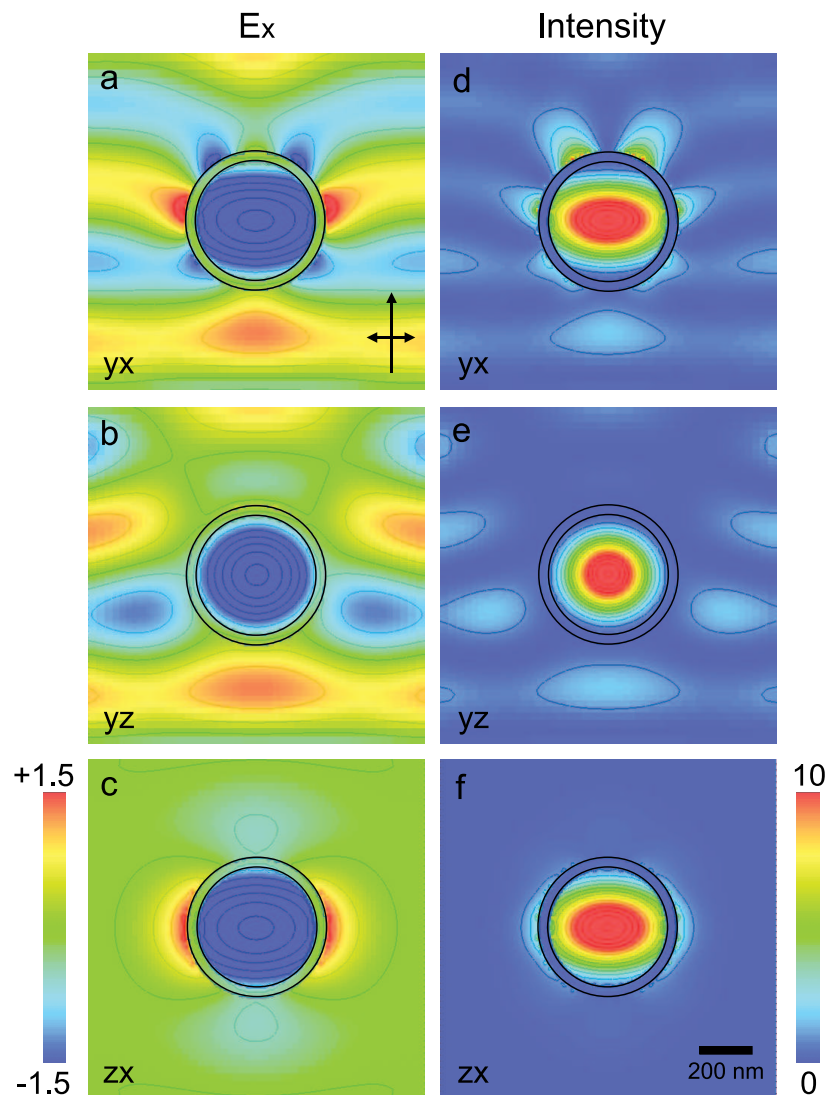


Figure 9.3: [color] FDTD time snapshot of the x-component (left) and intensity (right) of the electric field in the yx -plane (a, d), yz -plane (b, e), and zx -plane (c, f). On-resonance plane-wave excitation at 335 THz of a spherical Au-shell in silica ($R_{core} = 228$ nm, $t_{Au} = 38$ nm). Color scale bars range from -1.5 to 1.5 (a-c) and from 0 to 10 (d-f); the difference between consecutive contour lines amounts to a factor 0.5 (a-c) and 1 (d-f). The plane-wave propagates in the y -direction, and is polarized along x .

also shows a distinct peak at 885 nm (indicated by the arrow), in good correspondence with the resonance frequency at 335 THz observed in the ring down of the FDTD calculation. FDTD calculations using this two-step method thus lead to the identification of resonances of the particle for which energy is stored in the system in absorption.

The field distributions of this resonance mode are investigated with on-resonance plane-wave excitation at 335 THz. A time snapshot is shown in Fig. 9.3 for a time at which the electric field inside and close to the particle is at a maximum. The x-component of the electric field (direction of polarization) is shown in the contour plots in Figs. 9.3(a-c) on a scale of -1.5 to +1.5. Figures 9.3(d-f) show the electric field intensity normalized to the incident field on a linear scale of 0 to 10. Three different cross sectional planes are shown:

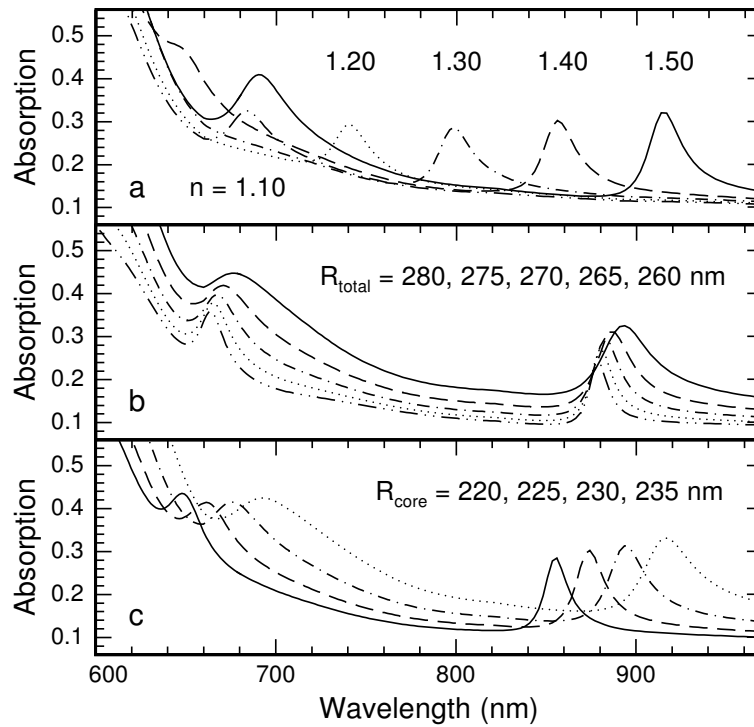


Figure 9.4: T-matrix calculations of optical absorption spectra for spherical Au-shells in silica ($n = 1.45$). (a) for different refractive indices of the core (solid line: 1.50, dash-dot-dotted line 1.1), (b) as a function of total radius at fixed particle radius of 228 nm (solid line: 260 nm, dash-dot-dotted line: 280 nm), and (c) as a function of core radius at a fixed total radius of 266 nm (solid line: 220 nm, dotted line: 235 nm).

the yx -plane containing the direction of propagation and polarization (a, d), the yz -plane perpendicular to the polarization direction (b, e) and the zx -plane, i.e., perpendicular to the propagation direction (c, f).

The images in Fig. 9.3 clearly reveal how the incoming plane-wave interacts with the Au-shell. The phase fronts of the plane-wave can be observed at the boundaries of the simulation volume in the yx and yz -planes. Clearly, the electric field is enhanced close to the outer surface of the Au-shell particle. An enhanced field intensity is also observed in the dielectric core of the particle. Time series of the snapshots of the yx -plane [Fig. 9.3(a)] indicate that the electric field is bound at the outer surface of the metal shell and propagates over the surface, and that the electric field over the full dielectric core of the particle oscillates out of phase relative to the field outside the shell [see e.g., Fig. 9.3(c)], as the plane-wave propagates in time. From the temporal decay of the electric field intensity inside the dielectric core, the quality factor (i.e., the number of oscillation cycles before energy is dissipated) for this cavity mode is found to be 35.

9.4 Cavity mode resonance

For a better understanding of the cavity mode mentioned in Section 9.3, T-matrix calculations were exploited to study the dependence of the resonance frequency on dielectric

constants of core and surrounding medium, and the size of the core and the shell. The results are shown in Fig. 9.4. Figure 9.4(a) shows the large influence of the dielectric constant of the core on the resonance peak: an increase of the refractive index by 0.1 results in a large red-shift of the resonance peak by ~ 55 nm. Changing the core from air ($n = 1.0$) to silica ($n = 1.5$) thus results in a shift of the resonance wavelength over 275 nm. Moreover, for the Au-shell with a dielectric core with refractive index of 1.5, a second peak in absorption is observed, at 685 nm. The effect of the dielectric constants of the surrounding medium on the resonance frequency, however, is found to be negligible (not shown). Only an increase in absorption peak intensity is observed for smaller dielectric constants (a factor of 2 for a silica-core/Au-shell particle placed in air compared to in silica). This demonstrates that the resonance properties of this mode are essentially set by the continuity conditions of Maxwell's equations at the core/shell boundary and not at the boundary between the shell and the surrounding medium.

As was demonstrated in Chapter 8, peaks in optical spectra can show a complex dependency on the dimensions of the core and the total radius. This was attributed to a competition between the effects of retardation (red-shift for larger size) and by the interaction strength between plasmon modes on the inner and outer boundaries of the shell (blue-shift for decreasing shell thickness). Therefore, it is interesting to investigate the response of the resonance peak of the cavity mode to small variations in shell thickness at fixed core radius [Fig. 9.4(b)] and at fixed total radius [Fig. 9.4(c)]. In both cases, the shell thickness is in the range of 30 to 50 nm. For a particle with a fixed core radius of 228 nm, the peak slightly shifts towards the blue for an increase in shell thickness. Indeed, for shell thicknesses studied here (about twice the skin depth of light in Au), the coupling between the plasmon modes at the inner and outer boundary of the Au-shell is expected to be relatively small. Figure 9.4(b) also shows a peak narrowing upon an increase in shell thickness. The red-shift observed in Fig. 9.4(c) for increasing core radius (at fixed total radius) also indicates that the core radius is of main importance to the resonance wavelength. The mode volume of this geometric resonance should be related to the wavelength of the light in the medium. In this case, this is on the order of 600 nm, slightly larger than the actual diameter of the dielectric core (~ 450 nm) and what is suggested by the intensity contour plots in Fig. 9.3. The shell in the simulations is not taken as a perfect conductor, and light can penetrate into the metal.

9.5 Oblate ellipsoidal Au-shells

The FDTD scheme outlined in Section 9.2 was also applied to oblate ellipsoidal shells. The shell particle consists of two concentric oblate ellipsoids (representing the core and the shell), both with the same size aspect ratio. The shell thickness therefore changes over the particle. The volume per component was taken to be equal to that of a Au-shell sphere with core radius of 228 nm and a shell thickness of 38 nm. [151] Figure 9.5(a) shows the normalized FFT spectra for particles with size aspect ratios of 1.0, 1.5, and 2.5. The spectrum of the spherical shell shows only one resonance at 895 nm (335 THz, closed triangles, see Fig. 9.3), whereas the cavity resonance for the anisotropic particles is split. For a polarization along the long axis of the oblate ellipsoidal Au-shell, a blue-shift is observed: the resonance shifts to 830 and 730 nm for aspect ratio of 1.5 (squares) and 2.5 (circles), respectively. The resonances are red-shifted for light polarized along the short

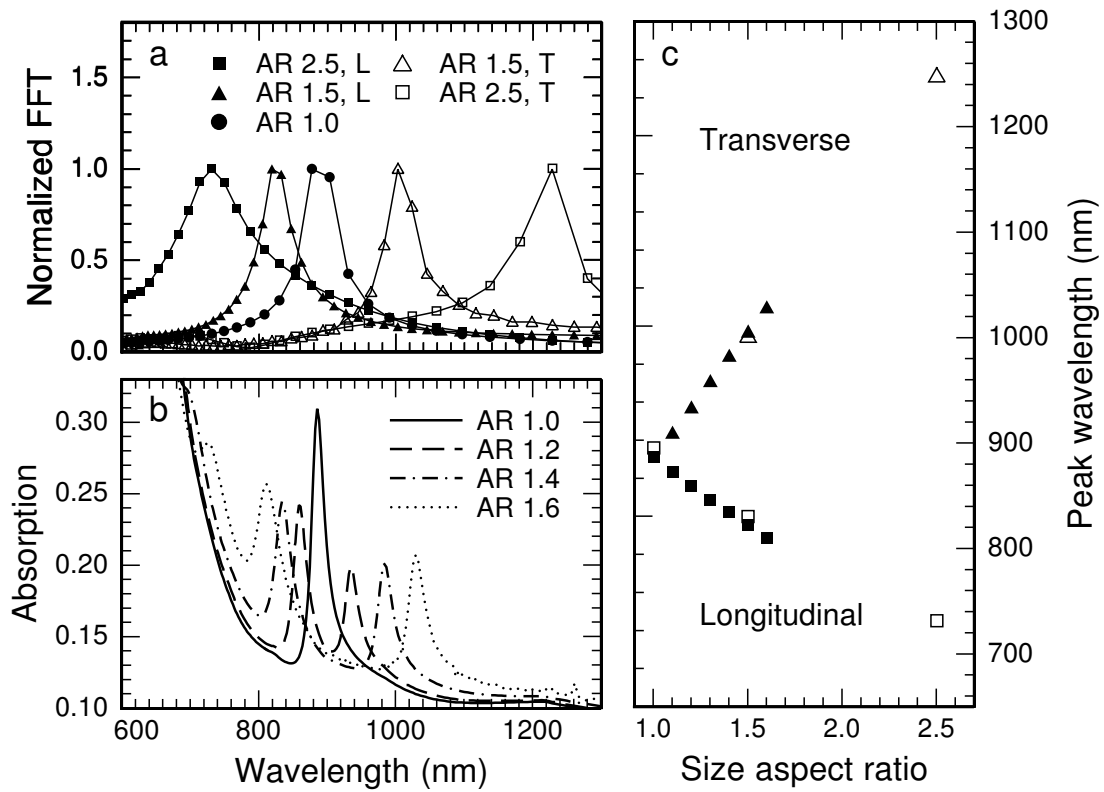


Figure 9.5: Resonances in oblate ellipsoidal Au-shells in silica with volume equivalent of a sphere with core radius 228 nm and a shell thickness of 38 nm. (a) Normalized FFT results from FDTD calculations for aspect ratios of 1.0, 1.5 and 2.5 for polarizations parallel to the long axis (L) and to the short axis (T) of the particle. (b) Orientation averaged absorption for aspect ratios of 1.0 (solid line), 1.2 (dashed line), 1.4 (dash-dotted line) and 1.6 (dotted line) calculated by the T-matrix method. (c) Shift of the peak positions versus aspect ratio for results from FDTD (open) and T-matrix calculations (closed symbols).

axis. This transverse resonance for the oblate ellipsoidal shell with aspect ratio of 1.5 (stars) and 2.5 (open triangles) is observed at 1000 nm and 1250 nm, respectively.

The blue- and red-shift observed for polarization along the long and short axes of the oblate shell, respectively, are opposite to the trends known for dipolar and multipolar modes in oblate metal core and metal-shell particles (also see Chapter 8). In the previous section it was shown that, for the Au-shell under consideration, the cavity resonance is related to the size of the dielectric core only. The Au-shell can thus be modelled as a dielectric void in a metal surrounding.

For simplicity, let us assume that the dielectric is air ($\epsilon = 1$), and that the dielectric constants of the metal are described by a simple Drude model without damping, i.e., $\epsilon = 1 - \frac{\omega_p^2}{\omega^2}$ with ω_p the bulk plasmon resonance. Then, the resonance condition of an ellipsoidal particle with dielectric constant ϵ_1 in a medium with dielectric constant ϵ_2 in the *quasistatic* limit, is given by: [34]

$$\epsilon_2 + L_i(\epsilon_1 - \epsilon_2) = 0 \quad (9.2)$$

and can be rewritten as

$$\omega_0 = \omega_p \sqrt{L_j} \quad \text{particle} \quad (9.3a)$$

$$\omega_0 = \omega_p \sqrt{1 - L_j} \quad \text{void} \quad (9.3b)$$

for a metal particle in air and an air void in metal, respectively. L_j is a depolarization factor that depends on the aspect ratio and the orientation of the particle, that equals $\frac{1}{3}$ for a sphere (see also Chapter 1). The depolarization factor related to the long axis of the ellipsoidal particle/void is smaller than $\frac{1}{3}$, and the longitudinal resonance frequency for a void will thus shift to the blue when compared to the spherical case. Similarly, the transverse resonance of the void cavity mode is red-shifted (L_j is larger than $\frac{1}{3}$). Both trends are observed in Fig. 9.5(a). In addition to the trends predicted in the quasistatic model, effects of size must also play a role. However, the calculations of Fig. 9.5(a) for anisotropic oblate ellipsoids at fixed volume shows that the resonance shifts are mainly determined by the anisotropy.

The optical absorption and scattering spectra of oblate ellipsoidal metal shells were also calculated using the T-matrix method. Figure 9.5(b) shows the absorption efficiency averaged over the orientation of the particle, for particles with aspect ratios ranging from 1.0 to 1.6. The resonance peak splits for spheroidal particles, with a larger shift for the peak shifting to the red than for the one shifting to the blue, as was also observed in the FDTD results in Fig. 9.5(a). Fig. 9.5(b) also shows that the total strength of the absorption feature is similar in magnitude for ellipsoidal particles as for spheres. The positions of the peaks obtained by the two methods are shown in Fig. 9.5(c) as a function of aspect ratio. The results of both methods are in good agreement and show that a large degree of wavelength tunability is achievable upon a change in aspect ratio at constant volume.

9.6 Conclusions and outlook

Au-shells with dimensions comparable to the wavelength of light exhibit cavity-related resonances that depend on the size, shape, and dielectric constant of the dielectric core inside the Au-shell. Upon plane-wave illumination, the electric field for this mode is enhanced over almost the entire volume of the core, with an enhanced intensity found in the center of the particle. The electric field enhancements at the outside edges are not studied in detail yet. The frequency of the resonance can be tuned over a large wavelength range by a proper choice of aspect ratio and polarization. The fabrication of these particles is experimentally feasible by use of ion beam techniques (see Chapter 7). Characterization of the Au-shell particles by extinction (Chapter 8), and trials to dissolve the silica cores with HF, [99] show that most of the silica cores can still be dissolved even if the particles are optically behaving as closed shells. This makes the inside of these deformed particles available for detection of signals that are enhanced by the local field.

Acknowledgements

FDTD simulations were done in collaboration with Luke Sweatlock (Caltech, Pasadena). Alexander Moroz is acknowledged for the T-matrix codes. Harry Atwater (Caltech), Femius Koenderink (FOM-AMOLF) and Sébastien Bidault (FOM-AMOLF) are acknowledged for stimulating and helpful discussions.

Applications

This Chapter sketches possible applications of the metal structures and fabrication techniques described in this thesis in photonics, sensing and medicine. These applications make use of the ability to tune the plasmon resonance frequency and the local fields in the vicinity of anisotropically-shaped metal particles.

10.1 Nanophotonics and information technology

Since the development of the light microscope in the 16th century, optical device size and performance have been limited by diffraction. Optoelectronic devices of today are much bigger than the smallest electronic devices for this reason. Achieving control of light-material interactions for photonic device applications at the nanoscale requires structures that guide electromagnetic energy with subwavelength-scale mode confinement. By converting the optical mode into non-radiating surface plasmons, electromagnetic energy can be concentrated and guided in structures with lateral dimensions of less than 10% of the free-space wavelength. For example, in the metal nanoparticle arrays, such as studied in Chapter 5 and 6, light can be guided along the array with a lateral confinement as small as 15 nm. Due to the strong coupling of the optical modes with electronic states in the metal, it has also been suggested that plasmonic interconnects could solve some of the bandwidth bottlenecks encountered in electronic circuit design. Ultimately, it may be possible to design an entire class of subwavelength-scale optoelectronic components (waveguides, sources, detectors, modulators) that could form the building blocks of an optical device technology – a technology scalable to molecular dimensions, with potential imaging, spectroscopy, and interconnection applications in computing, communications, and chemical/biological detection.

The optical cavities in Chapter 9 may serve as miniature light sources or lasers, if doped with a suitable light emitter or gain medium. The broadband scattering of these metal shell particles may also be used in photovoltaic cells to increase the effective interaction volume. The particle shape can be adjusted to match the relevant part of the solar energy spectrum. Anisotropic metal nanostructures may also find applications in optical storage, where a single bit can be stored in each particle provided that its shape can be individually controlled. Indeed, it is known that laser irradiation can change the shape of prolate ellipsoidal particles into spherical when light at the plasmon resonance is used. [170] Arrays of aligned Au rods in a dielectric matrix, such as those in Chapter 4 fabricated by MeV ion irradiation, may then be suitable candidates.

10.2 Biomedical applications

Applications of metal nanostructures to biological systems and medicine become possible if the plasmon frequency is tuned to the near-infrared, since blood and tissue are relatively

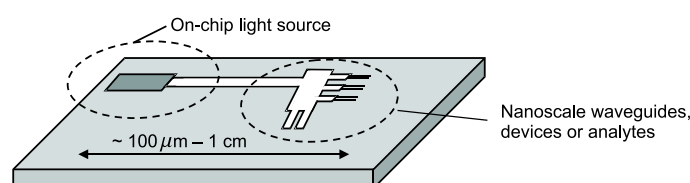


Figure 10.1: Schematic illustration of a plasmonic interconnect network that enables both chip-scale propagation and subwavelength-scale operation. Signals are transported to and from active sources and detectors and efficiently couple into and out of nanometer-scale devices or analytes.

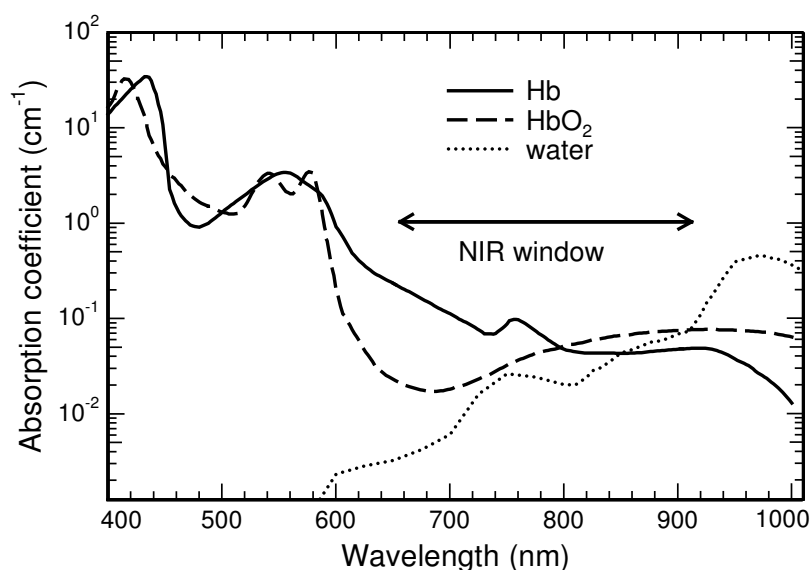


Figure 10.2: Absorption coefficient of water and (de)oxygenated hemoglobin (Hb). Absorption of light is relatively low in the near-infrared window (wavelengths between 600 and 900 nm).

transparent due to low absorption by water and hemoglobin (Fig. 10.2). The penetration depth of light in tissue at these wavelengths is more than 10 cm. As shown in this thesis, tunability of the plasmon resonance can be achieved using a core-shell structure composed of a dielectric core and a metal shell, with the size anisotropy providing additional control. Moreover, gold is stable and has a high compatibility to biological systems. Scattering of light by gold core and shell particles can be used to enhance the contrast in optical imaging techniques. By linking specific antibodies to the metal surface, tumor cells can be targeted and imaged before pathologic changes occur at the anatomic level. [29]

Metal shell colloids can also absorb light and locally generate heating. Irreversible photothermal ablation of tumor cells was recently demonstrated, providing an effective destruction of tumor cells with minimal damage to near-by healthy tissue. [171] The local photoinduced heating was also exploited for drug delivery. Metal shell particles were embedded in a temperature-sensitive polymer. Upon laser irradiation, the temperature rise caused a collapse of the polymer matrix and the molecules embedded in the voids of the polymer matrix were released. [172] The tunability of the plasmon resonance as described in this thesis can thus be used to engineer plasmonic structures for biomedical imaging, diagnosis, and treatment at the desired wavelength.

10.3 Sensing

The locally enhanced field at the surface of metal particles can be used to enhance Raman scattering or luminescence from molecules. The detection of Raman signals from a single molecule has already been demonstrated in inter-particle gaps of aggregated small silver colloids where the field intensity is maximum. [173] However, designing smart substrates where the field intensity can be optimized at a given frequency is still a technological

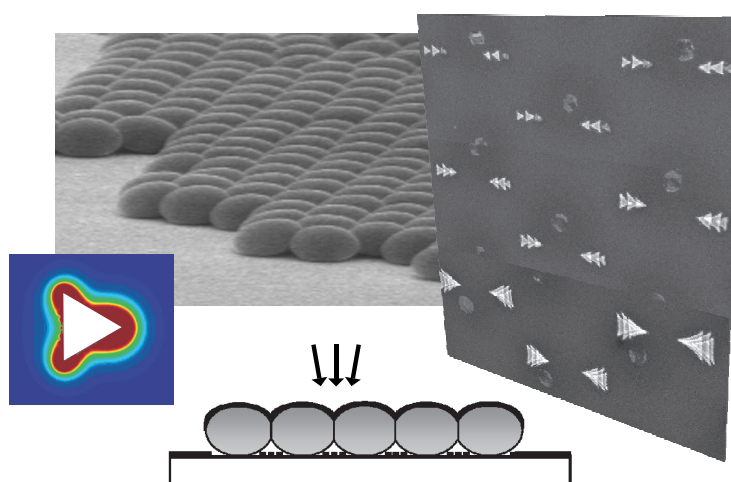


Figure 10.3: Nanosphere lithography with modified colloidal masks (Chapters 2 and 3). Colloidal masks irradiated with MeV ions reduces the size of the holes in the mask while the distance is kept constant. Arrays of metal particles can be obtained by evaporation of metal at different angles with the sample normal. The maximum enhancement of the electric field is found at the tips of the triangle (see Ref. [33]).

challenge. Both metal shell particles (also because of their surface roughness) and metal particle arrays (Chapters 5 and 9) are suitable candidates.

Core-shell colloids with cavity modes in the dielectric core, as described in Chapter 9, may lead to special applications in fluorescence enhancement due to the high field intensities located at the center of the dielectric core, far away from the metal surface, so that fluorescence quenching by coupling to the metal is minimal. [169] The inside of these particles becomes available for sensing by removing the silica core by HF etching, which is possible due to small pores in the metal shell. [99]

Another sensing scheme for detecting low concentrations of molecules or biological species exploits the dependence of the surface plasmon resonance frequency on the dielectric constant of the surrounding medium. As was shown in Part 1 of this thesis, large areas covered with hexagonal patterns of metal particles with a triangular shape can be made by using colloidal nanosphere lithography. This is a relatively simple and inexpensive method compared to conventional lithography. These metal nanoparticle arrays thus have excellent properties to be used in optical sensing of biomolecules, as the resonance wavelength will change in response to the attachment of molecules. Recent work by Haes *et al.*, for example, demonstrated the use of these structures in the diagnosis of Alzheimer's disease. [174]

Several techniques have been developed to decrease the size of the metal particles in nanosphere lithography at a constant inter-particle distance. In Chapter 2 and 3, for example, we showed that this can be achieved by use of ion irradiation and wet-chemical growth of silica on the colloidal mask. Imaging techniques like dark field scattering can then be used to detect changes in the dielectric environment on single particles. It was suggested that the sensitivity of single small metal particles could approach the single-molecule detection limit for large biomolecules. Implementation of nanoparticles with different size and shape will enable fast, simultaneous and label-free detection of different chemical and biological species. [20]

Appendix: Light scattering

General

Light scattering by particles is often best described using spherical coordinates. The particle center is located at the origin $(0,0,0)$, and in case of rotationally symmetric particles, the symmetry axis is chosen to coincide with the z -axis. The angles in the spherical coordinate system are given by θ and ϕ , in which $\theta \in [0, \pi]$ is the polar angle measured from the positive z -axis and $\phi \in [0, 2\pi)$ the azimuthal angle measured from the x -axis in the xy -plane (see Fig. 10.4).

The transverse electromagnetic plane-wave incident along the direction of $\hat{n} = \hat{\theta} \times \hat{\phi}$ on a scatterer can then be described by two components E_{\parallel} and E_{\perp} in the $\hat{\theta}$ and $\hat{\phi}$ directions, respectively. The scattered wave is an outgoing spherical wave. The scattering matrix \mathbf{S} linearly transforms the components of the incoming electric field into the components of the scattered wave: [154]

$$\begin{pmatrix} E_{\parallel} \\ E_{\perp} \end{pmatrix} = \begin{pmatrix} S_2 & S_3 \\ S_4 & S_1 \end{pmatrix} \frac{e^{ikr}}{r} \begin{pmatrix} E_{\parallel}^{in} \\ E_{\perp}^{in} \end{pmatrix} \quad (10.1)$$

The four elements of the scattering matrix, the amplitude functions S_1 , S_2 , S_3 and S_4 , are all complex functions that depend on the directions of incidence and scattering and on the particle size and morphology. For spherical particles, the off-diagonal elements S_3 and S_4 are zero, and the extinction cross section efficiency is given:

$$Q_{ext} = \frac{\lambda}{\pi R^2} \text{Im}[S_1 + S_2] \quad (10.2)$$

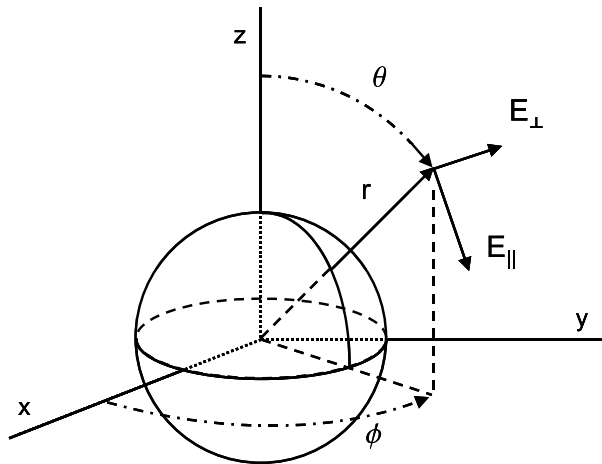


Figure 10.4: Spherical coordinate system.

Mie theory

The solution of Maxwell's equations to the problem of scattering and absorption of light by a sphere illuminated by a plane-wave was given by Gustav Mie in the beginning of the 20th century. [1] It is based on the method of separation of variables and described in many text books, see e.g., Refs. [34, 175, 176]. The differential equations can be solved separately for the parameters r , θ , and ϕ . The electric fields of the incoming and scattered waves are then expressed in a series of spherical harmonic functions. The geometry excludes some of the spherical harmonics in these series, since amplitude of the fields must be finite at the origin, and the (outgoing) scattered wave must vanish at large distances from the particle. By applying the boundary conditions that the tangential components of the fields must be continuous at the surface of the particle, the coefficients of the scattered and the internal fields can be solved as a function of the known coefficients of the incoming fields.

The exact analytical results via the method of separation of variables can only be applied to a limited number of particle geometries. [154] Besides the solution for an isotropic sphere, solutions of concentric core/shell spheres, [44] concentric multilayered spheres, infinite cylinders, homogeneous and core/shell spheroids, [177, 178] and a sphere on a surface [179] have been presented in literature.

T-matrix formalism

The T-matrix or transition matrix method was first introduced by Waterman for homogeneous particles in the late 1950s and later improved by several people. Nowadays, it is a widely used technique to calculate the optical properties of nonspherical particles. Like in the frame-work of Mie-theory, the incoming and scattered fields are expanded in vector spherical harmonics. The T-matrix is the matrix that relates the expansion coefficients of the scattered field p_{mn} and q_{mn} to the coefficients of the incoming field a_{mn} and b_{mn} :

$$\begin{pmatrix} \mathbf{p} \\ \mathbf{q} \end{pmatrix} = \begin{pmatrix} \mathbf{T}^{11} & \mathbf{T}^{12} \\ \mathbf{T}^{21} & \mathbf{T}^{22} \end{pmatrix} \begin{pmatrix} \mathbf{a} \\ \mathbf{b} \end{pmatrix} \quad (10.3)$$

From the T-matrix, the elements of the scattering matrix \mathbf{S} and other quantities can be calculated. A fundamental and convenient feature of the T-matrix is that it only depends on the size, composition and shape of the scatterer.

In a typical T-matrix calculation, the field inside the scatterer is also expanded in vector spherical harmonics, with coefficients c_{mn} and d_{mn} . These coefficients are related to the coefficients a_{mn} and b_{mn} of the incident field by the matrix \mathbf{Q} . The elements of the matrix \mathbf{Q} are 2-dimensional integrals over the surface of the particle. [180] The T-matrix method is therefore also referred to as the extended boundary condition method. The T-matrix is calculated from the matrix \mathbf{Q} by

$$\mathbf{T} = -\mathbf{Q}_2 [\mathbf{Q}]^{-1} \quad (10.4)$$

in which the matrix \mathbf{Q} is equal to \mathbf{Q}_2 , except that in the evaluation of the matrix elements the Bessel functions of the first kind have to be replaced by Hankel functions.

The formulas for T-matrix calculations become much simpler for axially symmetric particles with the rotational axis along the z-axis, because the surface integrals then reduce

to single integrals over the polar angle θ and the T matrix becomes diagonal with respect to the indices m and m' .

The T-matrix of a coated particle can be written in terms of the T-matrix \mathbf{T}_1 of a homogeneous particle with a radius equal to that of the core and a refractive index of m_1/m_2 , and the matrices \mathbf{A}_2 and \mathbf{B}_2 that form the T-matrix of a homogeneous particle of the same (total) size and refractive index m_2 by $-\mathbf{B}_2 \cdot \mathbf{A}_2^{-1}$: [155]

$$\mathbf{T} = -[\mathbf{B}_2 + \mathbf{B} \cdot \mathbf{T}_1] \cdot [\mathbf{A}_2 + \mathbf{A} \cdot \mathbf{T}_1]^{-1} \quad (10.5)$$

The matrices \mathbf{B} and \mathbf{A} are equal to the matrices \mathbf{B}_2 and \mathbf{A}_2 , except that in the evaluation of the matrix elements the Bessel functions of the first kind have to be replaced by Hankel functions.

T-matrix program

The calculations in Chapter 8 and 9 were done using a Fortran code written by Moroz, [41] based on the T-matrix codes by Mishchenko and Quirantes. The codes are available on the World Wide Web and described in several papers in the literature. [153, 155, 156, 180, 180, 181] The outcomes for spherical particles were benchmarked to results from Mie-theory calculations. Results for anisotropic particles were compared to analytical results for oblate spheroids from Asano [34, 178] (using the method of separation of variables) and results published by Kelly *et al.* [33]

Convergence

For computations, the expansion of the electromagnetic fields is cut-off after a finite number N_{max} . The convergence of the extinction and scattering cross sections is checked by a subroutine. [156] When convergence is not obtained within a certain accuracy, N_{max} is increased. An increase in N_{max} results in larger computer usage (it also determines the size of the submatrices T^{ij}), and can result in computational instability. For a coated particle, the convergence of the T-matrices in equation 10.5 require different N_{max} to converge. In the calculations, the largest of the value of N_{max} required to obtain convergence is used. The routine also checks for the convergence of the surface integrals, which is determined by the number of Gaussian integration points. In literature, a rule of thumb for coated particles is that this number should be about $4 N_{max}$. [155] In our calculations, the number of Gaussian integration points was set to $6 N_{max}$.

For larger particles and/or larger anisotropy, it is well known that computation of the T-matrix can be an ill-conditioned process. Due to the large numbers in the \mathbf{Q} -matrix,

Table 10.1: Convergence parameter N_{max} as a function of size anisotropy for an oblate ellipsoidal silica-core/Au-shell particle in silica with sphere-equivalent-dimensions of $R_{core} = 156$ nm and $R_{total} = 181$ nm (system A) and $R_{core} = 228$ nm and $R_{total} = 266$ nm (system B).

System	Aspect ratio	1.0	1.1	1.2	1.3	1.4	1.5	1.6	1.7
1	N_{max}	8	10	12	14	16	18	20	20
2	N_{max}	12	14	14	18	20	26	28	-

the matrix inversion involved in the computation of the T-matrix (see Equations 10.3 and 10.5) can become numerically unstable. Therefore, especially for a-spherical particles, special attention has to be paid to the convergence of the calculation.

For spherical Au-shell particles of about the size in the experiments reported here, convergence is obtained at typical values of 7–13 for N_{max} in the wavelength ranging from 1900 nm to 300 nm. Table 10.1 shows the increase in the convergence parameter N_{max} for the calculations for oblate ellipsoidal Au-shells as the particle anisotropy is increased for the systems studied in Chapters 8 (system A) and 9 (system B).

References

- [1] G. Mie, *Beiträge zur Optik trüber Medien, speziell kolloidaler Metallösungen*, Ann. Phys. **25**, 377 (1908).
- [2] M. C. Daniel and D. Astruc, *Gold nanoparticles: assembly, supramolecular chemistry, quantum-size-related properties, and applications toward biology, catalysis and nanotechnology*, Chem. Rev. **104**, 293 (2004).
- [3] B. Wiley, Y. Sun, J. Chen, H. Cang, Z.-Y. Li, X. Li, and Y. Xia, *Shape-controlled synthesis of silver and gold nanostructures*, MRS Bull. **30**, 356 (2005).
- [4] W. L. Barnes, A. Dereux, and T. W. Ebbesen, *Surface plasmon subwavelength optics*, Nature **424**, 824 (2003).
- [5] T. W. Ebbesen, H. J. Lezec, H. F. Ghaemi, T. Thio, and P. A. Wolff, *Extraordinary optical transmission through sub-wavelength hole arrays*, Nature **391**, 667 (1998).
- [6] J. Dintinger, A. Degiron, and T. W. Ebbesen, *Enhanced light transmission through sub-wavelength holes*, MRS Bull. **30**, 381 (2005).
- [7] L. Yin, V. K. Vlasko-Vlasov, J. Pearson, J. M. Hiller, J. Hua, U. Welp, D. E. Brown, and C. W. Kimball, *Subwavelength focussing and guiding of surface plasmons*, Nano Lett. **5**, 1399 (2005).
- [8] N. Fang, H. Lee, C. Sun, and X. Zhang, *Sub-diffraction limited optical imaging with a silver superlens*, Science **308**, 534 (2005).
- [9] E. Ozbay, *Plasmonics: merging photonics and electronics at nanoscale dimensions*, Science **311**, 189 (2006).
- [10] J. A. Dionne, L. A. Sweatlock, H. A. Atwater, and A. Polman, *Planar metal plasmon waveguides: frequency-dependent dispersion, propagation, localization and loss beyond the free electron model*, Phys. Rev. B **72**, 075405 (2005).
- [11] H. A. Atwater, S. A. Maier, A. Polman, J. A. Dionne, and L. A. Sweatlock, *The new “p-n junction”: plasmonics enables photonic access to the nanoworld*, MRS Bull. **30**, 385 (2005).
- [12] T. Nikolajsen, K. Leosson, I. Salakhutdinov, and S. I. Bozhnevolnyi, *Polymer-based surface-plasmon-polariton stripe waveguides at telecommunication wavelengths*, Appl. Phys. Lett. **82**, 668 (2003).
- [13] J. C. Weeber, J. R. Krenn, A. Dereux, B. Lamprecht, Y. Lacroute, and J. P. Goudonnet, *Near-field observation of surface plasmon polariton propagation on thin metal stripes*, Phys. Rev. B **64**, 045411 (2001).
- [14] M. Quinten, A. Leitner, J. R. Krenn, and F. R. Aussenegg, *Electromagnetic energy transport via linear chains of silver nanoparticles*, Opt. Lett. **23**, 1331 (1998).
- [15] M. L. Brongersma, J. W. Hartman, and H. A. Atwater, *Electromagnetic energy transfer and switching in nanoparticle chain arrays below the diffraction limit*, Phys. Rev. B **62**, R16356 (2000).
- [16] A. F. Koenderink and A. Polman, *Complex response and polariton-like dispersion splitting in periodic metal nanoparticle chains*, Phys. Rev. B (2006), in press.

- [17] S. A. Maier, P. G. Kik, H. A. Atwater, S. Meltzer, E. Harel, B. E. Koel, and A. A. G. Requicha, *Local detection of electromagnetic energy transport below the diffraction limit in metal nanoparticle plasmon waveguides*, Nat. Mater. **2**, 229 (2003).
- [18] F. J. García-Vidal and J. B. Pendry, *Collective theory for surface enhanced Raman scattering*, Phys. Rev. Lett. **77**, 1163 (1996).
- [19] H. Xu, J. Aizpurua, M. Käll, and P. Apell, *Electromagnetic contributions to single-molecule sensitivity in surface-enhanced Raman scattering*, Phys. Rev. E **62**, 4318 (2000).
- [20] A. D. McFarland and R. P. Van Duyne, *Single silver nanoparticles as real-time optical sensors with zeptomole sensitivity*, Nano Lett. **3**, 1057 (2003).
- [21] A. V. Whitney, J. W. Elam, S. Zou, A. V. Zinovev, P. C. Stair, G. C. Schatz, and R. P. van Duyne, *Localize surface plasmon resonance nanosensor: a high-resolution distance-dependence study using atomic layer deposition*, J. Phys. Chem. B **109**, 20522 (2005).
- [22] H. Xu, E. J. Bjerneld, M. Käll, and L. Börjesson, *Spectroscopy of single hemoglobin molecules by surface enhanced Raman scattering*, Phys. Rev. Lett. **83**, 4357 (1999).
- [23] Y. Hamanaka, K. Fukata, A. Nakamura, L. M. Liz-Marzán, and P. Mulvaney, *Enhancement of third-order nonlinear optical susceptibilities in silica-capped Au nanoparticle films with very high concentrations*, Appl. Phys. Lett. **84**, 4938 (2004).
- [24] A. Hohenau, J. R. Krenn, J. Beerman, S. I. Bozhnevolnyi, S. G. Rodrigo, L. Martin-Moreno, and F. Garcia-Vidal, *Spectroscopy and nonlinear microscopy of Au nanoparticle arrays: experiment and theory*, Phys. Rev. B **73**, 155404 (2006).
- [25] Y. Yang, M. Nogami, J. Shi, H. Chen, G. Ma, and S. Tang, *Controlled surface-plasmon coupling in SiO₂-coated gold nanochains for tunable nonlinear optical properties*, Appl. Phys. Lett. **88**, 081110 (2006).
- [26] P. Alivisatos, *The use of nanocrystals in biological detection*, Nat. Biotechnol. **22**, 47 (2004).
- [27] S. Schultz, D. R. Smith, J. J. Mock, and D. A. Schultz, *Single-target molecule detection with nonbleaching multicolor optical immunolabels*, Proc. Nat. Acad. Sci. **97**, 996 (2000).
- [28] J. G. Fujimoto, *Optical coherence tomography for ultrahigh resolution in vivo imaging*, Nat. Biotechnol. **21**, 1361 (2003).
- [29] L. R. Hirsch, A. M. Gobin, A. R. Lowery, F. Tam, R. A. Drezek, N. J. Halas, and J. L. West, *Metal nanoshells*, Ann. of Biomed. Eng. **34**, 15 (2006).
- [30] J. Chen, F. Saeki, B. J. Wiley, H. Chang, M. J. Cobb, Z. Y. Li, L. Au, H. Zhang, M. B. Kimmey, X. Li, and Y. Xia, *Gold nanocages: bioconjugation and their potential use as optical imaging contrast agents*, Nano Lett. **5**, 473 (2005).
- [31] R. Weissleder, *A clearer vision for in vivo imaging*, Nat. Biotechnol. **19**, 316 (2001).
- [32] R. Jin, Y. Cao, C. A. Mirkin, K. L. Kelly, G. C. Schatz, and J. G. Zheng, *Photoinduced conversion of silver nanospheres to nanoprisms*, Science **294**, 1901 (2001).
- [33] K. L. Kelly, E. Coronado, L. L. Zhao, and G. C. Schatz, *The optical properties of metal nanoparticles: the influence of size, shape, and dielectric environment*, J. Phys. Chem. B **107**, 668 (2003).
- [34] C. F. Bohren and D. R. Huffman, *Absorption and scattering of light by small particles*, Wiley, New York, 1983.
- [35] E. D. Palik, *Handbook of optical constants of solids*, Academic Press, New York, 1985.
- [36] P. B. Johnson and R. W. Christy, *Optical constants of the noble metals*, Phys. Rev. B **6**, 4370 (1972).
- [37] U. Kreibig and M. Vollmer, *Optical properties of metal clusters*, Springer, Berlin, 1995.
- [38] E. A. Coronado and G. C. Schatz, *Surface plasmon broadening for arbitrary shape nanoparticles: a geometrical probability approach*, J. Chem. Phys. **119**, 3926 (2003).

- [39] C. L. Nehl, N. K. Grady, G. P. Goodrich, F. Tam, N. J. Halas, and J. H. Hafner, *Scattering spectra of single gold nanoshells*, Nano Lett. **4**, 2355 (2004).
- [40] P. Stoller, V. Jacobsen, and V. Sandoghdar, *Measurement of the complex dielectric constant of a single gold nanoparticle*, ArXiv/cond-mat/0604174 (2006).
- [41] A. Moroz, *Improvement of Mishchenko's T-matrix code for absorbing particles*, Appl. Opt. **44**, 3604 (2005).
- [42] J. M. Gérardy and M. Ausloos, *Absorption spectrum of clusters of spheres from the general solution of Maxwell's equations. II Optical properties of aggregated metal spheres*, Phys. Rev. B **25**, 4204 (1982).
- [43] M. Quinten and U. Kreibig, *Absorption and elastic scattering of light by particle aggregates*, Appl. Opt. **32**, 6173 (1993).
- [44] A. L. Aden and M. Kerker, *Scattering of electromagnetic waves from two concentric spheres*, J. Appl. Phys. **22**, 1242 (1951).
- [45] E. Prodan, C. Radloff, N. J. Halas, and P. Nordlander, *A hybridization model for the plasmon response of complex nanostructures*, Science **302**, 419 (2003).
- [46] E. Prodan and P. Nordlander, *Plasmon hybridization in spherical nanoparticles*, J. Chem. Phys. **120**, 5444 (2004).
- [47] J. F. Ziegler, J. P. Biersack, and U. Littmark, *The stopping and range of ions in solids*, Pergamon Press, New York, 1985.
- [48] S. Klaumünzer, *Dramatic growth of glassy Pd₈₀Si₂₀ during heavy-ion irradiation*, Phys. Rev. Lett. **51**, 1987 (1983).
- [49] M. Hou, S. Klaumünzer, and G. Schumacher, *Dimensional changes of metallic glasses during bombardment with fast heavy ions*, Phys. Rev. B **41**, 1144 (1990).
- [50] S. Klaumünzer, *Ion tracks in quartz and vitreous silica*, Nucl. Instr. Meth. B **225**, 136 (2004).
- [51] A. Audouard, E. Balanzat, S. Bouffard, J. C. Jousset, A. Chamberod, A. Dunlop, D. Lesueur, G. Fuchs, R. Spohr, J. Vetter, and L. Thomé, *Structural modifications of crystalline and amorphous Ni₃B irradiated with high-energy heavy ions*, Nucl. Instr. Meth. B **59-60**, 414 (1991).
- [52] E. Snoeks, T. Weber, A. Cacciato, and A. Polman, *MeV ion irradiation-induced creation and relaxation of mechanical stress in silica*, J. Appl. Phys. **78**, 4723 (1995).
- [53] T. van Dillen, A. Polman, C. M. van Kats, and A. van Blaaderen, *Ion beam-induced anisotropic plastic deformation at 300 keV*, Appl. Phys. Lett. **83**, 4315 (2003).
- [54] T. van Dillen, M. J. A. de Dood, J. J. Penninkhof, A. Polman, S. Roorda, and A. M. Vredenberg, *Ion beam-induced anisotropic plastic deformation of silicon microstructures*, Appl. Phys. Lett. **84**, 3591 (2004).
- [55] T. van Dillen, E. Snoeks, W. Fukarek, C. M. van Kats, K. P. Velikov, A. van Blaaderen, and A. Polman, *Anisotropic deformation of colloidal particles under MeV ion irradiation*, Nucl. Instr. Meth. B **175-177**, 350 (2001).
- [56] H. Trinkaus and A. I. Ryazanov, *Viscoelastic model for the plastic flow of amorphous solids under energetic ion bombardment*, Phys. Rev. Lett. **74**, 5072 (1995).
- [57] T. van Dillen, A. Polman, P. R. Onck, and E. van der Giessen, *Anisotropic plastic deformation by viscous flow in ion tracks*, Phys. Rev. B **71**, 024103 (2005).
- [58] E. Snoeks, A. van Blaaderen, T. van Dillen, C. M. van Kats, M. L. Brongersma, and A. Polman, *Colloidal ellipsoids with continuously variable shape*, Adv. Mater. **12**, 1511 (2000).
- [59] A. N. Shipway, E. Katz, and I. Willner, *Nanoparticle arrays on surfaces for electronic, optical, and sensor applications*, Chem. Phys. Chem. **1**, 18 (2000).

- [60] A. L. Rogach, D. V. Talapin, E. V. Shevchenko, A. Kornowski, M. Haase, and H. Weller, *Organization of matter on different size scales: monodisperse nanocrystals and their superstructures*, *Adv. Func. Mater.* **12**, 653 (2002).
- [61] F. X. Redl, K. S. Cho, C. B. Murray, and S. O'Brien, *Three-dimensional binary superlattices of magnetic nanocrystals and semiconductor quantum dots*, *Nature* **423**, 968 (2003).
- [62] R. D. Schaller, M. A. Petruska, and V. I. Klimov, *Tunable near-infrared optical gain and amplified spontaneous emission using PbSe nanocrystals*, *J. Phys. Chem. B* **107**, 13765 (2003).
- [63] U. C. Fischer and H. P. Zingsheim, *Submicroscopic pattern replication with visible light*, *J. Vac. Sci. Technol.* **19**, 881 (1981).
- [64] H. W. Deckman and J. H. Dunsmuir, *Natural lithography*, *Appl. Phys. Lett.* **41**, 377 (1982).
- [65] J. C. Hulteen and R. P. Van Duyne, *Nanosphere lithography: a materials general fabrication process for periodic particle array surfaces*, *J. Vac. Sci. Technol. A* **13**, 1553 (1995).
- [66] F. Burmeister, C. Schafle, T. Matthes, M. Bohmisch, J. Boneberg, and P. Leiderer, *Colloid monolayers as versatile lithographic masks*, *Langmuir* **13**, 2983 (1997).
- [67] C. L. Haynes and R. P. Van Duyne, *Nanosphere lithography: A versatile nanofabrication tool for studies of size-dependent nanoparticle optics*, *J. Phys. Chem. B* **105**, 5599 (2001).
- [68] M. D. Malinsky, K. L. Kelly, G. C. Schatz, and R. P. Van Duyne, *Chain length dependence and sensing capabilities of the localized surface plasmon resonance of silver nanoparticles chemically modified with alkanethiol self-assembled monolayers*, *J. Am. Chem. Soc.* **123**, 1471 (2001).
- [69] Z. P. Huang, D. L. Carnahan, J. Rybczynski, M. Giersig, M. Sennett, D. Z. Wang, J. G. Wen, K. Kempa, and Z. F. Ren, *Growth of large periodic arrays of carbon nanotubes*, *Appl. Phys. Lett.* **82**, 460 (2003).
- [70] X. Wang, C. J. Summers, and Z. L. Wang, *Large-scale hexagonal-patterned growth of aligned ZnO nanorods for nano-optoelectronics and nanosensor arrays*, *Nano Lett.* **4**, 423 (2004).
- [71] R. Michel, L. Reviakine, D. Sutherland, C. Fokas, G. Csucs, G. Danuser, N. D. Spencer, and M. Textor, *A novel approach to produce biologically relevant chemical patterns at the nanometer scale: selective molecular assembly patterning combined with colloidal lithography*, *Langmuir* **18**, 8580 (2002).
- [72] A. Kosiorek, W. Kandulski, P. Chudzinski, K. Kempa, and M. Giersig, *Shadow nanosphere lithography: simulation and experiment*, *Nano Lett.* **4**, 1359 (2004).
- [73] S. M. Yang, S. G. Jang, D. G. Choi, S. Kim, and H. K. Yu, *Nanomachining by colloidal lithography*, *Small* **2**, 458 (2006).
- [74] J. P. Hoogenboom, D. L. J. Vossen, C. Faivre-Moskalenko, M. Dogterom, and A. van Blaaderen, *Patterning surfaces with colloidal particles using optical tweezers*, *Appl. Phys. Lett.* **80**, 4828 (2002).
- [75] D. L. J. Vossen, J. P. Hoogenboom, K. Overgaag, and A. van Blaaderen, *Building two and three-dimensional structures of colloidal particles on surfaces using optical tweezers and critical point drying*, *Mat. Res. Soc. Symp. Proc.* **705**, Y6.8.1 (2002).
- [76] A. van Blaaderen and A. Vrij, *Synthesis and characterization of colloidal dispersions of fluorescent, monodisperse silica spheres*, *Langmuir* **8**, 2921 (1992).
- [77] A. van Blaaderen, J. van Geest, and A. Vrij, *Monodisperse colloidal silica spheres from tetraalkoxysilanes - Particle formation and growth-mechanism*, *J. of Colloid and Interf. Science* **154**, 481 (1992).
- [78] H. Giesche, *Synthesis of monodispersed silica powders II. Controlled growth reaction and continuous production process*, *J. of the European Ceramic Society* **14**, 205 (1994).

- [79] D. L. J. Vossen, A. van der Horst, M. Dogterom, and A. van Blaaderen, *Optical tweezers and confocal microscopy for simultaneous three-dimensional manipulation and imaging in concentrated colloidal dispersions*, Rev. of Scient. Instr. **75**, 2960 (2004).
- [80] A. van Blaaderen, J. P. Hoogenboom, D. L. J. Vossen, A. Yethiraj, A. van der Horst, K. Visscher, and M. Dogterom, *Colloidal epitaxy: playing with the boundary conditions of colloidal crystallization*, Faraday Discuss. **123**, 107 (2003).
- [81] K. J. Vahala, *Optical microcavities*, Nature **424**, 839 (2003).
- [82] F. Burmeister, W. Badowsky, T. Braun, S. Wieprich, J. Boneberg, and P. Leiderer, *Colloid monolayer lithography-A flexible approach for nanostructuring of surfaces.*, Appl. Surf. Sci. **144-145**, 461 (1999).
- [83] D. L. J. Vossen, D. Fific, J. J. Penninkhof, T. van Dillen, A. Polman, and A. van Blaaderen, *Combined optical tweezers / ion beam technique to tune colloidal masks for nanolithography*, Nano Lett. **5**, 1175 (2005), Chapter 2 of this thesis.
- [84] A. Kosiorok, W. Kandulski, H. Glaczynska, and M. Giersig, *Fabrication of nanoscale rings, dots and rods by combining shadow nanosphere lithography and annealed polystyrene nanosphere masks*, Small **1**, 439 (2005).
- [85] W. Stöber, A. Fink, and E. J. Bohn, *Controlled growth of monodisperse silica spheres in the micron size range*, J. of Colloid and Interf. Science **26**, 62 (1968).
- [86] D. L. J. Vossen, M. J. A. de Dood, T. van Dillen, E. van der Drift, A. Polman, and A. van Blaaderen, *Novel method for solution growth of thin silica films from tetraethoxysilane*, Adv. Mater. **12**, 1434 (2000).
- [87] S. L. Chen, P. Dong, and G. H. Yang, *The size dependence of growth rate of monodisperse silica particles from tetraalkoxysilane*, J. of Colloid and Interf. Science **189**, 268 (1997).
- [88] C. Graf, D. L. J. Vossen, A. Imhof, and A. van Blaaderen, *A general method to coat colloidal particles with silica*, Langmuir **19**, 6693 (2003).
- [89] J. C. Hulst, D. A. Treichel, M. T. Smith, M. L. Duval, T. R. Jensen, and R. P. Van Duyne, *Nanosphere lithography: size-tunable silver nanoparticle and surface cluster arrays*, J. Phys. Chem. B **103**, 3854 (1999).
- [90] K. P. Velikov, C. G. Christova, R. P. A. Dullens, and A. van Blaaderen, *Layer-by-layer growth of binary colloidal crystals*, Science **296**, 106 (2002).
- [91] V. Kitaev and G. A. Ozin, *Self-assembled surface patterns of binary colloidal crystals*, Adv. Mater. **15**, 75 (2003).
- [92] S. Klaumünzer, *Ion hammering of silica colloids*, Nucl. Instr. Meth. B **215**, 345 (2004).
- [93] K. P. Velikov, T. van Dillen, A. Polman, and A. van Blaaderen, *Photonic crystals of shape-anisotropic colloidal particles*, Appl. Phys. Lett. **81**, 838 (2002).
- [94] Z. G. Wang, C. Dufour, E. Paumier, and M. Toulemonde, *The S_e sensitivity of metals under swift-heavy-ion irradiation - a transient thermal process*, J. Phys.: Condens. Matter **6**, 6733 (1994).
- [95] C. D'Orléans, J. P. Stoquert, C. Estournès, C. Cerruti, J. J. Grob, J. L. Guille, F. Haas, D. Muller, and M. Richard-Plouet, *Anisotropy of Co nanoparticles induced by swift heavy ions*, Phys. Rev. B **67**, 220101 (2003).
- [96] C. D'Orléans, C. Cerruti, C. Estournès, J. J. Grob, J. L. Guille, F. Haas, D. Muller, M. Richard-Plouet, and J. P. Stoquert, *Irradiations of implanted Co nanoparticles in silica layers*, Nucl. Instr. Meth. B **209**, 316 (2003).
- [97] C. D'Orléans, J. P. Stoquert, C. Estournès, J. J. Grob, D. Muller, J. L. Guille, M. Richard-Plouet, C. Cerruti, and F. Haas, *Elongated Co nanoparticles induced by swift heavy ion irradiations*, Nucl. Instr. Meth. B **216**, 372 (2004).

- [98] C. D'Orléans, J. P. Stoquert, C. Estournès, J. J. Grob, D. Muller, C. Cerruti, and F. Haas, *Deformation yield of Co nanoparticles in SiO₂ irradiated with 200 MeV ¹²⁷I ions*, Nucl. Instr. Meth. B **225**, 156 (2004).
- [99] C. Graf and A. van Blaaderen, *Metallo-dielectric colloidal core-shell particles for photonic applications*, Langmuir **18**, 524 (2002).
- [100] A. Benyagoub and S. Klaumünzer, *Swift heavy-ion-induced plastic deformation*, Radiat. Eff. Def. Sol. **126**, 105 (1993).
- [101] S. Roorda, T. van Dillen, A. Polman, C. Graf, A. van Blaaderen, and B. J. Kooi, *Aligned gold nanorods in silica made by ion irradiation of core-shell colloidal particles*, Adv. Mater. **16**, 235 (2004).
- [102] M. Strobel, K. H. Heinig, and W. Möller, *Three-dimensional domain growth on the size scale of the capillary length: effective growth exponent and comparative atomistic and mean-field simulations.*, Phys. Rev. B **64**, 245422 (2001).
- [103] E. Valentin, H. Bernas, C. Ricolleau, and F. Creuzet, *Ion-beam "photography": decoupling nucleation and growth of metal clusters in glass*, Phys. Rev. Lett. **86**, 99 (2001).
- [104] A. M. Vredenberg *et al.*, unpublished.
- [105] D. P. Peeters, C. Strohhofer, M. L. Brongersma, J. van der Elsken, and A. Polman, *Formation mechanism of silver nanocrystals made by ion irradiation of Na⁺ ↔ Ag⁺ ion-exchanged sodalime silicate glass*, Nucl. Instr. Meth. B **168**, 237 (2000).
- [106] F. Caccavale, G. D. Marchi, F. Gonella, P. Mazzoldi, C. Meneghini, A. Quaranta, G. W. Arnold, G. Battaglin, and G. Mattei, *Irradiation-induced Ag-colloid formation in ion-exchanged soda-lime glass*, Nucl. Instr. Meth. B **96**, 382 (1995).
- [107] M. L. Brongersma, E. Snoeks, T. van Dillen, and A. Polman, *Origin of MeV ion irradiation-induced stress changes in SiO₂*, J. Appl. Phys. **88**, 59 (2000).
- [108] L. A. Sweatlock, S. A. Maier, H. A. Atwater, J. J. Penninkhof, and A. Polman, *Highly confined electromagnetic fields in arrays of strongly coupled Ag nanoparticles*, Phys. Rev. B **71**, 235408 (2005), Chapter 6 of this thesis.
- [109] R. W. Ditchburn, *Light*, Dover, 1961.
- [110] B. E. Saleh and M. C. Teich, *Fundamentals of photonics*, Wiley, New York, 1991.
- [111] D. Sarid, *Long-range surface-plasma waves on very thin metal films*, Phys. Rev. Lett. **47**, 1927 (1981).
- [112] A. E. Craig, G. A. Oldon, and D. Sarid, *Experimental observation of the long-range surface plasmon polariton*, Opt. Lett. **8**, 380 (1983).
- [113] P. Berini, *Plasmon-polariton waves guided by thin lossy metal films of finite width: bound modes of symmetric structures*, Phys. Rev. B **61**, 10484 (2000).
- [114] P. Berini, *Plasmon-polariton waves guided by thin lossy metal films of finite width: bound modes of asymmetric structures*, Phys. Rev. B **63**, 125417 (2001).
- [115] R. Charbonneau, P. Berini, E. Berolo, and E. Lisicka-Shrzek, *Experimental observation of plasmon polariton waves supported by a thin metal film of finite width*, Opt. Lett. **25**, 844 (2000).
- [116] J. R. Krenn, B. Lamprecht, H. Ditlbacher, G. Schider, M. Salerno, A. Leitner, and F. R. Aussenegg, *Non-diffraction-limited light transport by gold nanowires*, Europhys. Lett **60**, 663 (2002).
- [117] D. A. Genov, A. K. Sarychev, V. M. Shalaev, and A. Wei, *Resonant field enhancements from metal particle arrays*, Nano Lett. **4**, 153 (2004).
- [118] F. Hache, D. Ricard, and C. Flytzanis, *Optical nonlinearities of small metal particles: surface-mediated resonance and quantum size effects*, J. Opt. Soc. Am. B **3**, 1647 (1986).

- [119] R. J. Gehr and R. W. Boyd, *Optical properties of nanostructured optical materials*, Chem. Mater. **8**, 1807 (1996).
- [120] Y. Shen and P. N. Prasad, *Nanophotonics: a new multidisciplinary frontier*, Appl. Phys. B: Lasers Opt. **74**, 641 (2002).
- [121] D. Prot, D. B. Stout, J. Lafait, N. Pinçon, B. Palpant, and S. Debrus, *Local electric field enhancements and large third-order optical nonlinearity in nanocomposite materials*, J. Opt. A, Pure Appl. Opt. **4**, S99 (2002).
- [122] S. A. Maier, P. G. Kik, and H. A. Atwater, *Optical pulse propagation in metal nanoparticle chain waveguides*, Phys. Rev. B **67**, 205402 (2003).
- [123] J. J. Penninkhof, A. Polman, L. A. Sweatlock, S. A. Maier, H. A. Atwater, A. M. Vredenberg, and B. J. Kooi, *Mega-electron-volt ion beam induced anisotropic plasmon resonance of silver nanocrystals in glass*, Appl. Phys. Lett. **83**, 4137 (2003), Chapter 5 of this thesis.
- [124] M. Kaempfe, H. Graener, A. Kiesow, and A. Heilmann, *Formation of metal particle nanowires induced by ultrashort laser pulses*, Appl. Phys. Lett. **79**, 1876 (2001).
- [125] R. A. McMillan, C. D. Paavola, J. Howard, S. L. Chan, N. J. Zaluzec, and J. D. Trent, *Ordered nanoparticle arrays formed on engineered chaperonin protein templates*, Nat. Mater. **1**, 247 (2002).
- [126] H. Mertens and A. Polman, *Depth-resolved nanostructure and refractive index of borosilicate glass doped with Ag nanocrystals*, Optical Materials, in press (2006).
- [127] Q.-H. Wei, K.-H. Su, S. Durant, and X. Zhang, *Plasmon resonance of finite one-dimensional Au nanoparticle chains*, Nano Lett. **4**, 1067 (2004).
- [128] J. R. Krenn, A. Dereux, J. C. Weeber, E. Bourillot, Y. Lacroute, J. P. Goudonnet, G. Schider, W. Gotschy, A. Leitner, F. R. Aussenegg, and C. Girard, *Squeezing the optical near-field zone by plasmon coupling of metallic nanoparticles*, Phys. Rev. Lett. **82**, 2590 (1999).
- [129] S. Y. Park and D. Stroud, *Surface-plasmon dispersion relations in chains of metallic nanoparticles: an exact quasistatic calculation*, Phys. Rev. B **69**, 125418 (2004).
- [130] S. A. Maier, P. G. Kik, and H. A. Atwater, *Observation of coupled plasmon-polariton modes in Au nanoparticle chain waveguides of different lengths: estimation and waveguide loss*, Appl. Phys. Lett. **81**, 1714 (2002).
- [131] *Maxwell's equations by Finite Integration Algorithm (MaFIA)*, CST, Darmstadt, Germany, Software, 4th edition, version 4.106.
- [132] J. P. Kottmann and O. J. F. Martin, *Plasmon resonant coupling in metallic nanowires*, Opt. Express **8**, 655 (2001).
- [133] P. Nordlander, C. Oubre, E. Prodan, K. Li, and M. I. Stockman, *Plasmon hybridization in nanoparticle dimers*, Nano Lett. **4**, 899 (2004).
- [134] T. Atay, J.-H. Song, and A. V. Nurmikko, *Strongly interacting plasmon nanoparticle pairs: from dipole-dipole interaction to conductively coupled regime*, Nano Lett. **4**, 1627 (2004).
- [135] S. J. Oldenburg, R. D. Averitt, S. L. Westcott, and N. J. Halas, *Nanoengineering of optical resonances*, Chem. Phys. Lett. **288**, 243 (1998).
- [136] A. E. Neeves and M. H. Birnboim, *Composite structures for the enhancement of non-linear susceptibility*, J. Opt. Soc. Am. B **6**, 787 (1989).
- [137] S. J. Limmer, T. P. Chou, and G. Cao, *Formation and optical properties of cylindrical gold nanoshells on silica and titania nanorods*, J. Phys. Chem. B **107**, 13313 (2003).
- [138] H. Wang, D. W. Brandl, F. Le, P. Nordlander, and N. J. Halas, *Nanorice: a hybrid plasmonic nanostructure*, Nano Lett. **6**, 827 (2006).
- [139] E. Snoeks, A. van Blaaderen, T. van Dillen, C. M. van Kats, K. P. Velikov, M. Brongersma, and A. Polman, *Colloidal assemblies modified by ion irradiation*, Nucl. Instr. Meth. B **178**, 62 (2001).

- [140] T. van Dillen, A. Polman, W. Fukarek, and A. van Blaaderen, *Energy-dependent anisotropic deformation of colloidal silica particles under MeV Au irradiation*, Appl. Phys. Lett. **78**, 910 (2001).
- [141] C. Graf *et al.*, unpublished.
- [142] Y. N. Yavlinskii, *Track formation in amorphous metals under swift heavy ion bombardment*, Nucl. Instr. Meth. B **146**, 142 (1998).
- [143] C. Radloff and N. J. Halas, *Enhanced thermal stability of silica-encapsulated metal nanoshells*, Appl. Phys. Lett. **79**, 674 (2001).
- [144] C. A. Volkert and A. Polman, *Radiation-enhanced plastic flow of covalent materials during ion irradiation*, Mat. Res. Soc. Symp. Proc. **235**, 3 (1992).
- [145] E. Snoeks, K. S. Boutros, and J. Barone, *Stress relaxation in tungsten films by ion irradiation*, Appl. Phys. Lett. **71**, 267 (1997).
- [146] A. Benyagoub, S. Klaumünzer, T. Thomé, J. C. Dran, F. Garrido, and A. Dunlop, *Ion-beam induced plastic deformation in amorphous materials investigated by marker implantation and RBS*, Nucl. Instr. Meth. B **64**, 684 (1992).
- [147] F. Garrido, A. Benyagoub, A. Chamberod, J. C. Dran, A. Dunlop, S. Klaumünzer, and L. Thomé, *Giant deformation of solids irradiated with swift heavy ions: behaviour of amorphous/crystalline multilayers*, Nucl. Instr. Meth. B **115**, 430 (1996).
- [148] T. van Dillen, P. R. Onck, E. van der Giessen, and A. Polman, unpublished.
- [149] S. A. Maier and H. A. Atwater, *Plasmonics: Localization and guiding of electromagnetic energy in metal/dielectric structures*, J. Appl. Phys. **98**, 011101 (2005).
- [150] L. Gunnarsson, T. Rindzevicius, J. Prikulis, B. Kasemo, M. Käll, S. Zou, and G. C. Schatz, *Confined plasmons in nanofabricated single silver particle pairs: experimental observations of strong interparticle interactions*, J. Phys. Chem. B **109**, 1079 (2005).
- [151] J. J. Penninkhof, C. Graf, T. van Dillen, A. M. Vredenberg, A. van Blaaderen, and A. Polman, *Angle-dependent extinction of anisotropic silica/Au core/shell colloids made via ion irradiation*, Adv. Mater. **17**, 1484 (2005), Chapter 7 of this thesis.
- [152] G. Decher, *Fuzzy nanoassemblies: toward layered polymeric multicomposites*, Science **277**, 1232 (1997).
- [153] M. I. Mishchenko, *Calculation of the amplitude matrix for a non-spherical particle in a fixed orientation*, Appl. Opt. **39**, 1026 (2000).
- [154] M. I. Mishchenko, L. D. Travis, and A. A. Lacis, *Scattering, absorption, and emission of light by small particles*, Cambridge University Press, Cambridge, 2002.
- [155] A. Quirantes, *Light scattering properties of spheroidal coated particles in random orientation*, J. Quant. Spectrosc. Radiat. Transfer **63**, 263 (1999).
- [156] A. Quirantes, *A T-matrix method and computer code for randomly oriented, axially symmetric coated scatterers*, J. Quant. Spectrosc. Radiat. Transfer **92**, 373 (2005).
- [157] J. Gersten and A. Nitzan, *Electromagnetic theory of enhanced Raman scattering by molecules adsorbed on rough surfaces*, J. Chem. Phys. **73**, 3023 (1980).
- [158] M. Moskovits, *Surface enhanced spectroscopy*, Rev. Mod. Phys. **57**, 783 (1985).
- [159] J. B. Jackson and N. J. Halas, *Surface-enhanced Raman scattering on tunable plasmonic nanoparticle substrates*, Proc. Nat. Acad. Sci. **101**, 17930 (2004).
- [160] A. Parfenov, I. Gryczynski, J. Malicka, C. D. Geddes, and J. R. Lakowicz, *Enhanced fluorescence from fluorophores on fractal silver surfaces*, J. Phys. Chem. B **107**, 8829 (2003).
- [161] O. G. Tovmachenko, C. Graf, D. J. van den Heuvel, A. van Blaaderen, and H. C. Gerrisen, *Fluorescence enhancement by metal-core/silica-shell nanoparticles*, Adv. Mater. **18**, 91 (2006).

- [162] A. Taflove and S. C. Hagness, *Computational electrodynamics: the finite-difference time-domain method*, Artech House, Norwood MA, 2000.
- [163] C. Oubre and P. Nordlander, *Optical properties of metallodielectric nanostructures calculated using the finite difference time domain method*, J. Phys. Chem. B **108**, 17740 (2004).
- [164] F. J. Garcia de Abajo and A. Howie, *Retarded field calculation of electron energy loss in inhomogeneous dielectrics*, Phys. Rev. B **65**, 115418 (2002).
- [165] S. J. Oldenburg, S. L. Westcott, R. D. Averitt, and N. J. Halas, *Surface enhanced Raman scattering in the near infrared using metal nanoshell substrates*, J. Chem. Phys. **111**, 4729 (1999).
- [166] J. B. Jackson, S. L. Westcott, L. R. Hirsch, J. L. West, and N. J. Halas, *Controlling the surface enhanced Raman effect via the nanoshell geometry*, Appl. Phys. Lett. **82**, 257 (2003).
- [167] P. F. Liao and A. Wokaun, *Lightning rod effect in surface enhanced Raman scattering*, J. Chem. Phys. **76**, 751 (1982).
- [168] E. Dulkeith, A. C. Morteani, T. Niedereichholz, T. A. Klar, J. Feldmann, S. A. Levi, F. C. J. M. van Veggel, D. N. Reinhoudt, M. Möller, and D. I. Gittins, *Fluorescence quenching of dye molecules near gold nanoparticles: radiative and nonradiative effects*, Phys. Rev. Lett. **89**, 203002 (2002).
- [169] J. Enderlein, *Spectral properties of a fluorescing molecule within a spherical metallic nanocavity*, Phys. Chem. Chem. Phys. **4**, 2780 (2002).
- [170] O. Wilson, G. J. Wilson, and P. Mulvaney, *Laser writing in polarized silver nanorod films*, Adv. Mater. **14**, 1000 (2002).
- [171] N. J. Halas, *Playing with plasmons: Tuning the optical resonant properties of metallic nanoshells*, MRS Bull. **30**, 362 (2005).
- [172] N. J. Halas, *The optical properties of nanoshells*, Optics & Photonics News **13**, 26 (2002).
- [173] K. Kneipp, Y. Wang, H. Kneipp, L. T. Perelman, I. Itzkan, R. R. Dasari, and M. S. Feld, *Single molecule detection using surface enhanced Raman scattering (SERS)*, Phys. Rev. Lett. **78**, 1667 (1997).
- [174] A. J. Haes, L. Chang, W. L. Klein, and R. P. van Duyne, *Detection of a biomarker for Alzheimer's disease from synthetic and clinical samples using a nanoscale optical biosensor*, J. Am. Chem. Soc. **127**, 2264 (2005).
- [175] H. C. van de Hulst, *Light scattering by small particles*, Dover Publications, New York, 1957.
- [176] J. A. Stratton, *Electromagnetic theory*, McGraw-Hill Companies, 1941.
- [177] S. Asano and G. Yamamoto, *Light scattering by a spheroidal particle*, Appl. Opt. **14**, 29 (1975).
- [178] S. Asano, *Light scattering properties of spheroidal particles*, Appl. Opt. **18**, 712 (1979).
- [179] B. R. Johnson, *Calculation of light scattering from a spherical particle on a surface by the multipole expansion method*, J. Opt. Soc. Am. A **13**, 326 (1996).
- [180] M. I. Mishchenko and L. D. Travis, *Capabilities and limitations of a current Fortran implementation of the T-matrix method for randomly oriented, rotationally symmetric scatterers*, J. Quant. Spectrosc. Radiat. Transfer **60**, 309 (1998).
- [181] M. I. Mishchenko, L. D. Travis, and D. W. Mackowski, *T-matrix computations of light scattering by nonspherical particles: a review*, J. Quant. Spectrosc. Radiat. Transfer **55**, 535 (1996).

Summary

Coherent oscillations of free electrons in a metal, localized in a small volume or at an interface between a metal and a dielectric medium, have attracted a lot of attention in the past decades. These so-called surface plasmons have special optical properties that can be used in many applications ranging from optoelectronics to sensing of small quantities of molecules. One of the key issues is that electromagnetic energy can be confined to a relatively small volume close to the metal surface. This field enhancement and the resonance frequency strongly depend on the shape and size of the metal structures. In this thesis, several fabrication methods to create these metal structures on the nanometer to micrometer scale are presented. The optical properties are studied with a special emphasis on the effect of shape anisotropy.

In Chapters 2 and 3, we use self-assembled 2D colloidal crystals as mask to fabricate arrays of metal triangles on a substrate. One of the limitations of this nanosphere lithography technique is that the size of the holes in the colloidal mask (through which the metal is evaporated) is determined by the size of the colloids in the mask. We have alleviated this restriction by use of MeV ion irradiation and wet-chemical growth of silica on top of the colloidal mask.

In Chapter 2, we show that irradiation with highly energetic ions causes an in-plane expansion of the silica spheres in the mask, thereby reducing the size of the holes in the mask. The size of the holes is controlled very accurately by the ion beam fluence. This Chapter also shows that colloidal masks with arbitrary symmetry and spacing can be obtained by use of optical tweezers. Evaporation at different angles with respect to the substrate surface gives additional control over structure and inter-particle spacing. It also allows particles of different metals to be deposited next to each other. Large arrays of metal particles with dimensions in the 15–30 nm range are demonstrated.

Chapter 3 presents an alternative method to modify colloidal masks for nanolithography. Using a wet-chemical method, a thin layer of silica is grown onto the substrate and the colloidal mask. A dispersion of small seed colloids is added to the reaction mixture to provide a large surface area. It is shown that the thickness of the silica coating on the mask is less than the increase of the size of the seed colloids. This indicates that the growth mechanism on the mask is more diffusion-limited than reaction-limited. The size of the holes can be controlled accurately by using a calibration curve. Metal particles with sizes down to tens of nanometers were fabricated with this method.

Chapter 4 concentrates on the effects of MeV ion beam irradiation on small particles of silver and gold embedded in a silica matrix. Amorphous materials like silica are known to show anisotropic plastic deformation at constant volume when subject to MeV ion irradiation, in contrast to pure metals. We demonstrate that gold cores embedded in a silica matrix show an elongation along the direction of the ion beam, whereas silver cores rather disintegrate. The description of these metallo-dielectric systems within the framework of a visco-elastic continuum model must thus include ion-induced particle disintegration as

well as effects of temperature-dependent solubility.

Chapter 5 shows that in a slightly different system, with silver particles in an ion-exchanged soda-lime glass, ion irradiation causes an alignment of the silver nanocrystals in arrays along the ion beam direction. The optical extinction spectrum is shown to be polarization-dependent, with red- and blue-shifts of the plasmon resonance peaks for polarizations longitudinal and transverse to the arrays, respectively. We demonstrate that the band splitting can be tuned by the ion fluence. The splitting is attributed to near-field electromagnetic plasmon coupling within the arrays.

This near-field coupling is studied in more detail in Chapter 6 by means of full-field finite difference time domain simulations. Idealized linear arrays with closely spaced silver particles with a diameter of 10 nm are considered for different inter-particle spacing and array length. The results indicate that the combination of particle center-to-center spacing and diameter, rather than inter-particle spacing alone, is the key parameter determining the coupling strength. Based on these results, the experimentally observed red-shift presented in Chapter 5 is attributed to collective plasmon coupling in touching and/or in long arrays of strongly coupled particles. The simulations also indicate that the resonant electric field is concentrated in the very small gaps between the particles in the array, with a 5000 fold field intensity enhancement observed for a 1-nm spacing between the particles.

The last Chapters of this thesis focus on spherical and oblate ellipsoidal metal shell particles with dimensions comparable to the wavelength of light. The fabrication of these colloids is described in Chapter 7, and the optical properties are considered in Chapters 8 and 9.

The synthesis of metal shell colloids is done by electroless plating of silver or gold on spherical silica colloids. We show that the shape of the metal shell colloids can be changed into oblate ellipsoidal by MeV ion beam irradiation, with the anisotropy determined by the ion fluence. We demonstrate that this is due to the ion-induced anisotropic deformation of the silica core. The metal shell imposes a mechanical constraint on the deformation of the silica core, resulting in a reduced net deformation rate. With this technique, it is possible to fabricate large substrates with relatively monodisperse oblate ellipsoidal particles, with the short axis aligned in the direction of the ion beam. This enables angle-dependent optical extinction measurements on large numbers of aligned particles, providing information on the shape- and orientation-dependent optical properties of the particles.

The optical properties of these metal-shell colloids are studied in Chapter 8, both by experiments and theoretical calculations. The extinction spectra show several peaks that can be attributed to the contributions of dipole, quadrupole and higher order modes. We demonstrate that, for spherical particles, the frequencies and the relative strengths of these peaks are a complex function of the core radius and the shell thickness. This is due to a competition between phase retardation effects (causing a red-shift for larger particles) and the coupling between the surface plasmons at the inner and outer surfaces of the shell (resulting in a red-shift for thinner shells). Optical extinction measurements are done as a function of the incident angle for oblate ellipsoidal metal shell particles with size aspect ratios up to 1.8. The extinction peak in the infrared part of the spectrum is strongest for light incident along the short axis of the particles and shifts towards the red as the aspect ratio is increased. We observe a good agreement between calculations for single particles and ensemble-averaged experimental data.

Finite-difference time domain simulations and calculations by the T-matrix method, presented in Chapter 9, indicate that large Au-shell particles can sustain cavity modes, for

which the electric field is enhanced in almost the full volume of the dielectric core. We show that the resonance frequency is sensitive to the size, shape and dielectric constant of the core. The resonance frequency is found to shift towards the red for transverse polarization and blue for longitudinal polarization. This confirms the concept of a cavity mode, as this behavior is also theoretically predicted for ellipsoidal voids in a metal surrounding, in the quasistatic approximation.

Finally, the last Chapter reports on several applications of the metal structures studied in this thesis. In opto-electronics, the size of optical devices has always been limited by diffraction. By converting the optical mode into non-radiating surface plasmons, electromagnetic energy can be concentrated and guided in metal structures, with lateral mode dimensions of less than 10% of the free-space wavelength. Small variations in dielectric constant in the surrounding medium can be detected by use of optical spectroscopy on metal particle arrays. The enhanced local fields and the tunability of the plasmon resonance give rise to enhanced signals in fluorescence and surface enhanced Raman spectroscopy, and also enable biomedical applications such as drug delivery and cancer diagnosis and therapy, all of which can be optimized using the shape control explored in this thesis.

Samenvatting

Veel wetenschappers in het heden en verleden hebben zich laten inspireren door de speciale optische eigenschappen van kleine metaalstructuren. Een bekend voorbeeld hiervan zijn de rode en gele kleuren in glas-in-lood ramen, veroorzaakt door kleine goud en zilver deeltjes die zeer efficiënt licht van een bepaalde kleur absorberen. De vrije electronen in het metaal kunnen door het licht in een oscillerende beweging worden gebracht. Het kleine metaal volume beperkt de beweging van de electronen en zorgt ervoor dat ladingen zich ophopen aan het grensvlak van het metaal en het diëlectricum (bijvoorbeeld glas of lucht). Deze zogeheten oppervlakteplasmonen vinden toepassingen in diverse gebieden van wetenschap en techniek. Te denken valt aan de detectie van kleine hoeveelheden moleculen en aan componenten in de opto-electronica.

Een van de belangrijke eigenschappen van oppervlakteplasmonen is dat de electromagnetische energie kan worden geconcentreerd in een relatief klein volume dicht bij het metaal oppervlak. Deze veldversterking, net als de frequentie van de resonantie, hangt sterk af van de vorm en de grootte van de metaalstructuren. Dit proefschrift behandelt diverse fabricage methodes om metaalstructuren te maken op een schaal van enkele nanometers tot een micrometer. Daarnaast worden de optische eigenschappen van zulke metaalstructuren bestudeerd met de nadruk op de effecten als gevolg van een verandering in vorm.

Het eerste gedeelte van het proefschrift, Hoofdstuk 2 en 3, laat zien dat tweedimensionale colloïdale kristallen van silica (glas) bollen gebruikt kunnen worden als masker voor nanolithografie. Na het opdampen van een metaal en het verwijderen van het masker, blijft een hexagonaal patroon van metaal driehoekjes op een oppervlak over. Eén van de beperkingen van deze methode is dat de grootte van de gaatjes in het masker bepaald wordt door de grootte van de silica bollen. In dit proefschrift wordt aangetoond dat dit verholpen kan worden door de maskers te deformeren door middel van MeV ionenbestraling en/of door nat-chemische aangroei van silica op het masker.

In Hoofdstuk 2 laten we zien dat bestraling met hoog-energetische ionen tot gevolg heeft dat de silica colloïden uitzetten in de richting loodrecht op de ionenbundel, zodat de gaatjes in het masker kleiner worden. De grootte van de gaatjes kan nauwkeurig worden ingesteld door de ionendosis te variëren. Daarnaast kunnen maskers met elke andere gewenste ordening gemaakt worden door de bollen met een optisch pincet op het substraat te positioneren. Ook het opdampen van metalen onder diverse hoeken geeft extra controle over de uiteindelijke structuur. Zo kunnen bijvoorbeeld meerdere deeltjes van verschillende materialen naast elkaar worden opgedampt. De kleinste metaaldeeltjes hebben een grootte van 15–30 nm.

Een andere methode om de gaatjesgrootte te controleren wordt beschreven in Hoofdstuk 3. Een dunne laag silica kan via een nat-chemisch proces worden aangegroeid op het colloïdale masker en op het substraat oppervlak. Een geconcentreerde dispersie van kleine colloïden wordt toegevoegd om een groot oppervlakte te verschaffen. Het experiment laat

zien dat de aangroei op de kleine zaadcolloïden groter is dan de aangroei op het masker. Hieruit concluderen we dat het groei mechanisme op het masker meer diffusie-gelimiteerd dan reactie-gelimiteerd is. De grootte van de gaatjes in het masker kan nauwkeurig worden gecontroleerd door een goed gekarakteriseerde dispersie van zaadcolloïden te gebruiken. Met deze methode zijn metaaldeeltjes gefabriceerd met afmetingen tot enkele tientallen nanometers.

Hoofdstuk 4 concentreert zich op het effect van MeV ionenbestraling op kleine metaaldeeltjes in glas. Het is bekend dat amorfe materialen (zoals glas) een plastische vormverandering ondergaan tijdens de bestraling met hoog energetische ionen, waarbij het volume constant blijft. Kristallijne materialen zoals goud of zilver vervormen niet, behalve wanneer ze zijn ingebed in bijvoorbeeld silica. We laten zien dat ronde goud deeltjes vervormen tot staafjes met de lange as in de richting van de ionenbundel en dat zilver deeltjes uiteen vallen. Een model dat de vervorming van deze metallo-diëlectrische materialen beschrijft zal daarom ook de effecten van de temperatuur-afhankelijke oplosbaarheid mee moeten nemen.

In Hoofdstuk 5 wordt een iets ander systeem besproken, bestaande uit silica glas gedoteerd met zilver ionen waarvan een deel geclusterd is in deeltjes. De ionenbestraling veroorzaakt een uitlijning van (ronde) zilver nanokristallen langs de richting van de ionenbundel. Na de bestraling is het glas van kleur veranderd, en hangt het transmissie spectrum af van de richting van de polarisatie en van de hoek van inval van het licht. De plasmonresonantie is rood (blauw) verschoven voor de polarisatie langs (loodrecht op) de keten van deeltjes. De opsplitsing van de plasmonresonantie kan aangepast worden door de ionendosis te variëren en wordt toegeschreven aan electromagnetische koppeling van de deeltjes in de ketens.

Dit koppelingsmechanisme wordt verder onderzocht in Hoofdstuk 6, waarbij we gebruik maken van simulaties van het electromagnetische veld met behulp van de finite-difference time domain (FDTD) techniek. Geïdealiseerde kettingen van zilver deeltjes met een diameter van 10 nm zijn doorgerekend voor verschillende afstanden tussen de deeltjes en verschillende ketenlengtes. De simulaties laten zien dat de koppelingssterkte wordt bepaald door de combinatie van diameter en afstand tussen de deeltjes. De experimenteel waargenomen roodverschuiving (Hoofdstuk 5) kan verklaard worden door aan te nemen dat de ketens erg lang zijn en/of dat de deeltjes in de ketens elkaar raken. Op de resonantie concentreert het elektrische veld zich tussen de deeltjes, waarbij de intensiteit met een factor 5000 versterkt kan zijn als de deeltjes op 1 nm van elkaar liggen.

In het laatste gedeelte van het proefschrift worden deeltjes met een metalen schil onderzocht, met afmetingen die vergelijkbaar zijn met de golflengte van het licht. De fabricage van de ronde en oblaat-ellipsoïdale deeltjes wordt beschreven in Hoofdstuk 7; de optische eigenschappen worden behandeld in Hoofdstuk 8 en 9.

Metaal-schil deeltjes worden gevormd via een synthese waarbij zilver of goud ionen in oplossing worden gereduceerd op de silica deeltjes. Voor de bestraling met hoog energetische ionen worden de deeltjes op een oppervlak gedroogd. Het blijkt dat de ionenbestraling ook metaal-schil deeltjes van vorm doet veranderen, doordat de silica kern van de deeltjes vervormt. Deze vervorming wordt tegengewerkt door de metalen schil, wat tot gevolg heeft dat metaal-schil deeltjes een lagere deformatiesnelheid hebben dan silica kernen zonder een metalen schil. Deze techniek maakt het mogelijk om grote oppervlakken te maken die bedekt zijn met relatief monodisperse oblaat-ellipsoïdale deeltjes, met de korte as uitgelijnd in de richting van de ionenbundel. Hierdoor kunnen hoek- en

oriëntatie-afhankelijke eigenschappen van de deeltjes gemeten worden aan grote aantallen deeltjes tegelijk.

De optische eigenschappen van deze metaal-schil deeltjes worden nader bestudeerd in Hoofdstuk 8. De pieken in de extinctiespectra komen overeen met de bijdragen van de dipool, quadrupool en hogere orde modes. Voor ronde deeltjes laten we zien dat de frequenties en sterktes van deze modes op een complexe manier afhangen van de grootte van de kern en de dikte van de schil. Dit komt door een competitie tussen de effecten van de fase-vertraging (met een roodverschuiving voor grotere deeltjes tot gevolg) en de koppeling tussen de oppervlakteplasmonen op de grensvlakken kern/schil en schil/omgeving (roodverschuiving voor dunnere schillen). Optische extinctiemetingen aan oblaat-ellipsoïdale metaal-schillen als functie van de hoek en aspect ratio laten zien dat de piek in het infrarood het sterkst is voor licht dat invalt langs de korte as van het deeltje en roodverschuift wanneer de aspect ratio groter wordt. De experimentele data komen goed overeen met de berekeningen aan enkele deeltjes.

In Hoofdstuk 9 geven FDTD simulaties en T-matrix berekeningen aan dat goud schil deeltjes met een diameter groter dan een halve micrometer een resonantie hebben waarvoor het elektrische veld versterkt is over bijna het gehele volume van de diëlectrische kern. De resonantiefrequentie wordt bepaald door de grootte, vorm en materiaalconstanten van de kern. Voor oblaat-ellipsoïdale deeltjes verschuift de resonantiefrequentie van deze mode naar het blauw voor polarisatie langs de lange as van het deeltje. Dit bevestigt het concept van een mode in de holte, omdat ditzelfde gedrag theoretisch voorspeld wordt voor ellipsoïdale holtes in een metaal die veel kleiner zijn dan de golflengte van het licht.

Tenslotte worden in Hoofdstuk 10 van dit proefschrift diverse toepassingen van metaal-structuren behandeld. De grootte van optische componenten in opto-electronica is altijd beperkt geweest door diffractie. Door de optische mode om te zetten in niet-stralende oppervlakteplasmonen, kan electromagnetische energie geconcentreerd, getransporteerd en gemanipuleerd worden op een schaal die kleiner is dan de golflengte van het licht. Kleine variaties in de diëlectrische constante van het omliggende medium kunnen worden waargenomen met behulp van optische spectroscopie. De lokaal versterkte velden en de controle over de plasmonfrequentie zorgen voor een versterking van het te meten signaal in fluorescentie en Raman spectroscopie metingen. Ook biomedische toepassingen zoals het lokaal toedienen van medicijnen en een vorm van diagnose en behandeling van kanker worden hiermee mogelijk. Met behulp van de controle over de vorm van de deeltjes, zoals bestudeerd in dit proefschrift, kunnen deze processen worden geoptimaliseerd.

List of publications

This thesis is based on the following publications:

- *Combined optical tweezers/ion beam technique to tune colloidal masks for nanolithography*, D. L. J. Vossen, D. Fific, J. J. Penninkhof, T. van Dillen, A. Polman, and A. van Blaaderen, *Nano Lett.* **5**, 1175-1179 (2005). (Chapter 2)
- *Chemical modification of colloidal masks for nanolithography*, D. L. J. Vossen, J. J. Penninkhof, and A. van Blaaderen, to be submitted. (Chapter 3)
- *Anisotropic deformation of metallo-dielectric core-shell colloids under MeV ion irradiation*, J. J. Penninkhof, T. van Dillen, S. Roorda, C. Graf, A. van Blaaderen, A. M. Vredenberg, and A. Polman, *Nucl. Instr. and Meth. in Phys. Res. B* **242**, 523-529 (2006). (Chapter 4)
- *Mega-electron-volt ion beam induced anisotropic plasmon resonance of silver nano-crystals in glass*, J. J. Penninkhof, A. Polman, L. A. Sweatlock, S. A. Maier, H. A. Atwater, A. M. Vredenberg, and B. J. Kooi, *Appl. Phys. Lett.* **83**, 4137-4139 (2003). (Chapter 5)
- *Very large plasmon band shift in strongly coupled metal nanoparticle chain arrays*, L. A. Sweatlock, J. J. Penninkhof, S. A. Maier, A. Polman, and H. A. Atwater, *Mat. Res. Soc. Symp. Proc.* **797**, W4.6.1 (2004). (Chapter 6)
- *Highly confined electromagnetic fields in arrays of strongly coupled Ag nanoparticles*, L. A. Sweatlock, S. A. Maier, H. A. Atwater, J. J. Penninkhof, and A. Polman, *Phys. Rev. B* **71**, 235408 (2005). (Chapter 6)
- *Angle-dependent extinction of anisotropic silica/Au core/shell colloids made via ion irradiation*, J. J. Penninkhof, C. Graf, T. van Dillen, A. M. Vredenberg, A. van Blaaderen, and A. Polman, *Adv. Mater.* **17**, 1484-1488 (2005). (Chapter 7)
- *Angle-dependent extinction of anisotropic Au shell colloids: experiment and theory*, J. J. Penninkhof, A. Moroz, C. Graf, A. Polman, and A. van Blaaderen, to be submitted. (Chapter 8)
- *Optical cavity modes in Au-shell particles*, J. J. Penninkhof, A. Moroz, L. A. Sweatlock, H. A. Atwater, A. van Blaaderen, and A. Polman, to be submitted. (Chapter 9)

Other publications, related to this thesis:

- *Ion beam-induced anisotropic plastic deformation of silicon microstructures*, T. van Dillen, M. J. A. de Dood, J. J. Penninkhof, A. Polman, S. Roorda, A. M. Vredenberg, *Appl. Phys. Lett.* **84**, 3591-3593 (2004).
- *Energy transport in metal nanoparticle plasmon waveguides*, S. A. Maier, P. G. Kik, L. A. Sweatlock, H. A. Atwater, J. J. Penninkhof, A. Polman, S. Meltzer, E. Harel, A. A. G. Requicha, B. E. Koel, *Mat. Res. Soc. Symp. Proc.* **777**, P.T7.1.1-T7.1.12 (2003).
- *Erbium-thulium interaction in broadband infrared luminescent silicon-rich silicon oxide*, S. Y. Seo, J. H. Shin, B. S. Bae, N. Park, J. J. Penninkhof, A. Polman, *Appl. Phys. Lett.* **82**, 2445-3447 (2003).

Dankwoord

Terugkijkend op vier jaar als promovendus wil ik een aantal mensen bedanken.

Allereerst mijn beide promotoren: Albert Polman en Alfons van Blaaderen. Jullie enthousiasme voor wetenschappelijk onderzoek werkt aanstekelijk! Alfons, even bij jou enkele resultaten doorspreken resulteerde altijd in weer een hele nieuwe waslijst aan ideeën en projecten. Bedankt dat ik bij jou in de groep mocht werken en gebruik mocht maken van de labfaciliteiten en electronenmicroscopen in Utrecht. Albert, ook jou komt dank toe. Hoewel je soms naar mijn idee iets *te* enthousiast was (wellicht wilde je proberen mijn kritische blik te compenseren), heb je me veel vrijheid gegeven om mijn projecten vorm te geven. Bedankt ook voor de vele mogelijkheden om internationaal te gaan. Ik heb veel van je geleerd hoe je een goede presentatie moet geven. Albert en Alfons, ik ben blij dat ik met jullie mocht samenwerken en kon profiteren van jullie expertise, creativiteit en professionaliteit.

I also would like to thank Harry Atwater and Luke Sweatlock. The joint AMOLF-Caltech Summerschool in August 2002 was the start of a fruitful collaboration, with regular visits to Europe and Caltech. I have enjoyed my stays at Caltech in April 2003 and in May 2005 very much. Thanks for the numerous discussions about the FDTD simulations and plasmonics in general.

De gezamenlijke koffiepauzes in de kantine en de goede sfeer op de “thuisbasis” AMOLF zal ik niet snel vergeten. Ik wil mijn kamergenoten Anna Tchebotareva, Sjoerd Roorda, Janne Savolainen en Sébastien Bidault bedanken voor de gezelligheid en de discussies over experimenten en de Nederlandse taal. René, je voortvarendheid en zelfstandigheid tijdens jouw afstudeerproject maakten dat de samenwerking heel soepel verliep. Teun, bedankt voor het leren van de fijne kneepjes van de ionenbestralingen en de electronenmicroscop. Ook de overige groepsleden wil ik bedanken voor hun bijdrages aan de sfeer binnen de groep, de dagelijkse discussie en de wekelijkse werkbesprekingen: Michiel de Dood, Jeroen Kalkman, Jan van der Elsen, Hans Mertens, Ewold Verhagen, Martin Kuttge, Rob van Loon, Femius Koenderink, Adriaan Tip, Max Siem, Timon van Wijngaarden, Martien den Hartog en Ernst Jan Vesseur. Ook Kobus Kuipers wil ik bedanken voor zijn kritische opmerkingen en vragen tijdens de werkbesprekingen. Hoewel ik de overige leden van de afdeling Nanophotonics niet afzonderlijk bij naam noem, wil ik ook hen bedanken voor de goede contacten en interessante colloquia op de donderdagochtend.

Een kleiner deel van mijn tijd heb ik in Utrecht doorgebracht, hoewel niet altijd even zichtbaar voor mijn directe collega's in het Ornstein Laboratorium. Regelmatig was ik te vinden in het Robert van der Graaff laboratorium om mijn samples te bestralen met MeV ionen. Voor alle interesse en hulp bij de bestralingen wil ik Arjen Vredenberg bedanken. Ik bewaar ook goede herinneringen aan ons samenspel op cello en viool ter voorbereiding van de uitvoeringen van het Princeton Muziekfestival. Ook de andere gebruikers van bundellijn 2 wil ik bedanken voor de plezierige samenwerking: Eddy van Hattum, Jeroen

Westerhout, Elmuez Dawi, Wim Arnold Bik.

Experimenten kunnen niet zonder technische ondersteuning. Zowel op AMOLF als in Utrecht heb ik hierbij veel hulp gekregen. Hiervoor wil ik Johan Derks, Chris Rétif en Hans Zeijlemaker in het bijzonder bedanken. Hun inzet om het grote arsenaal aan opstellingen in de groep in goede conditie te houden, heeft zeker vruchten afgeworpen. Ook de versnellertechnici in Utrecht wil ik hartelijk bedanken voor hun hulp bij en kennis van de 6 MV versneller. Ik hoop dat de nieuwe versneller jullie veel plezier mag geven. Dank ben ik verschuldigd aan Bart Kooi (Universiteit Groningen), Hans Meeldijk (Universiteit Utrecht) en Frans Tichelaar (Universiteit Delft) voor (hulp bij) de metingen op de transmissie electronen microscoop. Daarnaast wil ik de mensen van de werkplaats en de tekenkamer op AMOLF noemen, die altijd voor me klaar stonden om me te helpen en vaak al op korte termijn tijd konden vrijmaken om mijn wensen ten uitvoer te brengen.

Veel van het werk in dit proefschrift is tot stand gekomen mede dankzij Christina Graf, Dirk Vossen, Carlos van Kats, Alexander Moroz en Job Thijssen. Christina, jij leerde me de details van de syntheses van core-shell colloïden. Je was een beetje verbaasd dat meteen de eerste synthese van de goud-schil deeltjes al goed ging... Bedankt voor alle andere metaal-schil-deeltjes die je me vanuit Duitsland stuurde. Ik weet hoeveel werk het is om ze te maken! Ook Carlos, de andere expert op het gebied van colloïdsynthese, bedankt voor het delen van je kennis. Dirk, ons gezamenlijke werk aan de colloïdale maskers heeft twee mooie artikelen opgeleverd. Dank je wel voor je goede humeur en plezierige samenwerking. Alexander, thanks for all the time you spent after working hours and during the weekends to work on the computer programs. Many of the results in Chapters 8 and 9 would not have been possible without you. Job, bedankt voor de vele discussies en je niet afnemende interesse voor problemen die met (licht-)verstrooiing te maken hebben. Ik heb hier veel van geleerd en ben vereerd dat je mijn paranimf wilt zijn.

Omdat ik relatief weinig in Utrecht op kantoor ben geweest, hebben mijn Utrechtse kamergenoten Yu Ling Wu, Astrid van der Horst, en later (toen ik naar de andere kant verhuisde) Patrick Johnson, Paddy Royall, Andrew Campbell, Esther Vermolen en Peter van Oostrum regelmatig tegen een leeg bureau aan moeten kijken: sorry! Dank ben ik ook verschuldigd aan alle overige leden van de Soft Condensed Matter groep: Arnout Imhof, Marjolein Dijkstra, Christina Christova, Alejandro Cuetos, María Delgado Flores, Ahmet Demirôrs, Didi Derks, Damir Fific, Andrea Fortini, Dannis 't Hart, Antti-Pekka Hynninen, Michiel Hermes, Mirjam Leunissen, Matthieu Marechal, Catherine Quilliet, Eduardo Sanz, Svytoslav Savenko, Matthias Schmidt, Johan Stiefelhagen, Teun Vissers, Carmen Zoldesi en alle andere studenten die kwamen en weer gingen. De jaarlijkse sin-terklaasavonden waren hilarisch en altijd zeer gezellig.

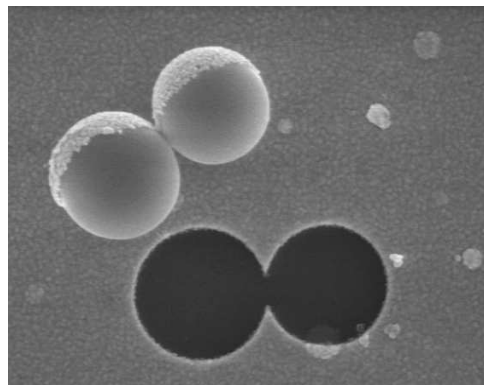
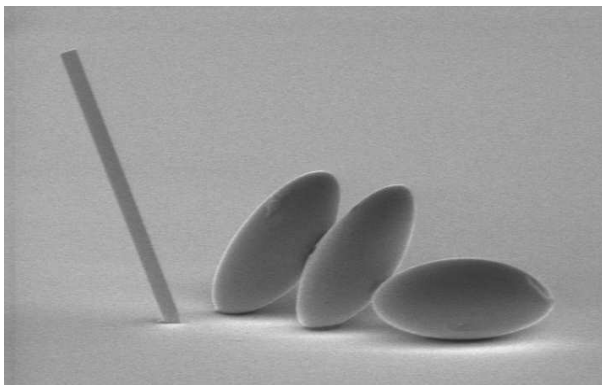
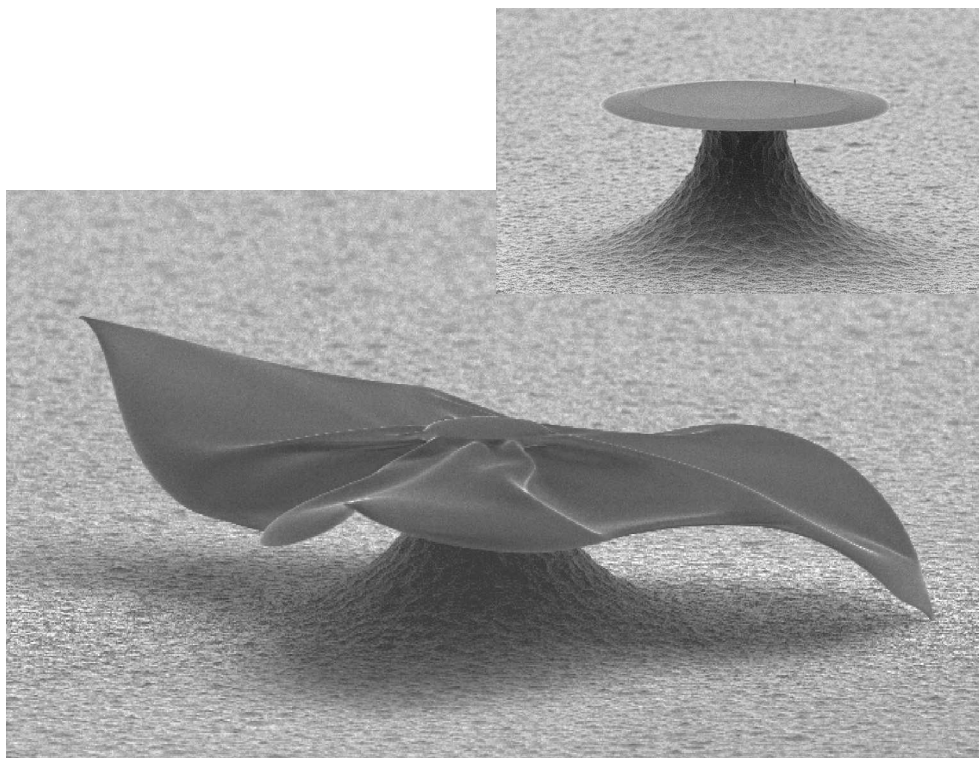
Als laatste wil ik mijn familie, kennissen en vrienden bedanken voor de belangstelling en de steun die ze getoond hebben in de afgelopen jaren. Carlijn, je had altijd een luis-terend oor tijdens onze sportieve activiteiten. Fijn dat je mijn paranimf wilt zijn! En mijn lieve Sander, de allerlaatste woorden van dit dankwoord zijn voor jou: dank je wel voor het geduld, de liefde en de steun die je me geeft. *Je t'aime*. Op de toekomst!

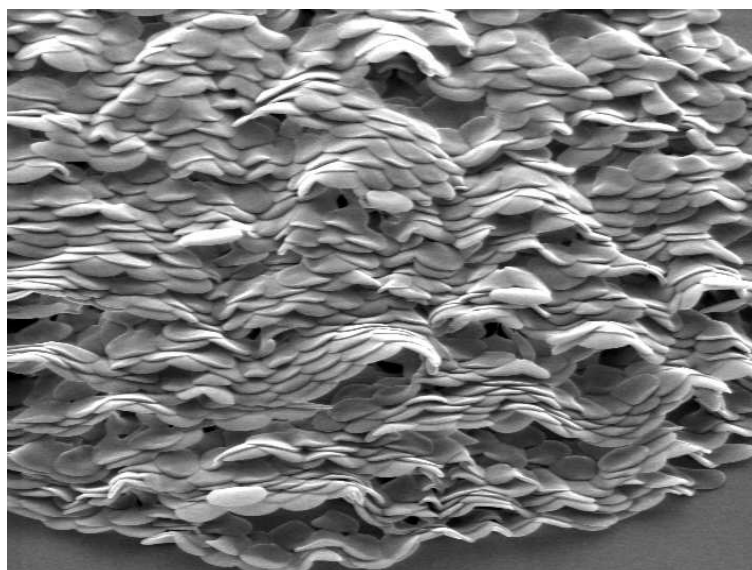
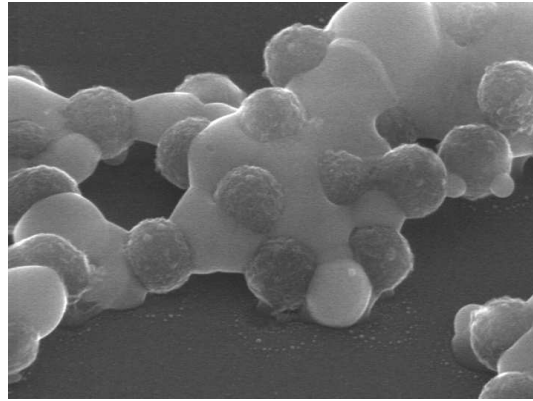
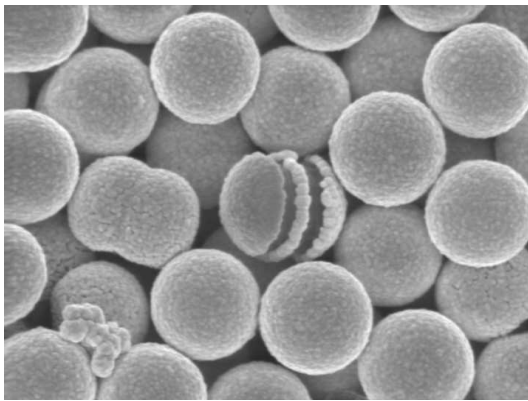
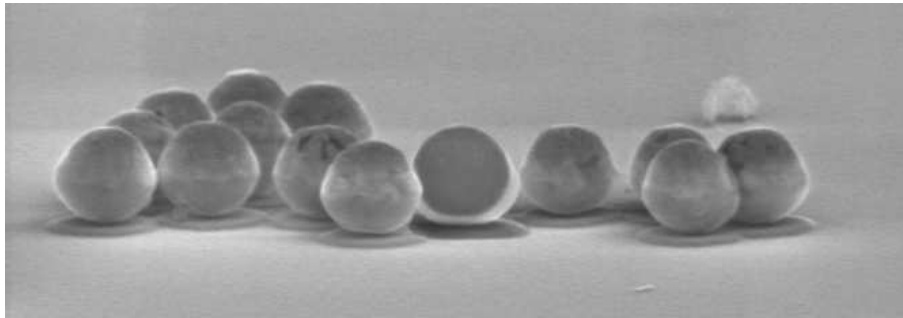
Curriculum vitae

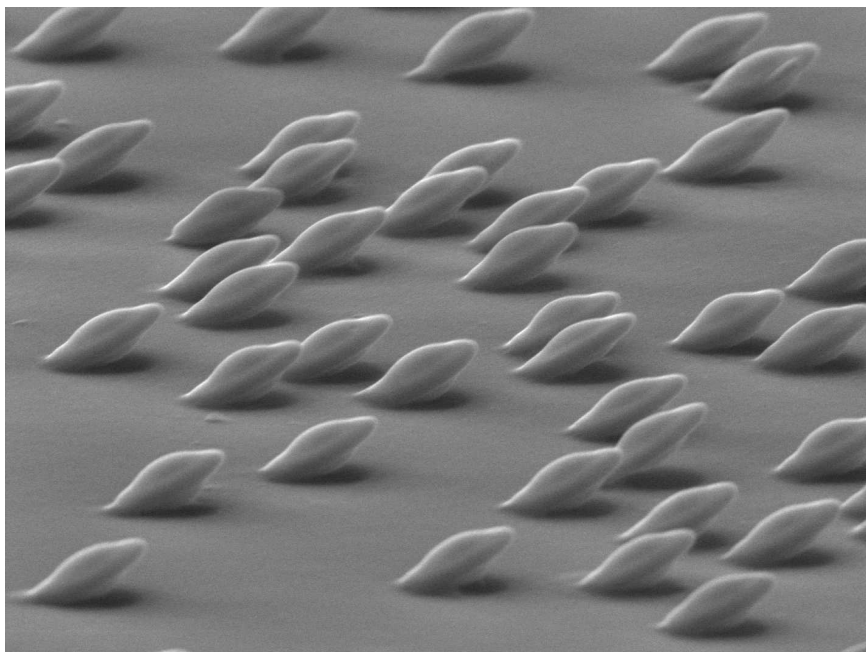
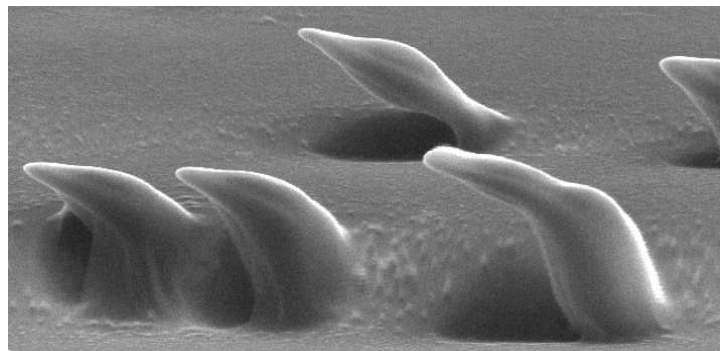
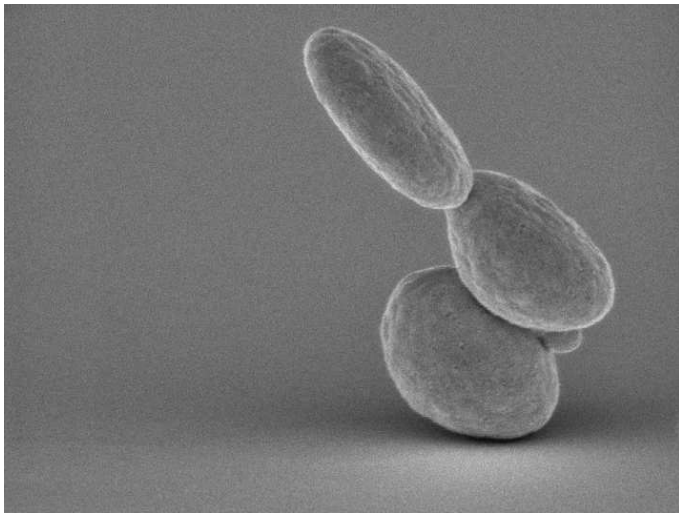
Joan Penninkhof werd geboren op 23 maart 1978 te Utrecht. In 1996 behaalde zij haar VWO diploma aan het Oosterlicht College te Nieuwegein. In september van datzelfde jaar begon zij aan de studies wiskunde en natuurkunde aan de Universiteit Utrecht. Na twee jaar werd de overstap gemaakt naar de experimentele natuurkunde, waarin zij in 2002 afstudeerde met het predicaat met genoegen. Haar afstudeeronderzoek naar optische versterkers deed zij aan het FOM-instituut voor Atoom- en Molecuulfysica (AMOLF) onder begeleiding van Prof. Dr. A. Polman. Tijdens haar studie was Joan onder andere actief binnen de β -bedrijvendagen Utrecht, het StudentenOverleg Natuur- en Sterrenkunde en het Utrechtsch Studenten Concert.

Na de AMOLF-CALTECH Nanophotonics Summerschool in augustus 2002 is Joan als onderzoeker in opleiding gaan werken in de groepen van Prof. Dr. A. Polman (Photonic Materials, AMOLF) en Prof. Dr. A. van Blaaderen (Soft Condensed Matter, Universiteit Utrecht), in dienst van de Stichting FOM. Daarbij werd nauw samengewerkt met de onderzoeksgroep van Prof. Dr. H. A. Atwater van het California Institute of Technology te Pasadena, CA, USA. De resultaten van dit promotieonderzoek staan beschreven in dit proefschrift.

Image gallery







Color images

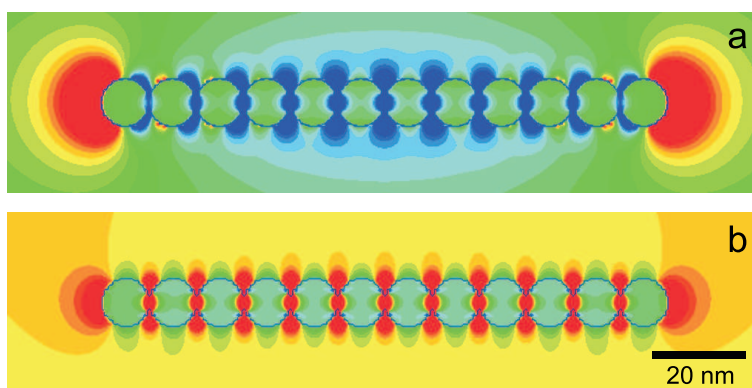


Figure 6.6: Distribution of the longitudinal component of the electric field (E_x) in the vicinity of an array of twelve Ag particles (10 nm diameter), illustrating two distinct modes. (a) an antenna-like mode resembling that of a single elongated wire is excited resonantly at 0.35 eV; (b) a coupled particle-like mode resembling that of a chain of independent particles is excited resonantly at 1.65 eV. The slight axial asymmetry of the field distribution is caused by superposition of the resonant mode with the exciting plane-wave.

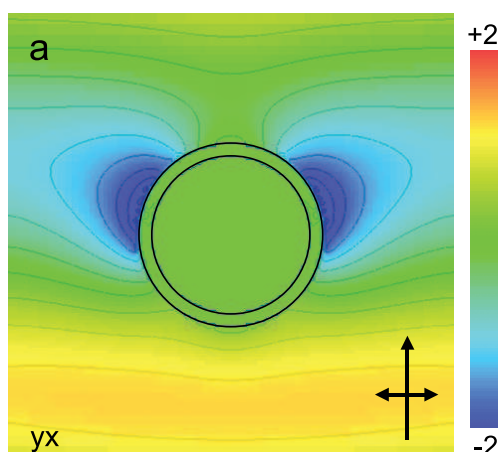


Figure 9.1(a): FDTD calculation time snapshot [at $t = 0$ in Fig. 9.1(b)] of the x-component of the electric field of a plane-wave propagating in the y-direction at a frequency of 150 THz and interacting with a spherical Au-shell in silica ($R_{core} = 228$ nm, $t_{Au} = 38$ nm). The plane-wave is polarized horizontally in the plane (double arrow), and its amplitude is normalized to 1. The color scale ranges from -2 to +2. The difference between two consecutive contour lines is 0.4.

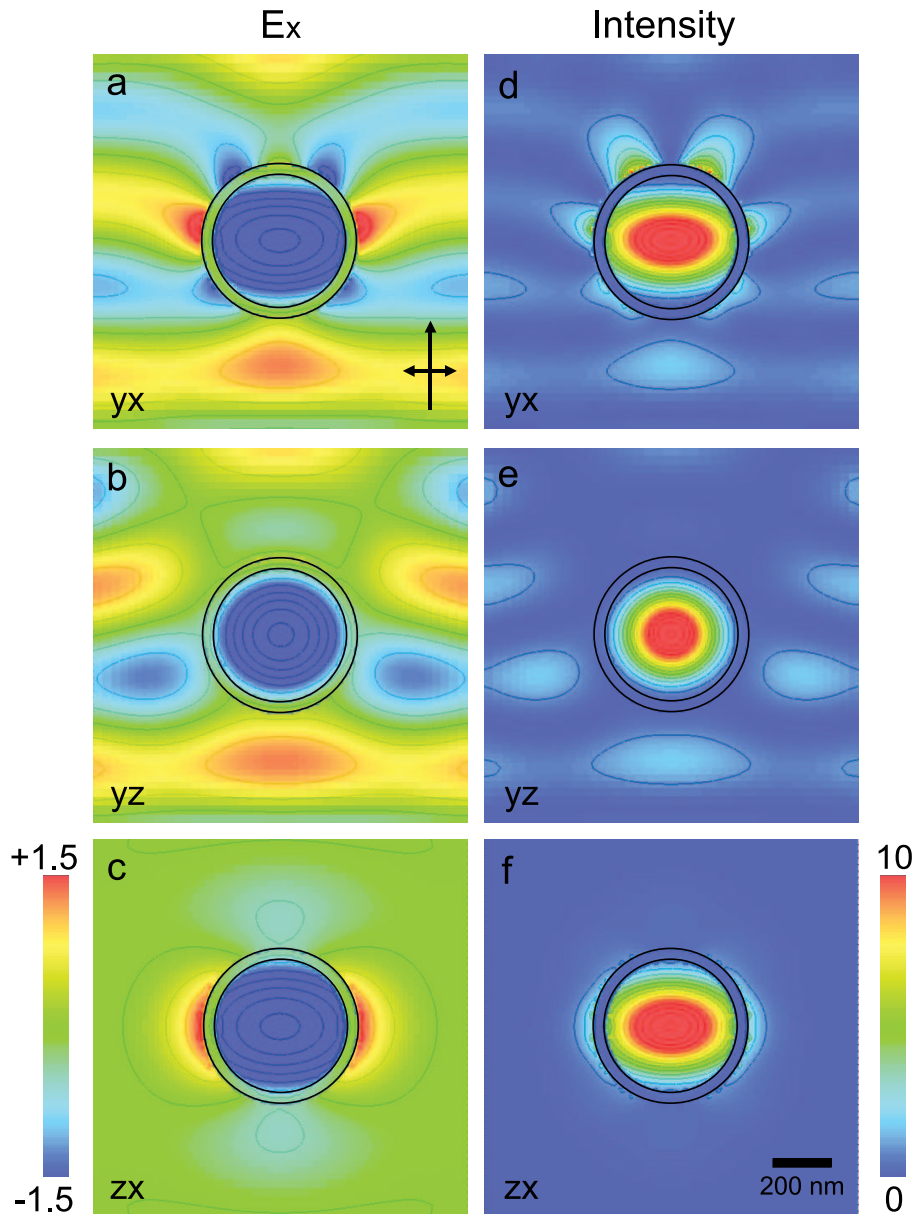
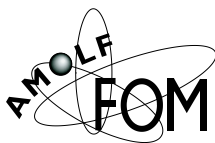


Figure 9.3: FDTD time snapshot of the x-component (left) and intensity (right) of the electric field in the yx-plane (a, d), yz-plane (b, e) and zx-plane (c, f). On-resonance plane-wave excitation at 335 THz of a Au-shell sphere in silica ($R_{core} = 228$, $t_{Au} = 38$ nm). Color scale bars range from -1.5 to 1.5 (a-c) and from 0 to 10 (d-f); the difference between consecutive contour lines amounts to a factor 0.5 (a-c) and 1 (d-f). The plane-wave propagates in the y-direction, and is polarized along x.



The work described in this thesis was performed at the FOM-Institute for Atomic and Molecular Physics, Kruislaan 407, 1098 SJ Amsterdam, The Netherlands, in collaboration with Utrecht University, Utrecht, The Netherlands, and California Institute of Technology, Pasadena, CA.

A digital version can be downloaded from <http://www.amolf.nl> and <http://www.colloid.nl>.

Affiliations:

Prof. Dr. A. Polman
Center for Nanophotonics, FOM-institute AMOLF, Amsterdam, The Netherlands

Prof. Dr. A. van Blaaderen
Soft Condensed Matter, Utrecht University, Utrecht, The Netherlands